ORGANIC SUPERCAPACITORS

DEVELOPMENT OF REDOX-ACTIVE ORGANIC ELECTRODES WITH LOW-COST CARBON BLACK FOR HIGH-PERFORMANCE SUPERCAPACITORS FOR ELECTRIC VEHICLE APPLICATIONS

By ARJUN REGO

A Thesis Submitted to the School of Graduate Studies in the Partial Fulfillment of the Requirements for the Degree Master of Applied Science

April 4, 2024

McMaster University

Master of Applied Science (2024)

Hamilton, Ontario (Department of Chemical Engineering)

TITLE: Development of Redox-Active Organic Electrodes with Low-Cost Carbon Black for High-Performance Supercapacitors for Electric Vehicle Applications

AUTHOR: Arjun Rego (McMaster University)

SUPERVISOR: Dr. Drew Higgins

PAGES: 91

Lay Abstract

Worldwide efforts to reduce greenhouse gas emissions, like CO_2, have made the world focusing on making more environmentally sustainable transportation methods, such as switching to electric vehicles (EVs). However, EVs still face performance and longevity issues due to the limitations of the batteries used. Batteries are not designed to charge and discharge quickly, however supercapacitors, which are like batteries, can charge and discharge much faster, making them a great match to incorporate into EVs alongside batteries. Traditional metal supercapacitor materials are costly and non-sustainable, but organic molecules like quinones offer a much cheaper, sustainable solution. Modifying quinones along with the addition of cheap carbon additives can vastly improve its energy storage performance and long-term usage. With future scalability in mind, this work demonstrates the potential for organic materials to potentially be used to enhance the performance of next generation EVs.

Abstract

Global efforts to reduce greenhouse gas emissions, particularly CO_2, have led countries to focus on decarbonizing the transportation sector. Moving towards electric vehicles (EVs) is necessary to reduce emissions, however despite EV technological advancements they have shortcomings in both performance and longevity. Supercapacitors are similar to batteries, however their ability to easily charge and discharge at much higher rates makes them excellent devices to work in tandem with batteries to advance their collective performance capabilities in EVs. Traditional metal-based supercapacitor materials remain to be high cost, non-renewable, and often environmentally toxic. On the other hand, quinones are organic materials considered as promising candidates for organic electrodes due to the redox activity, low cost, ease of structural modifications, nontoxicity, and

renewability. To overcome quinone challenges with low electrical conductivity and dissolution in electrolyte, polymerizing quinones has become a popular modification. Conducting polymers (CPs) are increasing in interest as their π-conjugated structures provide efficient electron transfer and good electrical conductivity. In the work of this master's thesis, two types of materials were developed for supercapacitor applications; a polyimide made from alternating units of the quinones 3,4,9,10-perylenetetracarboxylic dianhydride (PTCDA) and 2,6-diaminoanthraquinone (DAAQ) known as poly-perylene-3,4,9,10-tetracarboxydiimide-anthraquinone (PPA), and a truncated analogue of PPA comprised of PTCDA and two molecules of 2-diaminoanthraquinone (2-AAQ), termed N,N′-bis(2-anthra-quinone)]-perylene-3,4,9,10- tetracarboxydiimide (PDI-DAQ). All the original redox-active sites were retained following a facile synthesis to achieve fast multi-electron transfer mechanisms. These materials both were used to prepare composite electrodes with a low-cost carbon black (Ketjenblack) via simple and scalable preparation methods. Capacitances reached up to 377 F g^{-1} at 5 mV s^{-1} with a capacitance retention of 63.9% after 10,000 cycles at 100 mV s^{-1}. This work demonstrates the impressive energy storage capabilities of novel organic molecules in supercapacitors with low-cost carbon black to improve the performance of next-generation EVs.

Acknowledgements

This work was completed with the financial aid provided by the Department of Chemical Engineering, and the Ontario Graduate Fellowship awards I received.

I would like to thank my supervisor, Dr. Drew Higgins, for providing me the opportunity to pursue this research and for his support throughout the journey. Drew was continuously a positive influence for me to continue advancing my academic pursuits.

I would also like to thank all my lab members in the Higgins Lab for fostering an incredible work environment, especially those who contributed to my manuscripts as coauthors and provided guidance.

I extend my appreciation to my committee members, Dr. Stuart Linley, and Dr. Carlos Filipe, for their time, willingness, and expertise to evaluate my M.A.Sc. work.

My continuous appreciation throughout my academic journey goes out to my family. Specifically, my parents, Martin and Parminder Rego, and my sister, Sabrina Elanko, who have always supported and believed in me.

Contents

List of Figures

Introduction & Methodology (Chapters 1 & 2)

PDI-DAQ (Chapter 3)

PPA (Chapter 4)

List of Tables

Introduction & Methodology (Chapters 1 & 2)

PPA (Chapter 4)

Abbreviations and Symbols

Abbreviations

AC	Activated Carbon
BET	Brunauer-Emmett-Teller
CB	Carbon Black
CNT	Carbon Nanotube
CP	Conducting Polymer
CV	Cyclic Voltammetry
DAAQ	2,6-diaminoanthraquinone
EDLC	Electric Double Layer Capacitor/Capacitance
EDX	Energy-Dispersive X-Ray Spectroscopy
EIS	Electrochemical Impedance Spectroscopy
ESR	Equivalent Series Resistance
EV	Electric Vehicle
FTIR	Fourier Transform Infrared Resonance Imaging
GCD	Galvanostatic Charge/Discharge
GHG	Greenhouse Gas
HER	Hydrogen Evolution Reaction
HEV	Hybrid Electric Vehicle
HOMO	Highest Occupied Molecular Orbital
ICE	Internal Combustion Engine
LIB	Lithium-Ion Battery
LUMO	Lowest Unoccupied Molecular Orbital
MOF	Metal Organic Framework
MO	Metal Oxide
NMR	Nuclear Magnetic Resonance Imaging
OME	Organic Molecule Electrode
PANI	Polyaniline
PC	Pseudocapacitor/Pseudocapacitance
PDI-DAQ	N,N′-bis(2-anthra-quinone)]-perylene-3,4,9,10- tetracarboxydiimide
PEDOT	Poly(3,4-ethylenedioxythiophene)
PI	Polyimide
PPA	Poly-perylene-3,4,9,10-tetracarboxydiimide-anthraquinone
PPy	Polypyrrole
PTCDA	3,4,9,10-perylenetetracarboxylic dianhydride
PTh	Polythiophene
rGO	Reduced Graphene Oxide
SEM	Scanning Electron Microscopy
TGA	Thermogravimetric Analysis
TMN	Transition Metal Nitride
TMO	Transition Metal Oxide
XRD	X-Ray Diffraction
XPS	X-Ray Photoelectron Spectroscopy
2-AAQ	2-aminoanthraquinone

Symbols

A	Amperes
cm^{-1}	Wavenumber
D	Crystalline Size
$\bar{e}$	Electron
E	Potential
E°	Standard Reversible Potential
E_p	Peak Separation Potential Difference
eV	Electron Volts
F	Farad
i	current
K	Scherrer Constant
M	Molar
V	Voltage
v	Scan Rate
n	Number of Electrons Transferred
ppm	Parts Per Million
R	Universal Gas Constant
RHE	Reversible Hydrogen Electrode
T	Temperature
W	Watt
β	Line Broadening at Half Maximum
Ω	Ohm
θ	Bragg Diffraction Angle
ΔV	Potential Window

Declaration of Authorship

I, Arjun Rego, declare the thesis presented here, "Development of Redox-Active Organic Electrodes with Low-Cost Carbon Black for High-Performance Supercapacitors for Electric Vehicle Applications," is my own work.

Coauthor Contributions

PDI-DAQ (Chapter 3)

Elliot Evans – Collected electrochemical data and synthesized material under the direct supervision of Arjun Rego (2023); Performed Dunn's Test (2023)

Navid Noor – Fitted EIS models (2024)

Storm Gourley – Collected XRD data (2023)

Amirhossein Foroozan Ebrahimy– Captured SEM images (2023)

PPA (Chapter 4)

Navid Noor – Fitted EIS models (2024)

Storm Gourley – Collected XRD data (2023)

Amirhossein Foroozan Ebrahimy – Captured SEM images (2024)

Shayan Angizi – Fitted XPS curves from experimental data (2024)

CHAPTER 1

1. Introduction

1.1 Climate Change and the Transportation Sector

1.1.1 CO_2 Emissions and Rising Global Temperatures

Global warming has been on the rise for decades and has roughly increased by 1°C since the late 1800s.[1] Much of this can be attributed to the effects of global greenhouse gas (GHG) emissions, largely CO_2,[2] which have been on the rise for decades, increasing by roughly 1% over the past decade.[3] GHGs trap heat from escaping back into space and are necessary to help Earth maintain habitable temperatures, however the excessive GHG production from human activities has proved detrimental to the Earth's overall health .[2] While this increase has largely been due to the accelerating industrialization and urbanization occurring worldwide, it has also brought upon global warming, ocean acidification, desertification, rising sea levels, and drought, to name a few.[2] The consequences observed from GHG emissions further extends to decreases in agricultural output and disturbance of the natural ecosystem (e.g., wildlife extinction, burning of Amazon forests, decrease in plant life available to absorb CO_2).[2] With these realities in mind, it is vital to identify the major sources of CO_2 emissions worldwide and develop strategies to move towards net-zero emissions goals.

1.1.2 Transportation Sector Contribution to Climate Change

With the exception of the brief two-year decrease of GHG emissions during the COVID-19 pandemic, there was a swift rebound in 2022 which reached a record high of more than 36.8 Gt of CO_2 equivalents, compared to less than 5 Gt back in 1900.[4] While numerous sectors make up these growing CO_2 emissions statistics, the transportation sector alone makes up for approximately a third of it,[5] not far behind the industry and power sectors.[4] Although a reduction in CO_2 in

sectors such as industry and building have been observed in recent years, the transport sector emissions increased by 2,1% (137 Mt) in 2022.[4] Despite this increase, the emissions are estimated to have been about 13 Mt higher if it had not been for the increasing use of low-carbon vehicles, such as electric vehicles (EVs) which made up more than 14% of vehicle sales worldwide.[4]

1.1.3 Electric Vehicles, Lithium-ion Batteries, and Regenerative Braking

Global EV adoption has in part been attributed to the efforts governments have made around the world to incentivize the use of EVs which has promoted automotive manufacturers to start adopting EV and hybrid EV (HEV) models into their fleet of vehicles.[6] Many countries have set targets requiring all new light-duty vehicles offered to be zero-emissions in the years to come, such as Canada who made the target for 2035.[7] The US Department of Energy conducted a study which determined that the well-to-wheel emissions produced by EVs sits at approximately 5-fold lower than the emissions produced by an internal combustion engine (ICE) vehicle on average, however this varies by area depending on the source of electricity.[8] One of the major challenges of popularizing EVs has been the costs and technology around them, including vehicle range and battery life.[6] This makes it imperative to research new avenues to pursue for lowering costs, increasing range, and preserving battery life.

Lithium-ion batteries (LIBs) currently dominate the EV market and are essential to its success with high energy densities, good lifespan, and low self-discharge rates, just to name a few.[9] While they have been heavily optimized for EVs, shortcomings remain such as struggles to deliver the high power outputs (high rate discharging) that are inherent to driving conditions (i.e., acceleration), which cause substantial degradation of the LIB over time, shortening their

lifespan.[9] High rate charging/discharging can cause lithium plating on the graphite anode and irreversible lithium phase changes at the cathode that increases the cell resistance.[10] On the larger scale, this potentially increases operating costs of owning an EV if battery replacement becomes necessary, making them less desirable to consumers.[9]

Most EVs use regenerative braking to capture energy dissipated during braking and use it to recharge the batteries for subsequent use, increasing the range capable of the EV.[9]
However, when charging the LIBs using regenerative braking, some of the energy produced from braking is intentionally not recaptured to protect the batteries from charging at high rates. This is because absorbing the energy in such a short time frame can cause degradation similarly to what is observed when subjecting batteries to high discharging rates.[10]

1.2 Supercapacitors Background

1.2.1 Supercapacitor Integration Opportunities with Batteries for EVs

On the other hand, there is another type of energy storage devices known as supercapacitors which share many similarities with batteries such that they store and release energy and have gained attention in the EV industry because of their potential to fill the performance gaps of lithium-ion batteries.[11] Supercapacitors can achieve faster charging and discharging rates (higher power densities) than batteries. This means they have the potential to perform tasks such as absorbing more of the energy dissipated during braking to significantly increase its range and assist the battery during power delivery demand during peak power demands (i.e., acceleration) to avoid battery strain from high rate discharging, prolonging battery life.[12]

This hybridization system is more than just a concept, as it has been implemented over the past decade into EV systems. AFS Trinity Power Corporation was the first company to commercialize battery-supercapacitor hybrid technology.[12]

1.2.2 Supercapacitor Fundamentals

Fundamentally, a supercapacitor contains two electrode plates separated by an electrolytic solution to hold a charge, unlike a traditional capacitor which separates electrode plates by a dielectric. Supercapacitors have a higher power density than batteries, meaning they can deliver more energy in a shorter period per unit volume of material than a battery, however they hold much less energy in that same unit volume. From a more technical standpoint, they differ from batteries in the way they are set up. A traditional supercapacitor typically relies on high surface area materials and hold a charge between two plates with a dielectric to separate that charge between them.[11] However, there are 2 main types of supercapacitors separated based on their charge storage mechanism:

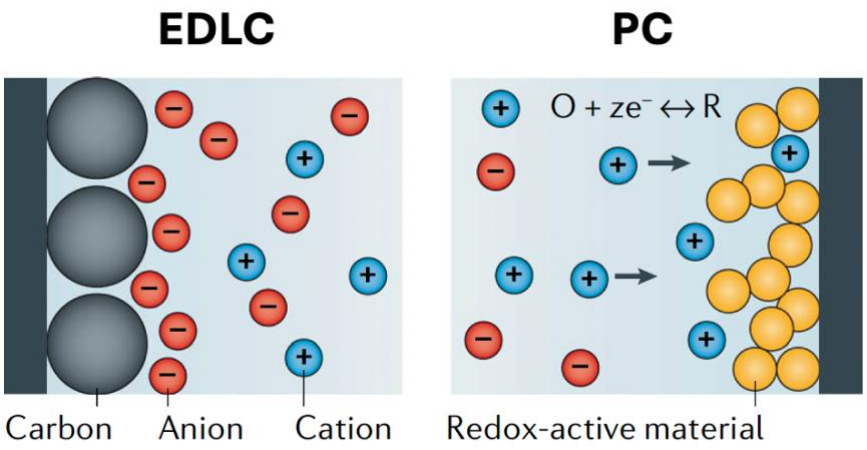

Figure 1: Basic schematic of EDLC and pseudocapacitive charge storage mechanisms, as illustrated in [13]. O and R represent oxidized and reduced species, respectively, while ē represents an electron and z refers to the number of electrons transferred in the faradaic process.

1.2.2.1 EDLC

The first mechanism is the electric double layer capacitor (EDLC) (**Figure 1**),which stores charge through electrostatic charge adsorption and separation at the electrode-electrolyte interface, a location known as the Helmholtz double layer.[11], [13] EDLCs do not utilize faradaic reactions, meaning there are no net electron transfers causing oxidation or reduction of materials. EDLC holds a significant advantage compared to batteries of much higher power densities for faster charging and discharging due to negligible mass transfer limitations, while also being extremely durable during repeated cycling.[11]

1.2.2.2 Pseudocapacitors

The second is the pseudocapacitor (PC), which utilizes fast reversible oxidation and reduction reactions of materials close to or at the surface of the electrode to store and deliver energy (**Figure 1**). Thus, the PC has faradaic reactions, like a battery. The main advantage of PCs compared to EDLCs is that the redox reactions store much more charge than electrostatic charge adsorption, resulting in a PC typically having capacitances an order of magnitude higher than EDLC, thus having a higher energy density that is more competitive with batteries.[11] The drawback with them are they have lower cycling stability than EDLC. Combining the charge storage mechanisms of both supercapacitor types gives rise to a third, the hybrid capacitor, which uses both electrostatic and electrochemical energy storage to simultaneously provide higher energy and power densities while also having higher cycling life than a purely pseudocapacitance-based supercapacitor. Exploring materials with PC mechanisms for hybrid capacitors provides the opportunity to enhance the performance and practicality of EVs through exceling in the areas where batteries face limitations.

1.3 Supercapacitors – State of the Art

1.3.1 Carbon Substrates

There are numerous types of carbon materials used as the primary EDLC component in hybrid capacitors as well as to provide the increased electrical conductivity for the pseudocapacitive material for improved electrochemical performance, translating to higher specific capacitances.[11] The carbon acts as a conductive path for electrons to flow to and from the pseudocapacitive material, while also providing EDLC contributions.[11] Common EDLC materials to use are activated carbon (AC), carbon nanotubes (CNTs), graphene, carbon aeorgels, and carbon black (CB).[11] AC is one of the most common, used in most energy storage devices because of its good conductivity, low cost, and control of pore sizes (5-50 nm).[14] Graphene is made of monolayers of carbon and is another common EDLC material.[14] It is flexible, has great electrical and thermal conductivity, as well as mechanical and chemical stability, making it a top contender as a supercapacitor material. However, it comes at a much higher cost than AC. Carbon aerogels are extremely light carbon materials with high surface areas, however they are brittle and subject to cracking.[14] CB is a less commonly used EDLC material in supercapacitors as although it is electronically conductive, it is less so than AC or graphene.[15] CB is similarly modifiable to AC, has high flexibility allowing for squishable electrically conductive networks, which is quintessential in energy storage devices such as supercapacitors and batteries for durability. CB's most desirable quality is being by far both the cheapest and most abundant nanocarbon currently available on the market. Ketjenblack® is a brand of CB that provides very pure mesoporous CB with BET specific surface areas up to 1400 m^2 g^{-1} and higher electrical conductivity than other CBs.[15], [16]

1.3.2 Pseudocapacitive Materials

1.3.2.1 Metal Supercapacitor Materials

Pseudocapacitive supercapacitor materials are generally split into two broad categories, metal and organic materials.[11] There is an exhaustive list of the types and combinations of metal-based supercapacitor materials researched, however the most common are transition metal oxides (TMOs). Specifically, cobalt, titanium, ruthenium, iron, manganese, zinc, nickel, and molybdenum oxides, with ruthenium oxide (RuO_2) based electrode materials being very common due to their high specific capacitances, rate capabilities, proton conductivity, cycling life, and potential window. While RuO_2 based supercapacitors have been able to deliver up to 1300 F g^{-1}, the biggest limitation for application is that ruthenium metal is costly and environmentally toxic. While there are less toxic and cheaper options such as nickel, zinc, and iron oxides which have been researched heavily and shown potential for applications as supercapacitor materials, issues with some such as poor conductivity, metal agglomeration during cycling, and complicated tuning of materials to achieve the desired oxide phase limit the practical applications. Metal organic frameworks (MOFs) which consist of metal oxide (MO) materials chemically bonded with carbonaceous materials to achieve 3-dimensional redox-active units with very high specific surface areas. While MOF specific surface areas are appealing, there are still conductivity challenges, degradation at high rates, and difficulties with diffusion of electrolyte ions into the material due to the high degree of crystallinity. Transition metal nitrides (TMNs) are another metal subcategory that attempts to improve the conductivity and cycling stability of pseudocapacitive materials. Metal-nitrogen bonds form through a mixture of covalent, ionic, and metallic bonding, creating crystal lattices with higher electrical conductivity and better redox activity than TMOs, making them more promising alternatives for supercapacitor applications. Leading TMNs in research are vanadium,

titanium, molybdenum, and niobium. Despite these advancements in metal-based supercapacitor research, the issues that they cannot currently overcome is the high cost of metals and being considered non-renewable resources, making the long-term availability of metals more finite.

1.3.2.2 Organic Supercapacitor Materials

Although not a new concept, an emerging field of research with organic materials, specifically redox-active conducting polymers (CPs), have been explored for high-performance supercapacitor applications.[11] The most apparent advantages of organic over metal candidates are their environmental friendliness, renewability, better processability, lower cost, easier syntheses, mechanical flexibility, and EDLC contributions in addition to pseudocapacitance. CPs also have high theoretical capacitances. However, a drawback is that redox-active CPs often struggle with their cycling stability due to swelling and shrinking of the material during charging and discharging.[17] The CPs mainly explored are few, such as polyaniline (PANI), polypyrrole (PPy), and polythiophene (PTh), leaving large gaps in the literature to report the performance of more novel CP supercapacitor materials and optimizing their capabilities. PANI is by far the most researched CP in research with capacitances of the pure material up to 115 F g^{-1} and PANI with reduced graphene oxide (rGO) up to 1182 F g^{-1}.[11] PANI, like other CPs, suffers from cycling instability issues and often reports capacitance retention after only 1000 cycles, rather than testing them to 5000 or 10000 cycles which is more commonly reported in metal-based supercapacitor research. PPy has slightly lower specific capacitances than PANI and higher self-discharging.[18] Poly(3,4-ethylenedioxythiophene) (PEDOT) is a PTh derivative CP with high electrical conductivity, but low electrochemical activity resulting in low specific capacitances, rate capability, and cycling stability, the latter largely due to high swelling and low mechanical stability.[18] While PANI reigns supreme of the scare options of CP, there clearly exists a large

gap in terms of CP choices for further supercapacitor research to identify the ideal physical and chemical properties for applications of CPs.

1.4 Polyimides

1.3.1 Advantages/Opportunities for Supercapacitors

Polyimides are a class of polymers with repeating imide bonds linking monomeric units together. They are praised for having an impressive combination of high chemical resistance, mechanical flexibility, and thermal stability, while having good electrical energy storage properties.[19] Their inherent nitrogen-containing backbone negates the need for additional n-doping modifications which currently pose as a difficulty for traditional CPs [19], [20]. The nitrogen backbone also helps improve the wettability of the material which is advantageous for use in aqueous electrolytes. Furthermore, PIs can have extended π-conjugated structures, as shown in research by Zhao et. al, [20] and Jiao et al,[21] which provides the opportunity for them to be considered CPs. Polyimides have been minimally focused on as pseudocapacitive materials in supercapacitor research, although they have been studied in aqueous rechargeable metal-ion batteries.[20]

1.3.2 General Synthesis

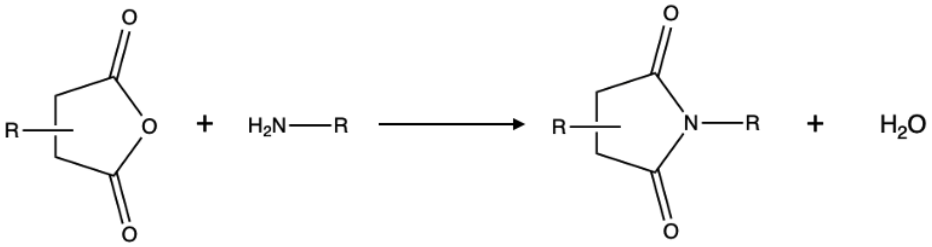

Figure 2: General formation of an imide bond from an anhydride and primary amine functional group.

Imide bonds are typically synthesized by reacting molecules with an anhydride and amine functional groups (**Figure 2**).[19] Reacting a dianhydride and diamine can allow for repeated imide bond formation, forming a polyimide. The reaction proceeds where the amino nitrogen reacts with one of the anhydride's carbonyl groups to break the ring, followed by a second reaction with the other carbonyl group to undergo an intramolecular cyclization process to form the imide bond, leaving two H_2O molecules as by-products.[19], [22]

1.3.3 Introducing PPA and PDI-DAQ

PI monomers can have redox-active groups with high redox reversibility, as demonstrated by dianhydrides such as 3,4,9,10-perylenetetracarboxylic dianhydride (PTCDA), which is a π-conjugated, semi-conductive organic molecule with a planar structure allowing for π-π bond adsorbing to conductive carbons.[23] On its own, it struggles with dissolution in electrolyte and anhydride group instability, resulting in very poor cycling.[24] However, co-polymerization with a redox-active, π-conjugated diamine can make an extended π-conjugated PI with high energy densities, such as that of Jiao et al [21], who used 2,6-diaminoanthraquinone (DAAQ) to create a high-performance supercapacitor material, poly-perylene-3,4,9,10-tetracarboxydiimide-anthraquinone (PPA). This material showed exceptional performance with a specific capacitance of 245 F g^{-1} at 5 mV s^{-1}, higher than that reported of pure PANI (115 F g^{-1} at 1 mV s^{-1}).[11]

Despite PI's numerous physical and chemical advantages, they have been commonly held back for supercapacitor research because they are generally highly insulating materials which translates to poor electrochemical performance.[19] However, Jiao et al demonstrated how the π-conjugated PPA even on its own can achieve higher capacitances than the research-leading PANI.[21] Its high

electrochemical performance combined with the inherent advantages seen in PIs make it a promising candidate for continued research as a novel supercapacitor material.

In the exploration of PPA, a modified version of the material was made consisting of only 3 monomeric units to make up a trimer, known as N,N′-bis(2-anthra-quinone)]-perylene-3,4,9,10-tetracarboxydiimide (PDI-DAQ). Where polymeric materials are known to swell and shrink during cycling, limiting their cycling stability, small organic molecules such as PDI-DAQ may be less susceptible to these drawbacks due to their smaller molecule size.[25] Many small organic molecules face challenges with dissolution in aqueous electrolytes which can further limit their cycling stability and performance, however PDI-DAQ has been reported as insoluble and has demonstrated fast and reversible redox-activity in battery research.[26]–[29] Pursuing the PPA trimeric analogue, PDI-DAQ, aimed to identify the electrochemical strengths of both insoluble small organic molecules and polymers incorporated with CB.

1.5 Objectives

From the literature review in sections 1.3.2.1 and 1.3.2.2, there is a clear need to explore organic supercapacitor materials that exhibit PC mechanisms due to the high costs and toxicity of many metals. While redox-active polymer materials have led organic supercapacitor research, few of them have been explored. With the wide array of organic materials available, such as redox-active quinone molecules, there remains untapped potential for revolutionary organic supercapacitor materials to be discovered and opportunities for advancements in the energy storage industry.

The underexplored potential of polymer materials, such as polyimides (as discussed in Chapter 1.4), motivates this research to highlight polyimide materials as contenders for supercapacitor applications.

This thesis focuses on the synthesis and optimization of the polymer, PPA, and the trimeric analogue, PDI-DAQ. While PPA has previously been tested as a supercapacitor material by Jiao et al, it did so with an expensive carbon material (reduced graphene oxide) that required more intensive electrode preparation steps.[21] In this research, PPA aimed to be presented with capacitance, cycling stability, and rate capability values competitive with the previously published work, however using a very low-cost carbon material, carbon black, and additionally modifying the synthesis of PPA to identify more optimal PPA electrode preparations for a higher performing supercapacitor. Further, identifying the exact degradation mechanisms of PPA was pursued to provide more insight for future research to mitigate performance degradation over prolonged cycling. The research on PDI-DAQ as a supercapacitor electrode material was performed to learn about the experimentally observed differences a shorter chained analogue of PPA could have on the performance of a supercapacitor. Identifying the optimal performance metrics of PPA and PDI-DAQ with carbon black, as well as the energy storage differences between both materials in similar setups was a major objective of this thesis work. Together, these objectives contribute to filling the gaps in organic supercapacitor research by providing information on opportunities polyimide materials hold for supercapacitor applications by demonstration of the electrochemical capabilities of PPA and PDI-DAQ, providing comparative data to highlight the effects of molecule size on the performance, and demonstration of modified PPA synthesis techniques to improve the cycling stability of the material.

CHAPTER 2

2. Methodology

2.1 Electrochemistry Fundamentals

2.1.1 Oxidation and Reduction Concepts

Oxidation is the process of a substance losing electrons during a reaction, while reduction is the process of substance gaining electrons during a reaction. In the example below, R represents a reduced species, while O represents the oxidized species, and ē represents an electron.

Oxidation: $R \rightarrow \bar{e} + O$

Reduction: $O + \bar{e} \rightarrow R$

2.1.2 Capacitance

Capacitance is a measure of the ability for a substance to store an electrical charge over a given voltage range,[30] which is given in a unit known as the Farad (F). To compare the performance of different active materials in supercapacitors, most often the capacitance is reported as a specific capacitance by mass (F g^{-1}).

2.1.3 Energy Density and Power Density

Energy density (Wh kg^{-1}) is an important metric that describes the amount of energy a material can hold per unit mass,[30] and is given by the formula:

Equation 1: $$E = \frac{1}{2}CV^2$$

Where E is the energy density, C is the capacitance, and V is the operating voltage window. This formula shows the importance of a supercapacitor material to have a wide operating voltage window, as it has positive exponential increase on the material's energy density.

Power density (W kg^{-1}) is another important metric that describes how much power can be delivered per unit mass,[30] and is given by the formula:

Equation 2:
$$P = \frac{V_{charged}^2}{4R_S}$$

Where P is the power density, $V_{charged}$ is the charged potential, and R_s is the equivalent series resistance (ESR), which is affected by the intrinsic electronic resistance of the material as well as the contact resistance of the material and current collector. The ESR is commonly determined through electrochemical impedance spectroscopy (EIS), which is explained in the next section.

As described earlier, batteries are known to have very high energy densities and low power densities, while capacitors have very high-power densities and low energy densities. Supercapacitors incorporating EDLC and pseudocapacitor charge storage mechanisms help bridge the gap to achieve higher energy densities, although still much lower than that of the lithium-ion battery used in EVs. The Ragone plot shows the relationship between energy and power densities of different energy storage devices (**Figure 3**).

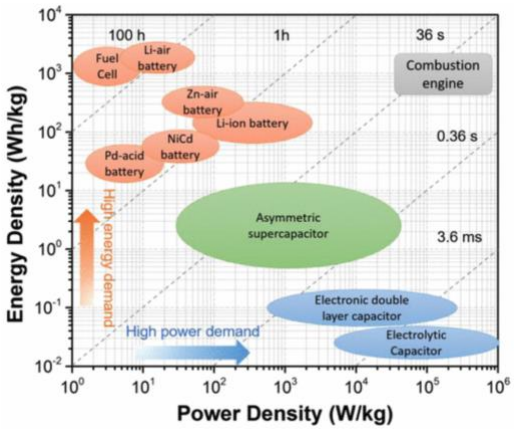

Figure 3: Ragone plot depicting the approximate power density and energy density of different energy storage devices. The times reported represent the discharge time, calculated by dividing the energy density by power density, as illustrated in [30].

2.2 Potentiostat

A potentiostat is an essential device in electrochemistry that applies a potential to the electrochemical setup relative to a reference electrode that has a standard potential.[31]

2.3 Three-Electrode Electrochemical Cell

There are two main types of cell setups for supercapacitors: three-electrode and two-electrode cells.[30] While two-electrode cells more closely replicate the realistic performance of the material in a supercapacitor, the three-electrode cell is very useful for understanding the electrochemical performance and properties of the materials. The three-electrode cell setup was used for the work described in this thesis (**Figure 4**). The three-electrode cell consists of:

2.3.1 Working Electrode

This electrode contains the material of interest and is what the potentiostat applies a potential to in relation to the reference electrode.[31] The working electrode used in this work was made of glassy carbon for its negligible capacitance contributions and inert redox activity.

2.3.2 Reference Electrode

This electrode has a defined and stable equilibrium potential that the potentiostat uses as the standard reference point for the potential it applies to the working electrode.[31] The Ag/AgCl electrode is used in this work and is a very commonly used reference electrode in electrochemistry. The electrode has an inner junction containing a silver wire with 4 M KCl and an outer junction in 10% KNO_3.[32] Only the outer junction has contact with the cell's electrolyte and is separated by a ceramic frit. This double junction setup avoids chloride contamination in the electrolyte over time.

2.3.3 Counter Electrode

While at the working electrode there is a potential applied from the potentiostat to induce oxidation and reduction processes (or electron adsorption and desorption for EDLC), the electrons must flow to and from the counter electrode to complete the circuit. The counter electrode used in this work is a graphite (carbon) rod, however platinum wire is another commonly employed material used in electrochemical research.[31]

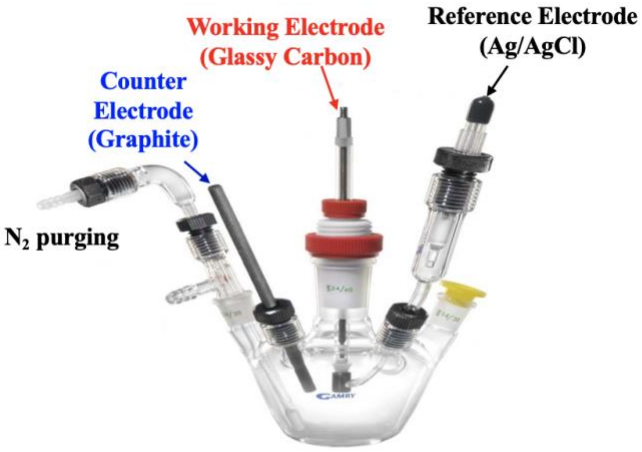

Figure 4: Schematic of three-electrode setup used during electrochemical experimentation.

2.4 Symmetric and Asymmetric Supercapacitors

Another setup parameter for a supercapacitor is whether it is symmetric or asymmetric. Symmetric supercapacitors have the same electrode materials at both electrodes which generally limits the potential window. Asymmetric supercapacitors have the electrodes made of 2 different types of materials, helping to take advantage of their individual potential windows to increase the overall potential window available.

2.5 Electrochemical Measurement Techniques

2.5.1 Cyclic voltammetry (CV)

CV is an electrochemical technique relating applied potentials on the x-axis to current response on the y-axis. The potentiostat delivers a sweep from one side of a given potential window to the other, followed by a reverse sweep back to the starting potential.[31] The rate at which this sweep occurs is called the scan rate (in units of mV s^{-1}). The oxidation and reduction of species is shown by peaks that occur at potentials specific to their reaction that can be quantified by the Nernst equation:

Equation 3: $$E = E^o + \frac{RT}{nF} \ln\left(\frac{(Ox)}{(Red)}\right)$$

Where E is the electrochemical cell potential, E^o is the species' standard potential, F is Faraday's constant, R is the universal gas constant, n is the number of electrons transferred, and T is temperature, with the ratios of the relative activities of the oxidized and reduced species denoted Ox and Red, respectively. As the potential changes throughout the CV in either direction, the concentration of the oxidized and reduced species also changes based on the Nernst equation. The current peak observed is due to the rate at which the electroactive species in question is being reduced/oxidized. For instance, take the reduction of the following species:

Equation 4: $$C{=}O + H^+ + \bar{e} \rightarrow C\text{-}OH$$

C=O is being reduced at the working electrode to C-OH and is being kinetically controlled by the availability of H^+ in the electrolyte. Approaching the potential at which reduction occurs, C=O begins reducing to C-OH at an increasing rate. At the current peak there is a high H^+ availability from the bulk electrolyte and thus the highest rate of reduction. As the potential continues scanning, there is less available H^+ near the working electrode, resulting in a current drop from the decrease in the rate of reduction and an increasing dependence on H^+ mass transport.

2.5.2 Galvanostatic charge/discharge (GCD)

GCD is another electrochemical technique that is often used to emulate the charge and discharge of a material in a specified potential window with a controlled applied electrical current.[33] "Galvanostatic" refers to a constant applied current, differing from the CV technique which applies a potential and measures the current response. The applied current, often normalized by the electroactive material's mass or electrode surface area, is commonly reported in A g^{-1} or mA h cm^{-2}, respectively.[34] During GCD, the evolution of the voltage of the electroactive material is recorded as a function of time, estimating its charge and discharge rates. A GCD curve is typically characterized by a sloped line with plateaus that correspond to the oxidation and reduction peaks seen in a CV, as previously discussed. Plotting the CV voltage as a function of the integral of the current would provide the same curve profile as a GCD.

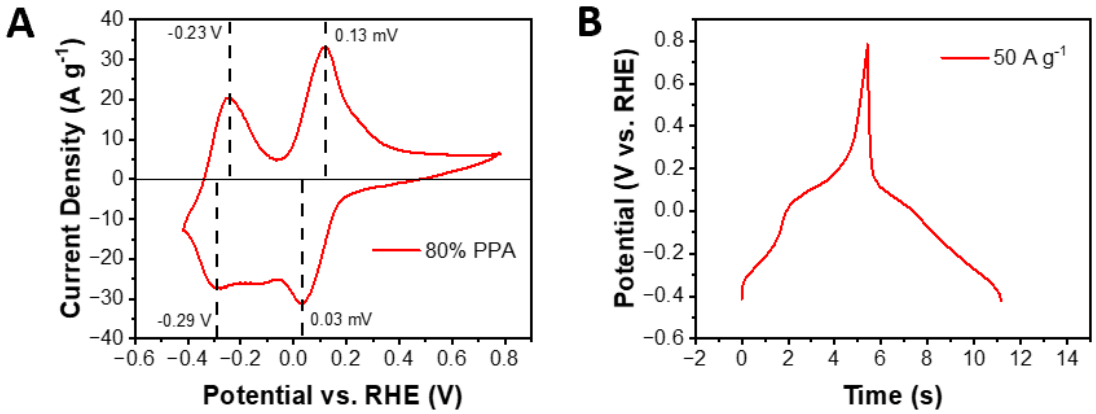

Figure 5: (a) Example of a CV of PDI-DAQ at 50 mV s^{-1} relating potential to current density, with two pairs of redox peaks observed at 0.08/0.05 V vs RHE and -0.21/-0.24 V vs RHE (b) GCD curve of PDI-DAQ at 50 A g^{-1} relating potential to time, showing the slope plateaus that correspond to the potentials at which redox peaks are observed in the CV.

2.5.3 Electrochemical Impedance Spectroscopy (EIS)

In EIS, a sinusoidal alternating current potential is applied to the supercapacitor system which the sinusoidal current response is measured.[35] EIS compares the AC current or voltage output from the supercapacitor system to the input AC current or voltage applied to the system over a range of applied frequencies. EIS measures a material's impedance, which is how a material resists an applied flow of current to the system. This is like resistance, however it does not always follow Ohm's law, as it depends on the applied AC potential frequency.

EIS measurements are most often fitted to an equivalent electrical circuit using a software that simulates the impedance to model a circuit. **Figure 6** below shows the most commonly fitted model for supercapacitor EIS spectra.

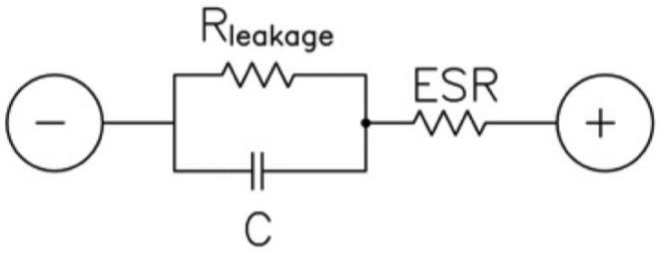

Figure 6: The most common EIS model fitted for a supercapacitor EIS spectra (simplified Randles model), where C is the ideal capacitance, ESR is the equivalent series resistance, and $R_{leakage}$ is the leakage resistance, as illustrated in [36]

Here, there is an equivalent series resistance (ESR) that is calculated, which is the resistance from a combination of the electrodes, contact points, and electrolyte, that causes loss of power during charging and discharging of the supercapacitor.[36] The loss of power is dissipated as heat. A simple equation relating power loss (P_{loss}) to current (I) and ESR is:

Equation 5: $$P_{loss} = I^2 ESR$$

The impedance data collected from EIS is most often presented in the form of a Nyquist plot, which plots the frequency of the applied potential using an imaginary impedance (-imZ) against the real impedance (ReZ) through Euler's formula[37]:

Equation 6: $$Z(\omega) = Z_o(cos\emptyset + jsin\emptyset) = \frac{V}{I}$$

Which is made equal to the ratio of voltage to current.

Figure 7 shows how information about diffusion resistance, charge transfer resistance, and system resistance can be extracted from a Nyquist plot. The lowest x-intercept value is the system resistance, while the width of the semi-circle is the charge transfer resistance and the region following it is the diffusion resistance caused by mass transfer limitations.[38]

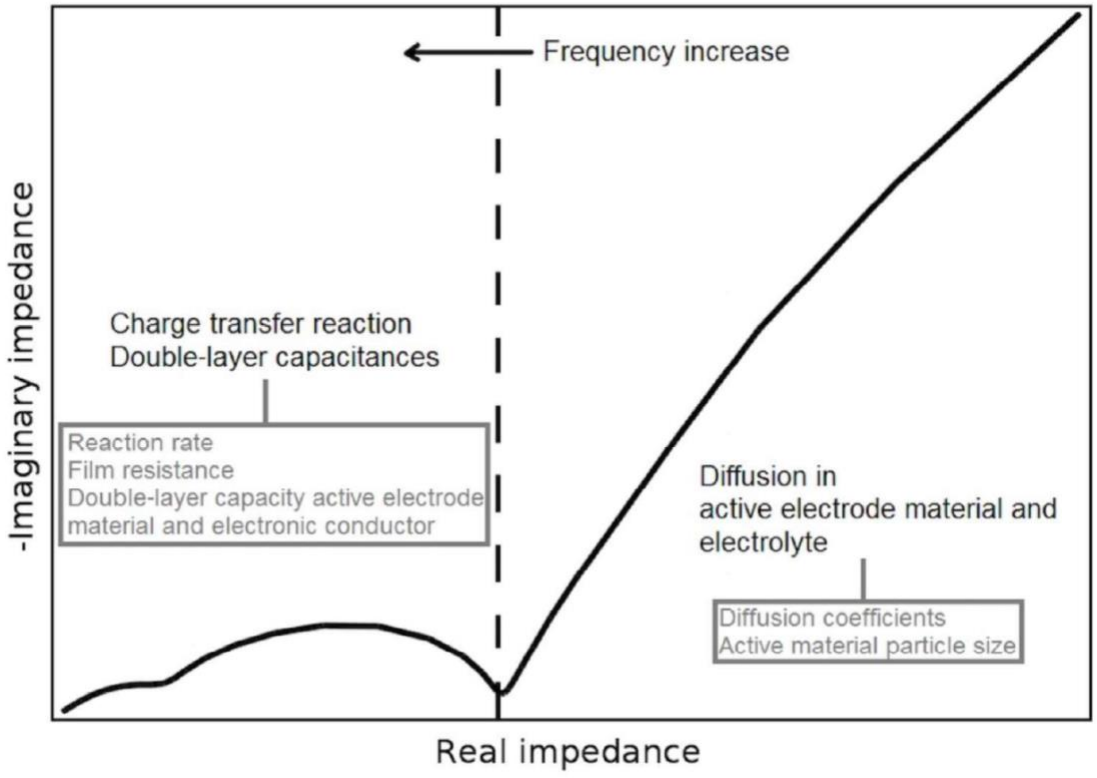

Figure 7: Example of a Nyquist plot and the relation of each region to the types of resistance for the electrochemical setup that can be extracted from it, as illustrated in [38].

2.6 Characterization Techniques

2.6.1 Scanning Electron Microscopy (SEM)

SEM is technique used to capture images of a material at high magnifications to provide information about its morphology, particle size, and uniformity through the use of an electron beam that scan across the sample (otherwise known as “raster”).[39] This beam interacts with the sample in such a way that electrons are then emitted from it to a detector that forms an image. The detector can be set to detect different types of electrons, providing more tailored information about the sample. There are low energy secondary electrons which are produced from very close to the material’s surface, resulting in an image well suited for examining surface morphology closely with high resolution. Back-scattered electrons are higher energy and occur from the beam’s electrons colliding with atomic nuclei, providing a higher contrast image that highlights the differences in atomic mass of the atoms present in the sample. Elements with higher atomic masses will appear brighter, while ones with lower atomic masses will be darker, allowing for qualitative information about the sample’s atomic composition. While there are other types of electrons and X-rays (Auger electrons, X-ray continuum and X-ray fluorescence), secondary and backscattered electrons are primarily used in SEM imaging.

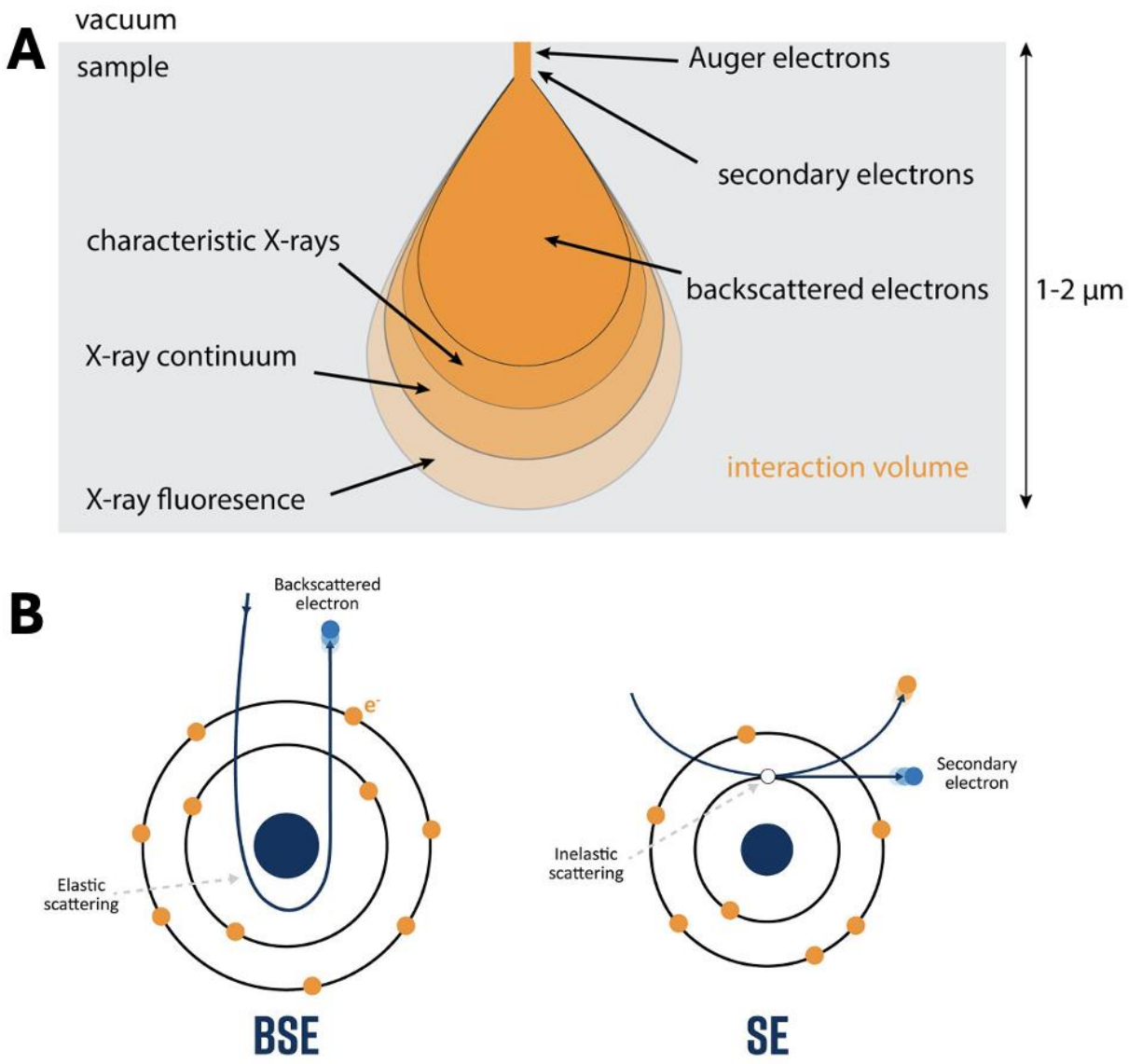

Figure 8: (a) Electron interactions in a sample in SEM. Secondary electrons and backscattered electrons are the most useful electron types in this technique, as illustrated in [40] (b) Schematic of how secondary and backscattered electrons are produced from the sample, as illustrated in [41].

2.6.2 Energy-Dispersive X-Ray Spectroscopy (EDX)

EDX is a technique coupled with SEM that can more quantitatively determine the elemental composition. The SEM beam's electrons enter the sample and can eject the higher energy core-shell electrons, resulting in an electron from an outer shell to relax to the core-shell measuring the

x-rays produced from the sample.[39] The elements generally have discrete x-ray energies produced from these events which make them identifiable using EDX software.

2.6.3 X-Ray Diffraction (XRD)

XRD provides information of the crystal structure of a sample. X-rays are passed through the sample in which scattering or absorption of the x-rays occurs (**Figure 9**).[42] The equations below describe the interactions the x-ray has with the sample:

Equation 7: $$I_f = \frac{I_o K}{r^2}\left(\frac{1+cos^2 2\theta}{2}\right)$$

Equation 8: $$\lambda = 2dsin\theta$$

Where I_f is the scattered beam intensity, I_o is the incident beam intensity, r is the distance measured from I_f, θ is the Bragg angle, and λ is the x-ray wavelength. Bragg law describes the constructive interference that occurs when the x-ray's wavelength is equal to the space between the crystal lattice planes, causing high intensity scattering that can be detected. XRD can help identify the sample by comparing the diffraction patterns of known samples found in databases.

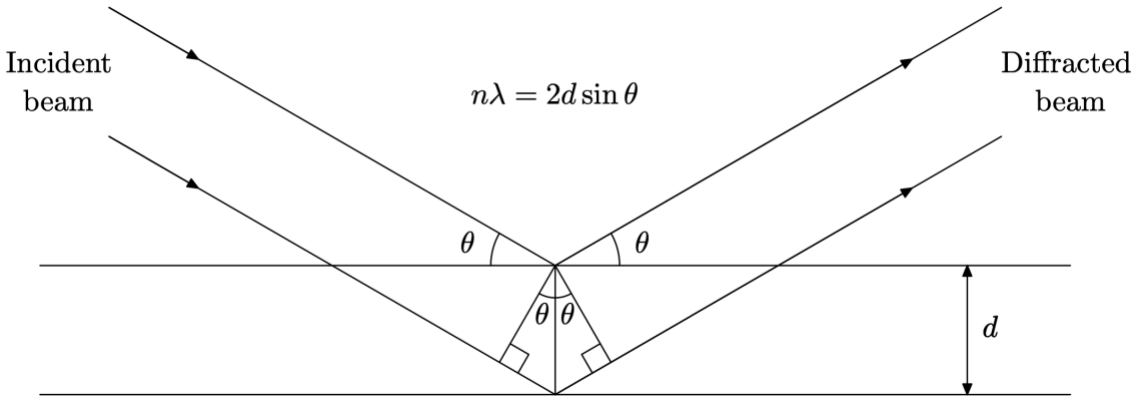

Figure 9: Illustration of Bragg's Law as it applies to XRD samples, as illustrated in [43].

2.6.4 X-Ray Photoelectron Spectroscopy (XPS)

XPS is a surface-sensitive technique that can quantifiably determine the composition and electron structure of samples by applying x-rays to the surface of a solid sample resulting in the emission of electrons coupled with the detection of their kinetic energy.[44] The basis of XPS lies on the concept of the photoelectric effect, in which light could be used to emit photoelectrons (electrons produced from energetic photons striking the sample) from the surfaces of materials. To produce photoelectrons, soft x-rays (< ~6keV) bombard the sample's surface and that energy is discretely transferred to the sample's core-shell electrons, emitting electrons with a binding energy (BE), kinetic energy (KE), and spectrometer work function (Φ_{spec}, a constant) summed to equal to the applied x-ray energy (hv).

Equation 9: $$hv = BE + KE + \Phi_{spec}$$

XPS uses the kinetic energies measured to calculate the binding energies of the electrons participating in chemical bonding in the sample using **Equation 9**. Any electrons with binding energies less than the applied x-ray energy should be emitted from the surface of the sample and detectable. Determining the binding energy of the electrons for each element in the sample can differentiate what the element is bonded to. For example, from the difference in C 1s binding energy analysis in **Figure 10**, the existence of a C-C, C-O, or C=O bond can be distinguished. All elements except for hydrogen and helium can be detected using this technique.

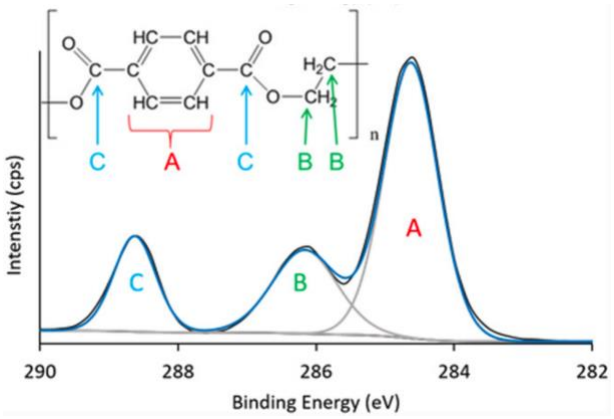

Figure 10: Example of a C 1s XPS of polyethylene terephthalate (PET) and the chemical structure showing the assignment of the three peaks based on binding energy, as illustrated in [44].

2.6.5 Nuclear Magnetic Resonance Imaging (NMR)

NMR is a widely used characterization technique to identify the molecular contents of a sample, including its purity and molecular structure.[45] To understand the fundamentals of NMR, one can consider the most common type of NMR, ^{1}H NMR, which takes advantage of the inherent magnetic moment (μ) that hydrogen produces due to the positively charged nucleus spinning. This is only possible for elements with an odd atomic mass (odd sum of protons and neutrons), to allow for a net non-zero nuclei spin to produce magnetic properties that the NMR spectrometer can affect. The NMR spectrometer has a powerful magnetic field that can cause the nuclei's magnetic field of hydrogen to align with it. The NMR spectrometer releases magnetic pulses at certain frequencies to align the nuclei, and once it relaxes to its usual alignment, it releases an energy that can be detected. The chemical environment of the hydrogen molecule affects which frequencies it responds to, and from this, a spectrum of said frequencies can be used to identify the composition of the sample. This technique is further informative by how the magnetic properties nearby hydrogen molecules can cause splitting of the hydrogen's frequency response. **Figure 11** shows this splitting in the ^{1}H NMR spectrum of ethanol.

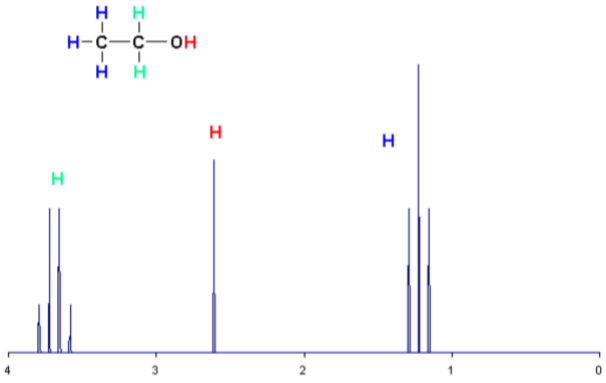

Figure 11: Example of a ^{1}H NMR spectrum of ethanol, as illustrated in [46].

2.6.6 Fourier Transform Infrared Resonance Imaging (FTIR)

In FTIR, continuous infrared (IR) radiation bombards the sample, resulting in its absorption by the molecules which excite rotational and vibrational movements (stretching and bending) of the bonds that can be measured.[47] Molecules with X number of atoms can have 3X degrees of freedom (each atom has the ability to move in an x,y, and z direction). Functional groups are expected to have their own characteristic frequencies for the rotational and vibrational movements FTIR subjects the molecule too, resulting in the ability to distinguish the presence of specific functional groups (e.g., -OH, C=N, -N-H, C=C, C=O, etc.).

2.6.7 Thermogravimetric Analysis (TGA)

TGA is a quantitative technique where the mass of the sample is measured across temperature ranges, providing information about the decomposition of the material. This can occur in air, or in an inert environment (i.e., nitrogen or argon gas).[48]

CHAPTER 3

3. PDI-DAQ

The following paper, "An Organic Trimer Molecule Electrode Material with Low-Cost Carbon Black for Novel Supercapacitor Applications," describes the trimeric organic molecule, PDI-DAQ, as a novel supercapacitor material. PDI-DAQ provides insight into the electrochemical behaviour of insoluble small molecule organic molecules as well as identifying performance comparisons with the polymeric analogue, PPA, in Chapter 4. Details of the implications of this work are described in Chapter 1.

An Organic Trimer Molecule Electrode Material with Low-Cost Carbon Black for Novel Supercapacitor Applications

Arjun Rego, Elliot Evans, Navid Noor, Storm Gourley, Amirhossein Foroozan Ebrahimy, Drew Higgins*

Department of Chemical Engineering, McMaster University, 1280 Main Street West, Hamilton, Ontario, L8S 4L7, Canada.

3.1 Abstract

Quinone-based organic molecules have emerged as promising supercapacitor electrode materials due to their reversible redox activity, high theoretical capacitances, low cost, nontoxicity, and renewability. Quinones are limited by their high solubility in aqueous electrolytes, resulting in low cycling stabilities and electrical conductivity. This work addresses some of these limitations by

proposing a novel quinone-composed material, N,N′-bis(2-anthra-quinone)]-perylene-3,4,9,10-tetracarboxydiimide (PDI-DAQ), as an organic molecule electrode (OME) for supercapacitors. PDI-DAQ demonstrates high capacitances, good cycling stability, and a facile synthesis and electrode preparation method. PDI-DAQ incorporated with a low-cost carbon substrate, Ketjenblack carbon black (CB) into an OME demonstrated a specific capacitance of up to 318.6 F g^{-1} at 5 mV s^{-1} in 1 M H_2SO_4 electrolyte at an optimized weight ratio of 1:1 PDI-DAQ to CB. This OME had a cycling stability of 61.2 % after 10,000 cycles. PDI-DAQ successfully demonstrates the advantages of covalently bonding organic molecules with multiple redox-active functional groups to create a pseudocapacitive supercapacitor material with a simple preparation for an OME.

Keywords: Insoluble organic material; Quinone; PTCDA; 2-AAQ; PDI-DAQ; Energy storage, Pseudocapacitance; Low-cost carbon black; High performance; Good cycling stability

3.2 Introduction

Energy-related CO_2 emissions reached a new high in 2022 with a 423 megaton increase in emissions alone from energy combustion.[1] The transportation sector alone accounts for about a third of the global CO_2 emissions.[2] In an effort to decarbonize this sector, many automotive manufacturers have adopted electric vehicle (EV) and hybrid EV (HEV) models into their catalogues.[3] A study by the US Department of Energy determined that on a national average, the well to wheel emissions produced by EVs is approximately 5-fold lower than that of internal combustion engine vehicles.[4] The EV market is currently dominated by lithium-ion batteries (LIBs) energy storage large owing to their high energy density which is needed for longer driving ranges, however, LIBs are still limited in their application space due challenges with low power density, long term stability, and low charging rates.[5] For example, regenerative braking is

commonly employed in EVs to recover energy dissipated during braking, however due to the low power density of LIBs, much of this energy is wasted.[6] On the other hand, supercapacitors are an established class of electrochemical energy storage devices capable of faster charging and discharging rates than a battery, accompanied by longer lifetimes.[7], [8] Supercapacitors can operate in tandem with batteries as a part of EV power systems to not only capture a higher percentage of energy during braking, but also to modulate high power demands (i.e., accelerating) while the battery pack provides the energy needed to enable long driving ranges.[9],[10]
This can avoid LIBs from high rate charging which can cause accelerated degradation and reduce the overall lifetime of the LIB system. [6] Clearly, there is a need for both energy dense batteries and power dense supercapacitor technologies to meet expectations of next generation of EVs.

Supercapacitors can be divided into two main groups based on the mechanism of charge storage. The first mechanism, electric double layer capacitance (EDLC), utilizes electrostatic charge adsorption via charge separation at the interface of the electrode and electrolyte, a location known as the Helmholtz double layer. [11] EDLC provides high power densities as well as rapid charging and discharging, attributed to negligible mass transfer limitations in the system. The second mechanism, pseudocapacitance (PC), relies on faradaic oxidation and reduction (redox) reactions close to or at the surface of the electrode.[12] Supercapacitors made with materials exhibiting PC mechanisms tend to have higher energy densities than those with EDLCs and are very similar in concept to batteries; however, the redox reactions occurring in PC supercapacitors are significantly faster and much less diffusion limited than the equivalent redox reactions occurring in conventional lithium-ion battery chemistries.[12]

In determining an effective supercapacitor, it is critical to maintain a high energy density without sacrificing power, a long cycling stability, and a large capacitance. Beyond performance,

any commercially viable supercapacitor needs materials that are low cost and environmentally friendly. These criteria have steered research towards organic materials, which combine simple synthesis and inexpensive materials to form effective supercapacitors.[13] Most organics research so far has targeted conductive polymers (CPs), which have facile synthesis pathways, high possible energy densities and have high pseudocapacitive capabilities owing to their redox activity.[14] To date, there are only a few substantially explored CPs for supercapacitors, such as polyaniline (PANi), polypyrole (PPy), and polythiophene, despite there being a wide variety of structures to be considered. [15], [16] However, CPs have intrinsic conductivity limitations, substandard power densities, and undesirable cycling stability.[14], [17] Degradation of CPs is often attributed to the repeated insertion/de-insertion of ions leading to swelling and shrinking of the material during while cycling leading to mechanical degradation.[15], [18] Their large molecule sizes paired with their conductivity limitations also result in less efficient charge transfer kinetics when incorporated with a conductive carbon substrate (i.e., rGO, CNTs, carbon black), due to the formation of large non-conductive areas between the carbon matrix. [19] In response to these challenges, another branch of research has begun to focus on organic small molecule electrodes (OMEs). An OME is a composite material containing an organic molecule bound to a conductive carbon substrate; this carbon compensates for the poor conductivity and cycling stability inherent to small molecules while also increasing the electrode's surface area and structural strength.[16], [18] Compared to CPs, OMEs offer clearer characterization and better tunability, allowing for more insight into the properties of the chosen molecule.[13], [20] As lighter organic molecules, they are also easily synthesized and environmentally sustainable.[21] Thus, OMEs are a material that holds much promise due to their ecological neutrality, high tunability, and accessible syntheses.

Quinones are a class of organic materials that are considered promising candidates for incorporation in OMEs due to the redox activity, low cost, and ease of structural modifications).[18] Covalently bonding quinones has become a popular alternative in literature, particularly the formation of polyimides and polythioethers.[22] Perylenetetracarboxylic dianhydride (PTCDA) and 2-aminoanthraquinone (2-AAQ) are quinones with multiple conjugated carbonyl groups capable of performing in redox reactions.[23] Unfortunately, they too suffer from conductivity limitations and poor cycling stability primarily due to dissolution in the electrolyte.[23]–[25] Zhao et al., researched polymerizing PTCDA with diamine alkyl chain moieties for supercapacitors to improve cycle life and rate capability, however, the alkyl linker molecules caused disruptions in the p-conjugated network which can inhibit the polyimide's intrinsic conductivity and redox kinetics.[26], [27] Using inspiration from the benefits of polymerizing quinones in literature, covalently linking two 2-AAQ molecules to PTCDA via imide bonds was hypothesized to mediate dissolution and increase charge transfer kinetics of the material.[28] The resultant molecule, termed N,N′-bis(2-anthra-quinone)]-perylene-3,4,9,10-tetracarboxydiimide (PDI-DAQ), has demonstrated insolubility and improved stability as a cathode in organic electrolytes in battery research while maintaining redox activity.[27]–[29] The higher molecular weight of PDI-DAQ compared to the monomeric counterparts makes this molecule insoluble in aqueous electrolytes, improving its stability, and preserving its original redox active sites to achieve a 6-electron transfer mechanism per molecule, thereby allowing for a higher energy density (**Figure 1b**).[27] PDI-DAQ also retains a p-conjugated network, while adding additional redox-active moieties to the structure.[27]

When considering carbon substrates to use, it is key to consider cost, surface area, mechanical strength, and conductivity. These factors lead to a selection of materials commonly explored for

supercapacitors including graphene/graphene oxide, carbon black, and carbon nanotubes (CNTs). [30], [31] [32], [33]. Carbon black was chosen as the carbon substrate for PDI-DAQ for its low cost, high surface area (800 m^2 g^{-1}), and ease of preparation.

In this paper, we report the novel application of PDI-DAQ as a supercapacitor OME exhibiting high capacitances up to 318.6 F g^{-1} at 5 mV s^{-1} in 1 M H_2SO_4 using a low-cost conductive carbon black material, Ketjenblack, through a facile synthesis and electrode preparation method. The cycling stability was 61.2 % after 10,000 cycles at a very high CV scan rate of 100 mV s^{-1}, demonstrating the durability of PDI-DAQ. In addition to its competitive performance, PDI-DAQ operates within a wide potential window of 1.2 V in aqueous electrolyte while remaining insoluble, unlike many supercapacitor materials, giving it a practical edge for energy storage applications. PDI-DAQ presents itself as a structurally robust, insoluble supercapacitor material with strong energy storage performance and the potential for vast applications in the EV industry.

3.3 Materials and Methods

3.3.1 Materials

All chemicals were reagent grade and used without any additional purification. Carbon Black-Ketjenblack EC-300J was purchased from Fuel Cell Stores. 3,4,9,10-perylenetetracarboxylic dianhydride (PTCDA, 95%) was purchased from AK Scientific. 2-aminoanthraquinone (2-AAQ) was purchased from Oakwood Chemical). Zinc acetate dihydrate and Nafion 117 was purchased from Millipore Sigma. All solutions were prepared using Milli-Q Type 1 Ultra-Pure H_2O. Imidazole (99%) and N,N-dimethylformamide (DMF, 99.8%),was purchased from Fisher Chemicals.

3.3.2 Synthesis

PDI-DAQ

In a round bottom flask, PTCDA (500 mg, 1.28 mmol), 2-AAQ (575 mg, 2.58 mmol), zinc acetate anhydride (235 mg, 1.28 mmol), and imidazole (20 g, 294 mmol) were added together and purged under an N_2 atmosphere for 5 minutes. The mixture was then heated and stirred at 110°C for 2 hours, melting the imidazole and allowing the reagents to dissolve in it. The temperature was increased to 160°C and the reaction was allowed to proceed for 48 hours under constant stirring. The material was then cooled to room temperature and removed from the N_2 atmosphere. 130 mL of Millipore Q water was added, and the resultant mixture was vacuum filtered. The remaining solid was then washed 3x with Millipore Q water, 3x with tetrahydrofuran (THF), 3x with 1M NaOH, and 3x with MeOH, to remove the imidazole, zinc acetate, and any unreacted PTCDA and 2-AAQ impurities. The product was then dried in an oven at 60°C for 12 hours. The synthesis was adapted from Hu et al, [27]

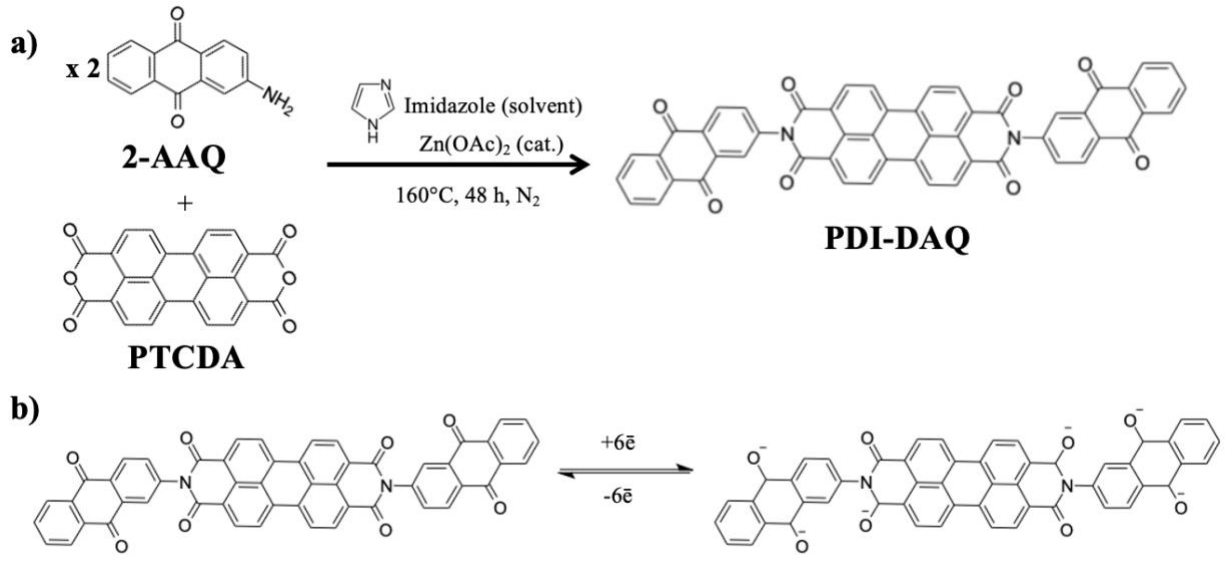

Figure 1 – a) Synthesis overview of PDI-DAQ from PTCDA and 2-AAQ in imidazole solvent with $Zn(OAc)_2$ catalyst. b) Proposed 6-electron transfer mechanism of PDI-DAQ.

3.3.3 Characterization

Fourier transform infrared (FTIR) spectroscopy was conducted on PDI-DAQ with a Thermo Scientific Nicolet 6700 FT-IR. H^1 Nuclear Magnetic Resonance (NMR) spectroscopy was performed on a Bruker 600 Hz. To determine the crystal phase of the samples, x-ray diffraction crystallography was performed with a Cu K_α radiation source (λ=1.5418 Å) operating at 30 kV and 30 mA at the McMaster Analytical Diffraction facility. The data was collected at diffraction angles of 2θ=0-50º. The identification of the phase was based on JCPDS cards, and the primary crystallite size was calculated using the Scherrer equation (**Equation 1**). Scanning electron microscopy (SEM) was performed on an FEI Magellan 400 at 4 kV and 13 pA in high vacuum (10^{-4} Pa regime) to determine PDI-DAQ particle size and morphology, and the uniformity of composition of the PDI-DAQ/CB composite electrode. Samples were drop casted on Si wafers, with secondary detectors used throughout, as well as an Everhart-Thornley detector for low magnification images at a 4 mm working distance. A through lens detector was used in immersion mode for high magnification images at a 2 mm working distance. Energy dispersive X-ray (EDX) spectroscopy was performed on PDI-DAQ at 5 kV, 1.6 nA with an image scan size of 1024 x 1024 pixels, a dwell time of 5 µs/pixel, and a working distance of 4 mm.

3.3.4 Electrochemical Measurements

All cyclic voltammetry (CV), galvanostatic charge discharge (GCD), and cycling stability tests were measured by a BioLogic SAS VSP-300 potentiostat through EC-Lab software. All measurements were set-up through a three-electrode system – a Pine glassy carbon working electrode, a graphite counter electrode, and a Pine Ag/AgCl reference electrode. To fabricate the working electrode, the synthesized PDI-DAQ and conductive carbon black in a 1:1 ratio (2.5 mg

each), and Nafion 117 (150 µL) were dispersed into 5 mL to form an ink. The ink was then sonicated for 30 minutes to uniformly disperse the electrode material. Following sonication, 2.5 µL of the prepared ink was drop-casted onto the glassy carbon electrode to achieve a mass loading of 34 µg cm^{-2}. The electrode was heated in a VWR forced air oven at 80°C for 15 minutes to evaporation DMF solvent and then allowed to return to room temperature, leaving a thin film of active material on the glassy carbon. The electrode was placed in a three-electrode cell with 1 M H_2SO_4 electrolyte, which was purged with N_2 during and 20 minutes before all experiments.

3.3.5 Calculations

Crystallite size was calculated from **Equation 1**:

Equation 1: $$D = \frac{K\lambda}{\beta cos\theta}$$

Where D is the crystallite size, K is the Scherrer constant (0.89), λ is the x-ray wavelength corresponding to Cu K_α radiation (0.15406 nm), θ is the diffraction angle, and β is the line broadening (in radians) at half maximum (FWHM).

Specific capacitance values (C_s, units of Fg^{-1}) from CV data were calculated with **Equation 2**:

Equation 2: $$C_s = \frac{\int IdV}{2 \cdot v \cdot \Delta V \cdot m}$$

Specific capacitance values (C_s, units of Fg^{-1}) from GCD data were calculated with **Equation 3:**

Equation 3: $$C_{s=\frac{I}{(\frac{dV}{dt})m}}$$

In the above equations, I represents the current (A), v is the scan rate (mV s^{-1}), m is the mass of active material (g), t is the time (s) and ΔV is the potential window (V).

3.4 Results and Discussion

3.4.1 Characterization

Fourier Transform Infrared (FT-IR) spectroscopy was used to provide clarification on the structural characteristics of the synthesized PDI-DAQ. As seen in **Figure 2a**, the N-H peak that is identifiable in 2-AAQ at ~3338 cm^{-1} disappears in the PDI-DAQ spectrum, suggesting the N-H bond was broken during the reaction.[27] Furthermore, the fingerprint region shown in **Figure 2a** shows that the vibrations of the C=O group in PTCDA (~1770 cm^{-1}), which are found in the anhydrides at the ends of the molecule, have shifted to a lower wavelength (~1701 cm^{-1}) in PDI-DAQ. This shift is evidence that the anhydride group has been replaced by the imide group, where the two C=O groups are adjacent to a nitrogen atom rather than the oxygen atom present in the structure of PTCDA, causing a change in the chemical environment surrounding the C=O groups.[27] In contrast, there is a minimal wavelength shift between the C=O ketone peak for 2-AAQ (~1671 cm^{-1}) before trimerization compared to afterwards in PDI-DAQ (~1667 cm^{-1}). This is because the chemical environment around the ketone of 2-AAQ is marginally changed, as the imide bond formation was 4 bond lengths from the carbonyl carbon, unlike the carbonyl group present in PTCDA. These FTIR findings are consistent with other studies that have effectively synthesized the molecule.[27]–[29]

^{1}H and was performed on PDI-DAQ to further confirm the synthesized structure. A 9:1 H_2SO_4:D_2SO_4 solvent system was used. The ^{1}H NMR provided more evidence of the formation of PDI-DAQ via imide bond formation of PTCDA with 2 molecules of 2-AAQ (**Figure 2b**) by analysis of the number of protons on the perylene moiety (8 protons) and the 2 anthraquinone moieties (14 protons), giving a ratio of 4:7. The sum of the integrations of multiplet at 7.80-8.08

ppm, corresponding to the protons of the perylene moiety, and the peaks at 6.93-7.51 ppm, correspond to the protons of the anthraquinone moiety, makes an approximate 4:7 ratio. This along with the absence of an N-H peak in the PDI-DAQ FTIR spectra provide strong evidence of the successful synthesis of PDI-DAQ.

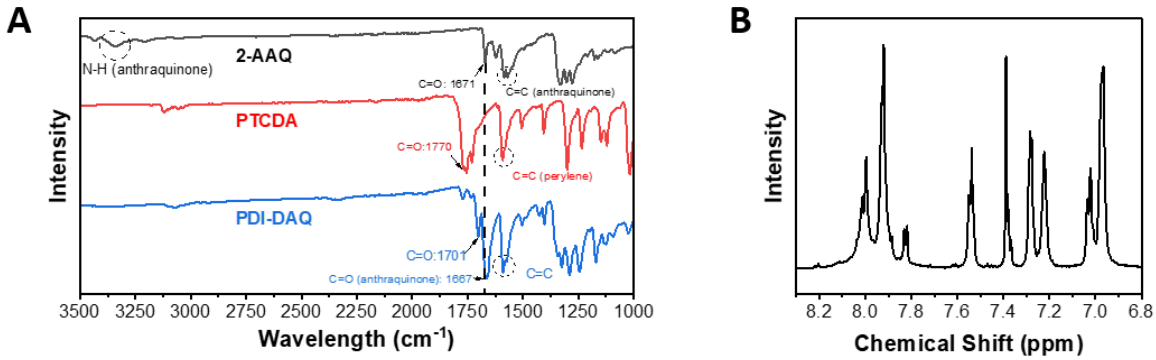

Figure 2 – (a) FTIR Spectra For 2-AAQ, PTCDA, and PDI-DAQ (b) H^1 NMR spectrum confirmed the structure of the as synthesized PDI-DAQ. Chemical shifts: ^{1}H NMR (600 MHz, ppm, D_2SO_4, δ): 7.80-8.08 (m, 4H), 7.51-7.57 (t,d, 1H), 7.35-7.40 (s, 1H), 7.24-7.31 (d, 1H), 7.18-7.24 (s, 1H) 6.93-7.05 (t, 3H).

Figure 3 shows the X-ray diffraction (XRD) spectra of PDI-DAQ, PDI-DAQ/CB, and CB. The PDI-DAQ spectrum show numerous intense peaks, suggesting that PDI-DAQ is a semi-crystalline organic material. The spectrum of CB shows a large broad peak at 22.5° and a small broad peak at 17°. The peak at 22.5° from CB appears to have shifted to a higher angle in the PDI-DAQ/CB composite spectrum, overlapping the 2 peaks seen in the PDI-DAQ spectrum. This peak overlap means that the spaces between the layers of CB have decreased, potentially because the p-p interactions between PDI-DAQ and CB have brought the CB layers closer together.[34] The crystallite size of PDI-DAQ was calculated to be 11.39 nm using **Equation 1**.

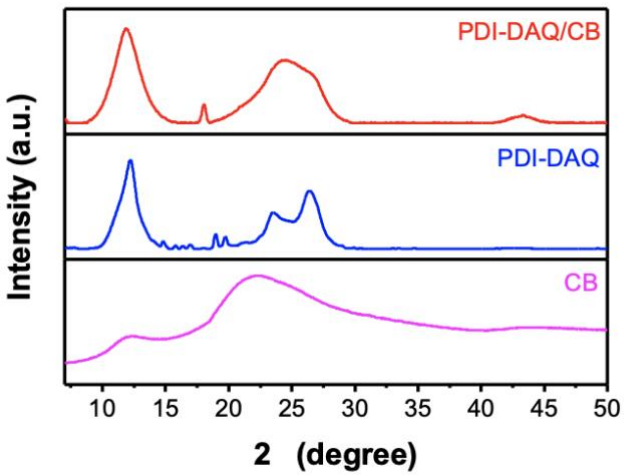

Figure 3: XRD spectra for 50:50 PDI-DAQ:CB composite, PDI-DAQ, and CB.

The morphology of PDI-DAQ and PDI-DAQ/CB were examined by SEM as shown in **Figures 4a,** and **5**, respectively. **Figure 4a** shows the long, thin, sheet-like morphology of PDI-DAQ which provides accessible surface area to help anchor PDI-DAQ to the CB surface during OME preparation through adsorption via p-p interactions.[18] Moreover, the elemental composition of PDI-DAQ was analyzed via EDX spectroscopy. The elemental maps of carbon, oxygen, and nitrogen, as well as the EDX spectrum are shown in **Figure 4b-e**. The intensity of the peaks qualitatively corroborates the elemental composition of PDI-DAQ, where the most prevalent element is C, followed by O and N.

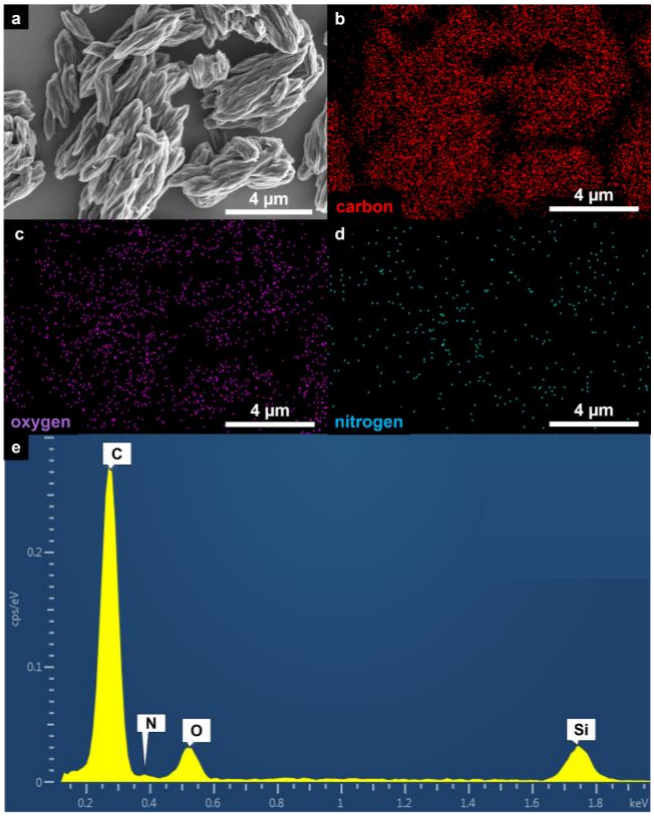

Figure 4: SEM-EDX of PDI-DAQ. (a) An SEM image of PDI-DAQ; (b) carbon map; (c) oxygen map; (d) nitrogen map; (e) EDX spectrum showing C, N, and O peaks from PDI-DAQ, and Si peak from the Si wafer used as the substrate for electron microscopy.

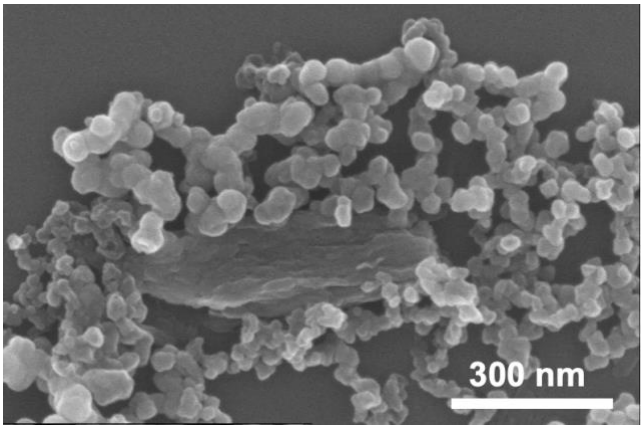

Figure 5: SEM image of 1:1 ratio of PDI-DAQ/CB OME composite

The morphology of PDI-DAQ/CB OME composite is shown in **Figure 5**. The imaged revealed long PDI-DAQ islands, 600 nm in length, surrounded by a network of CB. The PDI-DAQ particles mixed with CB as individual sheets rather than in large aggregates. Performing Brunauer-Emmett-

Teller (BET) analysis on PDI-DAQ revealed its specific surface area to be 154.10 m^2 g^{-1} in its pristine form (**Figure S3**), compared to conventional PANI, which has a reported surface area of 20.02 m^2 g^{-1}.[35] Materials exhibiting high surface areas have good adsorption capabilities compared to those exhibiting low ones.

3.4.2 PTCDA and 2-AAQ Monomers

The electrochemical performance of the individual monomer precursors of PDI-DAQ were examined as outlined above. PTCDA and 2-AAQ both demonstrated pseudocapacitive behaviour attributed to their redox capabilities which were observed as oxidation and reduction peaks (**Figure 6a,b**). PTCDA achieved a capacitance up to 149.8 F g^{-1}, while 2-AAQ achieved 124.2 F g^{-1} at 5 mV s^{-1}.

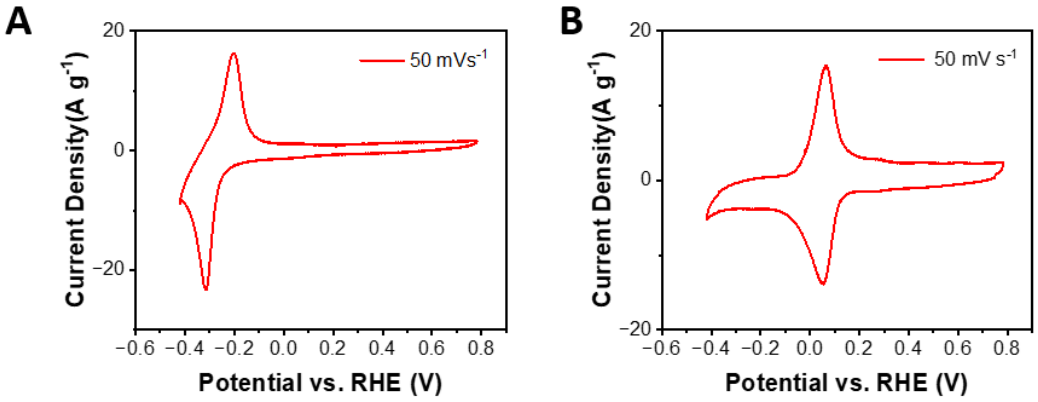

Figure 6: CV curves of (a) PTCDA and (b) 2-AAQ at 100, 50, and 5 mV s^{-1}.

3.4.3 PDI-DAQ Performance

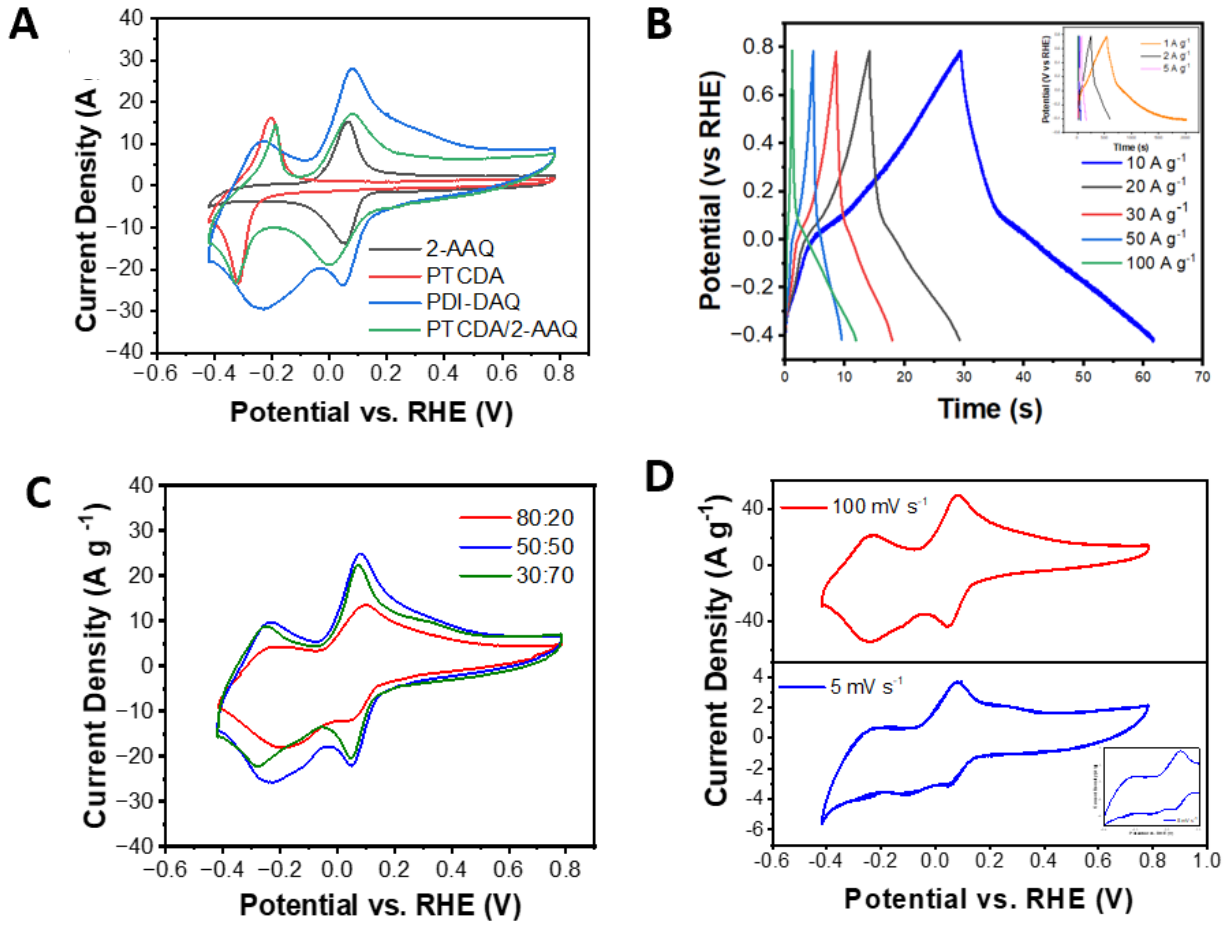

Figure 7: a) Electrochemical performance of PDI-DAQ molecule electrode, comparing with PTCDA, 2-AAQ, and PTCDA/2-AAQ physical mix at 50 mV s^{-1}. b) Different ratios of PDI-DAQ to CB to identify the optimal composition for maximum capacitance. c) Electrochemical performance of PDI-DAQ with CB at a 1:1 ratio at 1, 2, 5, 10, 20, 30, 50, and 100 A g^{-1}. d) CV curves of PDI-DAQ at 100 mV s^{-1} and 5 mV s^{-1}.

Figure 7a illustrates the difference in size of the area under the CV curves of PDI-DAQ and a 1:2 physical mixture of PTCDA and 2-AAQ, indicating a difference in capacitance, (the numerator of **Equation 2** represents the area under the CV curve). PDI-DAQ exhibited a specific capacitance of 215.3 F g^{-1} at 50 mVs^{-1}, while the physically mixed monomers only exhibited 140.0 F g^{-1} at 50 mVs^{-1}. This 53.8% increase in capacitance of PDI-DAQ demonstrates the improved electrochemical energy storage capabilities resulting from covalently bonding PTCDA with 2-AAQ via imide linkages. Specifically, allowing for retention of the conjugated structures between

the moieties of PDI-DAQ compared to the monomeric units interacting via noncovalent intermolecular interactions.[28] The retention of the conjugated structure reduces the mobility of the redox-active centers and stabilizes the intermediate redox states, while also allowing for more efficient charge transfer due to the conjugated p network of the material as well as the proximity of the redox active centers to each other.[36] **Figure 7b** shows the charge and discharge rates of the PDI-DAQ/CB OME via GCD at current densities from 1 A g^{-1} to 100 A g^{-1}. Both the charge and discharge curves show a non-constant slope due to the presence of Faradaic charge storage processes from PDI-DAQ in the OME composite. At 5 A g^{-1}, the PDI-DAQ OME achieved a capacitance of 375 F g^{-1}.

The redox peaks associated with the perylene moiety (-0.21V/-0.24V vs RHE) have a noticeably smaller peak-to-peak separation (DE_p= 30 mV) compared to its monomeric unit, PTCDA (DE_p= 120 mV) (**Figure 6a**). This 90 mV difference suggests that the barrier of electron transfer for the reversible reactions from carbonyl groups of the perylene moiety is greatly reduced compared to PTCDA.[37] This difference is due to the difference in electronegativity between the oxygen in PTCDA, and the nitrogen that replaces it in PDI-DAQ to form the imide bond.[38] Oxygen has a higher electronegativity (3.5) than nitrogen (3.0) on the Pauling scale, suggesting a stronger ability to attract shared electrons.[38] During the reduction of the adjacent carbonyl groups, the electrons of the carbonyl double bond initiate a nucleophilic attack on available protons, destabilizing the carbonyl carbon by reducing its electron density (more electropositive).[38] In PDI-DAQ, the adjacent nitrogen is less electronegative than the adjacent oxygen in PTCDA, meaning the nitrogen from the 2-AAQ amino group is more electron-donating and capable of stabilizing the electropositive carbonyl carbon in the transition state during reduction.[39]–[41] The replacement of an oxygen with a nitrogen is believed to lower the HOMO/LUMO band gap for electron transfer,

consequently lowering the energy barrier for reduction and resulting in an increased electron transfer speed.[40] On the contrary, the redox peaks associated with the anthraquinone moiety, 0.08V/0.05V vs RHE, retains approximately the same peak-to-peak separation (DE_p= 30 mV) as its monomeric unit, 2-AAQ (DE_p= 20 mV). As the anthraquinone carbonyl groups are further in intramolecular proximity to the imide bond than the perylene carbonyl groups, the effects the imide nitrogen has on its energy barrier are minimal. Consequently, there is only a 10 mV difference in electron transfer kinetics observed from the similar peak-to-peak separation.

While at 100 mV s^{-1} there are two well-defined pairs of redox peaks at, -0.21V/-0.24V and 0.08V/0.05V vs RHE, at 5 mV s^{-1} there is observable shouldering occurring due to another ill-defined redox peak pair in between (**Figure 7d**). This behaviour noticed only following trimerization, and at lower scan rates, likely resulting in some of the reversible electron transfers of PDI-DAQ being less favourable and occurring more predominantly when the scan rate is sufficiently low for them to reach chemical equilibria.[37] At high scan rates, equilibrium does not have sufficient time to be reached, merging the peaks together.[42] This, however, can explain why compared to the physically mixed PTCDA and 2-AAQ, PDI-DAQ exhibits broader peaks. Since the redox-active sites of the perylene and anthraquinone moieties are covalently bonded, it is hypothesized that once the former redox-active sites are forming a transition state with available protons during reduction/oxidation, it can change the stability of subsequent redox-active sites, mildly shifting their redox potentials.[43]

PDI-DAQ mixed with CB in weight fractions ranging from 30% to 80% PDI-DAQ were tested to identify the optimal ratio that would give the highest capacitance at a given scan rate (**Figure 7c)**. The optimal ratio of PDI-DAQ with CB to produce an OME with the maximum capacitance was determined to be 1:1 (50 wt.% of each). Similarly, Jiao *et al.*, reported that a 1:1 ratio of rGO and

a polymer of PTCDA with 2,6-diaminoanthraquine was the optimal composition to fabricate their organic molecule electrode for supercapacitor applications.[34] As the charge transfer resistance of the PDI-DAQ OME was determined to be 21.6 Ω, while for PDI-DAQ/CB it was only 9.5 Ω (**Figure 9c**), it is hypothesized that due to its insufficient electrical conductivity, a higher PDI-DAQ ratio does not leave sufficient carbon black content to form a complete conductive network to connect the redox-active sites of PDI-DAQ.[36] The addition of CB lowers the charge transfer resistance of the PDI-DAQ electrode, allowing for more efficient electron transfer throughout the composite material to maximize the capacitances.

3.4.4 PDI-DAQ Cycling Stability

The cycling stability of PDI-DAQ was tested through 10,000 CV cycles at 100 mV/s (**Figures 8a-b**). After 5000 cycles, the material's capacitance retention was 68.4% from its initial value, and decreased another 7.2% in the following 5000 cycles, to 61.2%. To ensure PDI-DAQ was not dissolving into the 1 M H_2SO_4 electrolyte, a stability test in 0.1 M H_2SO_4 was performed which resulted in a capacitance retention of 68.3%.

In **Figure 8c**, there is an observed increase in capacitance over the first 500 cycles, followed by a very similar trend in decreasing capacitance retention as in 1 M H_2SO_4. The absence of this initial capacitance increase in 1 M H_2SO_4 may be because over the course of charging and discharging of the electrode, the electrode materials may loosen up and increase in volume, increasing its porosity and surface area.[44] This structural modification during cycling can allow for more protons to penetrate the electrode over time, improving the capacitance because of better charge transport. The lesser availability of protons in 0.1 M H_2SO_4 can make the penetration into the electrode material take many cycles, while the proton availability in 1 M H_2SO_4 is abundant and happens within the first few cycles.

If instead the capacitance retention was calculated after the maximum capacitance reached at 500 cycles until 10,000 cycles, it is 60.8 % (after 9500 cycles). ^{1}H NMR on the electrolyte (concentrated by water evaporation at 60°C) after stability testing showed no evidence of aromatic peaks relating to PDI-DAQ or its monomeric fragments. This provides evidence that dissolution due to solubilization in the electrolyte is unlikely to be the cause for capacitance fading. Another factor to consider may be the carbon black itself degrading during cycling, as it is known to be susceptible to aggregation of particles and low electrical conductivity because of its impurities, leading to capacitance loss.[45] However, from the CV curves of **Figure 8a** over the course of 10,000 cycles, the redox peaks appear to lose intensity, while the EDLC component closer to 0.8 V vs RHE retain the majority of their size and shape. The loss of the redox peak intensities over the course of cycling suggests the redox-active properties of PDI-DAQ are what are predominantly degrading as opposed to those of the CB.

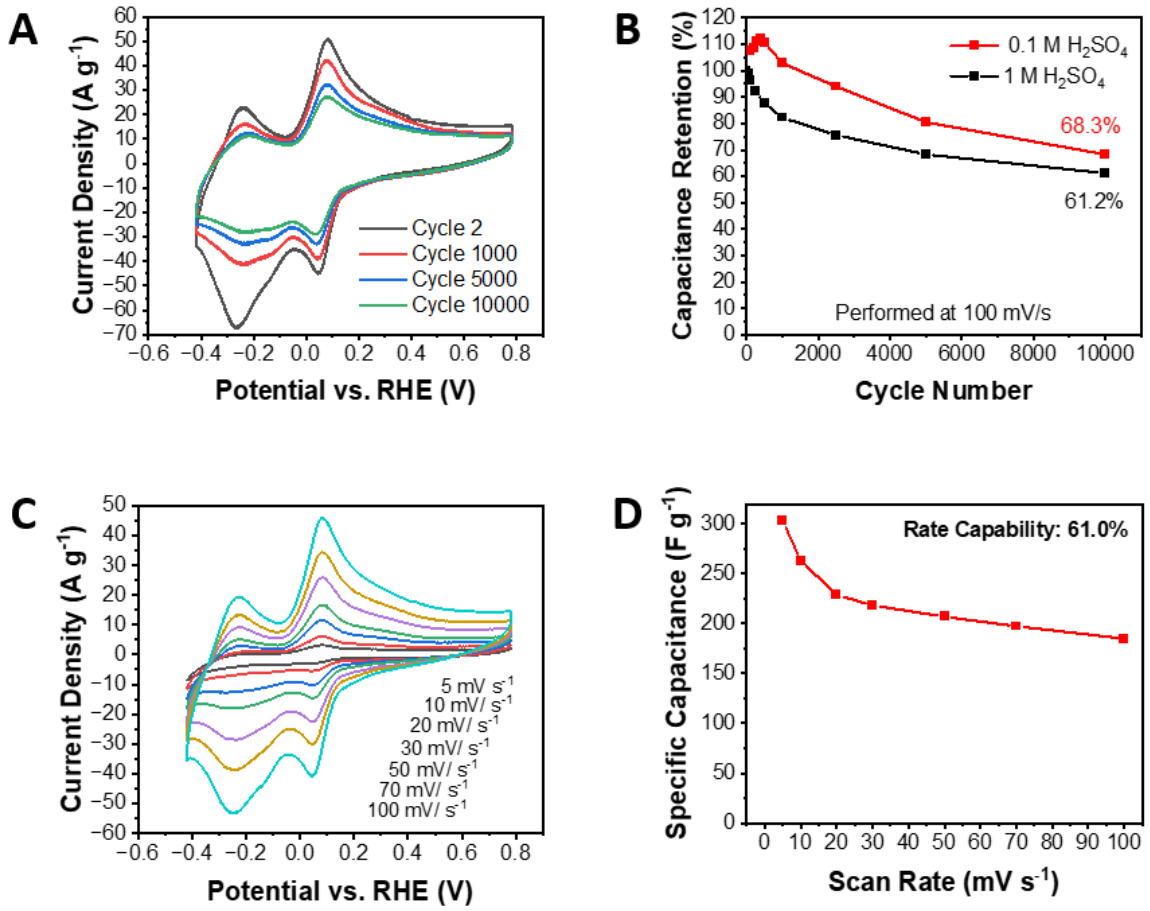

Figure 8 – (a) 10,000 cycle stability test CV curves of PDI-DAQ at 100 mV s^{-1} in 1 M H_2SO_4; (b) Capacitance retention of PDI-DAQ 100 mV s^{-1} in 1 M H_2SO_4 and 0.1 M H_2SO_4; (c) Rate capability CV curves of PDI-DAQ from 5-100 mV s^{-1}; (d) Rate capability of PDI-DAQ.

3.4.5 PDI-DAQ Rate Capability

Testing the rate capability of PDI-DAQ was used to determine application specific metrics such as power delivery and storage capabilities.[46], [47] CVs were run on the PDI-DAQ OME at scan rates of 5, 10, 20, 30, 50, 70, and 100 mV s^{-1} (**Figure 8d**). At 5 mV s^{-1}, the electrode exhibited a capacitance of 303.16 F g^{-1}; at 100 mVs^{-1}, it achieved a capacitance of 185.00 F g^{-1}. This means that the rate capability (relative to 5 mV s^{-1}) is 61.0%.

The capacitive and diffusion-controlled contributions were quantified using Dunn's method from **Equation 4**, where k_1 and k_2 are constants, v is the scan rate, and i is current. k_1v represents the capacitive-controlled contribution, and $k_2v^{1/2}$ represents the diffusion-controlled contribution.[48]

Equation 4: $$i(v) = k_1 v + k_2 v^{1/2}$$

At 5 mV s^{-1}, the diffusion-controlled contribution is predominant at about 53%, whereas as the scan rate increases to 100 mV s^{-1}, it becomes only 18% as the process becomes increasingly capacitive-controlled, illustrating the diffusive nature of this supercapacitor material (**Figure 9b**). The diffusive contribution decreases with increasing scan rate because the electrolyte protons do not have enough time to fully interact with PDI-DAQ compared to its contribution at low scan rates which allows for more redox activity to occur.[49] These results indicate that non-Faradaic charge transport processes are more predominant at higher scan rates, while Faradaic processes contribute greatly to the capacitance at lower scan rates.[48] This analysis helps understand the relative contributions and dependence of EDLC and pseudocapacitance to the material's overall charge storage.

Electrochemical Impedance Spectroscopy (EIS) was performed at open circuit potential to explore the ion transport characteristics. The Nyquist diagrams for both PDI-DAQ and PDI-DAQ/CB electrodes are illustrated in **Figure 9c** depicting a semi-circular pattern in the high-frequency range alongside a sloping line within the low-frequency domain. The depicted equivalent circuits in the inset of **Figure 9c** were employed to accurately model the observed Nyquist diagrams. The circuits for both PDI-DAQ and PDI-DAQ/CB consist of a resistor representing the electrolyte solution resistance, paired with two capacitors reflecting the electrical double-layer current (C2) and the Faradaic current (C3). Additionally, a resistor accounts for the charge transfer resistance. The

circuit further incorporates a Warburg element, which accounts for the deviation from a perfect vertical alignment in the low-frequency area, suggesting a marginally extended Warburg length.[50] The deduced charge transfer resistances were found to be 21.6 Ω for the PDI-DAQ and 9.5 Ω for the PDI-DAQ/ CB electrodes. The reduced charge transfer resistance observed in the PDI-DAQ/CB electrode may be ascribed to the π-π interactions between the CB and PDI-DAQ, which are likely to enhance the electrode's conductivity.[51] The conductivity enhancement of the redox-active material by addition of CB is a contributor to the high capacitances observed of the 1:1 PDI-DAQ/CB composite electrode in a three-electrode setup, as the PDI-DAQ is more electrochemically available due to a reduction in charge transfer resistance. The equivalent series resistance (ESR) can be estimated by the X-intercept of the Nyquist plot. The ESR of the pure PDI-DAQ electrode material is much higher than that of the PDI-DAQ/CB composite electrode due to the higher resistivity of PDI-DAQ in comparison to CB, thus further demonstrating how the addition of CB improves the electrode's conductivity. From examining the low frequency region of the PDI-DAQ/CB Nyquist plot, the curve is very straight and has a very steep slope, almost at 90° to the X-axis, suggesting the rate of diffusion is fast and the electrode exhibits a good capacitance performance.[50] This is unlike pure PDI-DAQ, which has a curved line indicative of a higher Warburg resistance.

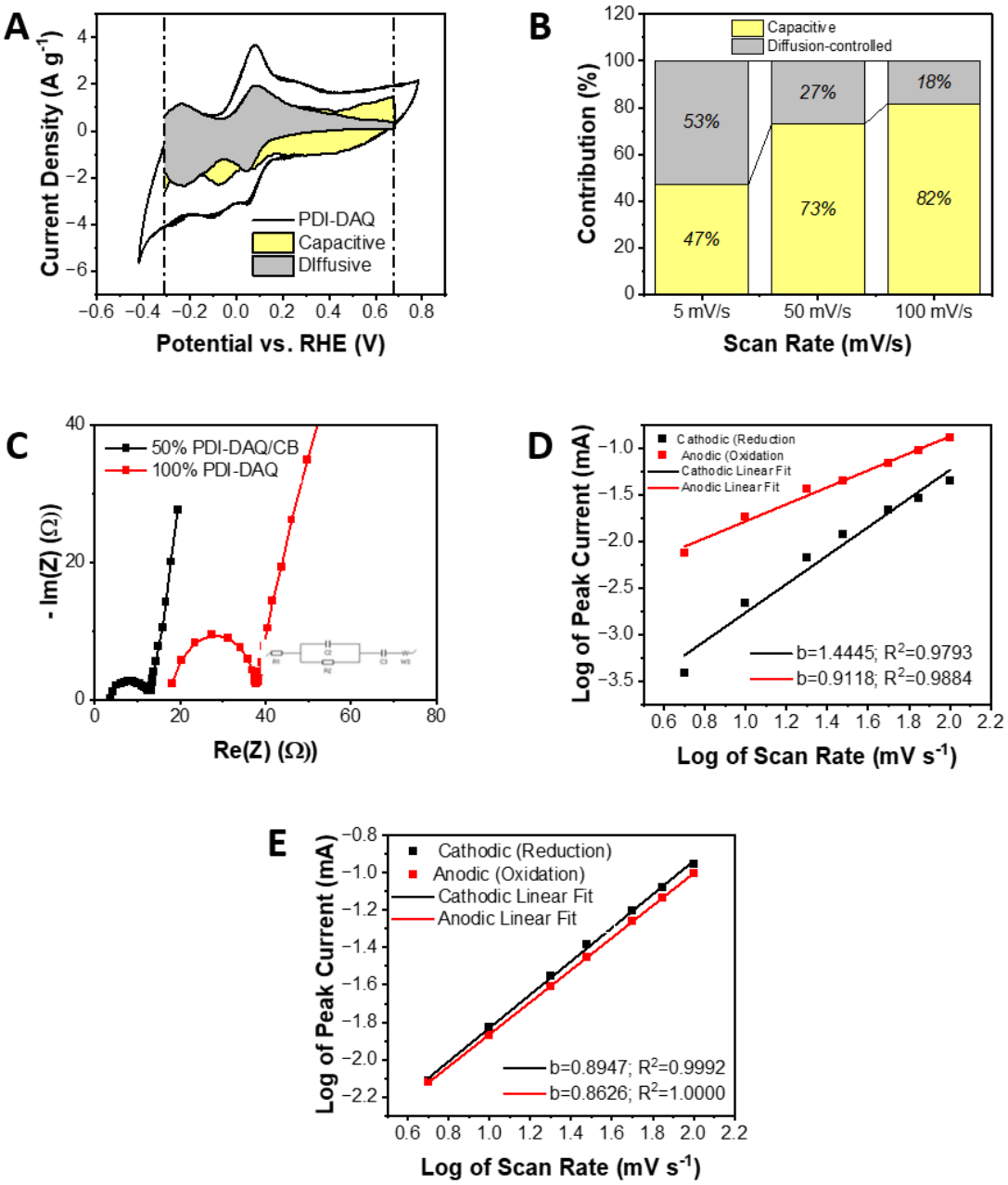

Figure 9 – (a) Capacitive and diffusion-controlled contributions of PDI-DAQ at 5 mV s^{-1}. (b) Capacitive and diffusion-controlled contributions at 5 mV s^{-1}, 50 mV s^{-1}, and 100 mV s^{-1}. (c) Nyquist plot of PDI-DAQ/CB. (d) Power law of peak 1 PDI-DAQ/CB. (e) Power Law of peak 2 of PDI-DAQ/CB

3.5 Conclusion

This work describes the facile synthesis of a redox-active trimer, PDI-DAQ, which was successfully incorporated with a low-cost CB substrate. This was accomplished alongside a simple OME preparation procedure to fabricate a high-performance supercapacitor OME with improved cycling stability and capacitance compared to its monomeric counterparts, PTCDA and 2-AAQ. Using a potential range of 1.2 V, a capacitance of 318.6 F g^{-1} was achieved at 5 mV s^{-1} with a cycling stability of 61.2 % following 10,000 reduction/oxidation cycles in acidic media. Furthermore, this performance was achieved through an optimization of the ratio of PDI-DAQ to CB to 1:1 by weight.

The simple and scalable synthesis of PDI-DAQ combined with high capacitance using a cheap conductive carbon substrate demonstrates the potential of this composite material to be applied in the energy storage field, such as in EVs. PDI-DAQ exhibits exceptional capacitances even at high scan rates and current densities with a very low-cost carbon substrate through a simple electrode preparation process that requires no carbon treatment steps.

3.6 Supplementary Figures

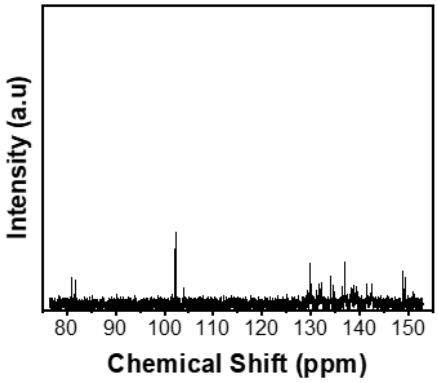

Figure S1: ^{13}C NMR spectrum of PDI-DAQ

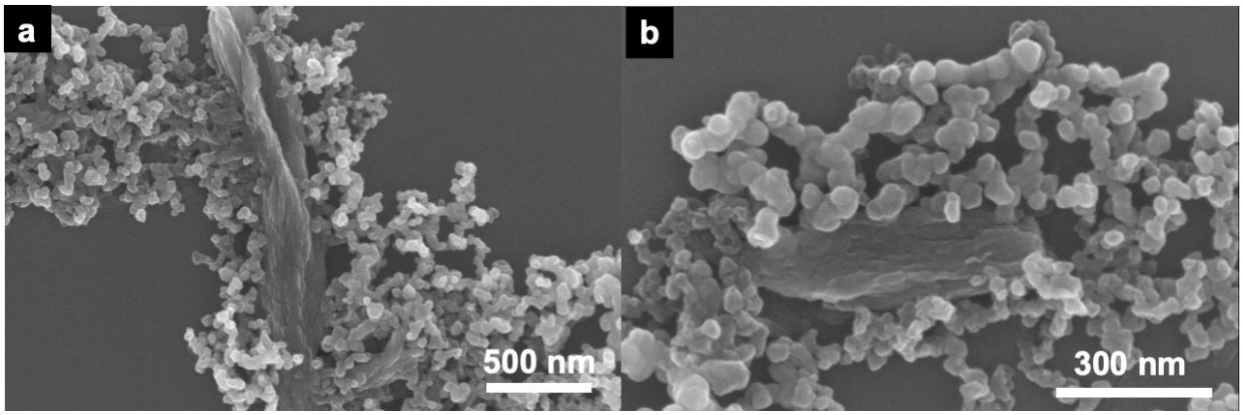

Figure S2: SEM images of 1:1 ratio of PDI-DAQ/CB OME at (a) 250,000x and (b) 350,000x magnifications

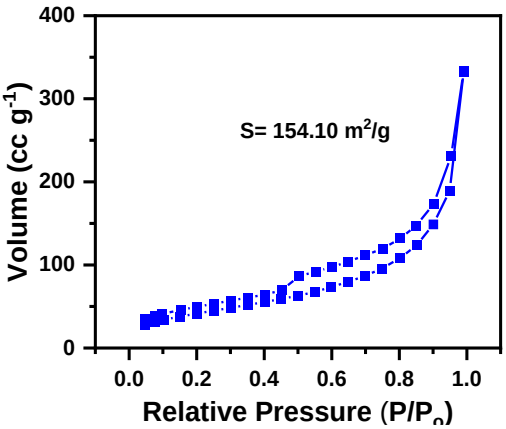

Figure S3: BET N_2 adsorption-desorption isotherm of PDI-DAQ.

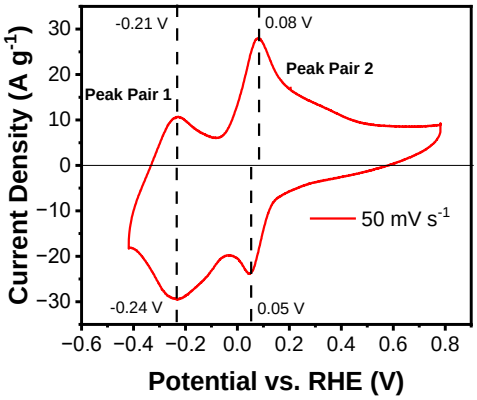

Figure S4: PDI-DAQ/CB electrode peak pairs and peak potentials at 50 mV s^{-1}.

3.7 References

[1] "CO2 Emissions in 2022," *International Energy Agency*, 2022. [Online]. Available: https://www.iea.org/reports/co2-emissions-in-2022.

[2] D. Lemian and F. Bode, "Battery-Supercapacitor Energy Storage Systems for Electrical Vehicles: A Review," *Energies*, vol. 15, no. 15, 2022.

[3] "Links between fuel consumption, climate change, our environment and health," *Natural Resources Canada*, 2016. [Online]. Available: https://www.google.com/url?sa=t&source=web&rct=j&opi=89978449&url=https://natural-resources.canada.ca/energy/efficiency/communities-infrastructure/transportation/idling/4419%23:~:text%3DThis%2520suggests%2520that%2520GHG%2520emissions,our%2520air%2520qual.

[4] "Emissions from electric vehicles," *U.S Department of Energy*, 2021. [Online]. Available: https://www.google.ca/url?sa=t&source=web&rct=j&opi=89978449&url=https://afdc.energy.gov/vehicles/electric_emissions.html&ved=2ahUKEwiMuLm4w6aFAxWUMjQIHU28APIQFnoECA4QAQ&usg=AOvVaw0N9neVabd7m4fjJumOJnSA.

[5] F. Un-Noor, S. Padmanaban, L. Mihet-Popa, M. N. Mollah, and E. Hossain, "A comprehensive study of key electric vehicle (EV) components, technologies, challenges, impacts, and future direction of development," *Energies*, vol. 10, no. 8, 2017.

[6] M. J. Lain and E. Kendrick, "Understanding the limitations of lithium ion batteries at high rates," *J. Power Sources*, vol. 493, p. 229690, 2021.

[7] M. E. Şahin, F. Blaabjerg, and A. Sangwongwanich, "A Comprehensive Review on Supercapacitor Applications and Developments," *Energies*, vol. 15, no. 3, pp. 1–26, 2022.

[8] N. M. Jamadar and H. T. Jadhav, "Effectiveness of supercapacitor during braking

operation of electric vehicle," *Mater. Today Proc.*, vol. 56, pp. 314–319, 2022.

[9] S. P. S. Badwal, S. S. Giddey, C. Munnings, A. I. Bhatt, and A. F. Hollenkamp, "Emerging electrochemical energy conversion and storage technologies," *Front. Chem.*, vol. 2, no. SEP, pp. 1–28, 2014.

[10] Y. Shao *et al.*, "Design and Mechanisms of Asymmetric Supercapacitors," *Chem. Rev.*, vol. 118, no. 18, pp. 9233–9280, 2018.

[11] C. Choi *et al.*, "Achieving high energy density and high power density with pseudocapacitive materials," *Nat. Rev. Mater.*, vol. 5, no. 1, pp. 5–19, 2020.

[12] S. Fleischmann *et al.*, "Pseudocapacitance: From Fundamental Understanding to High Power Energy Storage Materials," *Chem. Rev.*, vol. 120, no. 14, pp. 6738–6782, 2020.

[13] Y. He, Q. Wei, N. An, C. Meng, and Z. Hu, "Organic Small-Molecule Electrodes: Emerging Organic Composite Materials in Supercapacitors for Efficient Energy Storage," *Molecules*, vol. 27, no. 22, 2022.

[14] M. A. A. Mohd Abdah, N. H. N. Azman, S. Kulandaivalu, and Y. Sulaiman, "Review of the use of transition-metal-oxide and conducting polymer-based fibres for high-performance supercapacitors," *Mater. Des.*, vol. 186, p. 108199, 2020.

[15] E. Dhandapani, S. Thangarasu, S. Ramesh, K. Ramesh, R. Vasudevan, and N. Duraisamy, "Recent development and prospective of carbonaceous material, conducting polymer and their composite electrode materials for supercapacitor — A review," *J. Energy Storage*, vol. 52, no. PC, p. 104937, 2022.

[16] Q. Li, M. Horn, Y. Wang, J. Macleod, N. Motta, and J. Liu, "A Review of Supercapacitors Based on Graphene and Redox-Active Organic Materials," 2019.

[17] Y. Ding, D. Chen, X. Ren, Y. Cao, and F. Xu, "Organic-conjugated

polyanthraquinonylimide cathodes for rechargeable magnesium batteries," *J. Mater. Chem. A*, vol. 10, no. 26, pp. 14111–14120, 2022.

[18] S. P. Ega and P. Srinivasan, "Quinone materials for supercapacitor: Current status, approaches, and future directions," *J. Energy Storage*, vol. 47, no. September 2021, p. 103700, 2022.

[19] L. Zhao *et al.*, "Significantly stable organic cathode for lithium-ion battery based on nanoconfined poly(anthraquinonyl sulfide)@MOF-derived microporous carbon," *Electrochim. Acta*, vol. 335, 2020.

[20] M. R. Biradar, A. M. Kale, B. C. Kim, S. V. Bhosale, and S. V. Bhosale, "Perylenediimide/Graphite Foil-Based Electrode Materials with Outstanding Cycling Stability for Symmetric Supercapacitor Device Architectures," *Energy Technol.*, vol. 10, no. 6, pp. 1–10, 2022.

[21] M. R. Biradar, A. V. Salkar, P. P. Morajkar, S. V. Bhosale, and S. V. Bhosale, "Pyrazine-based organic electrode material for high-performance supercapacitor applications," *J. Energy Storage*, vol. 48, no. January, p. 103953, 2022.

[22] L. M. Zhu *et al.*, "Enhancing electrochemical performances of small quinone toward lithium and sodium energy storage," *Rare Met.*, vol. 41, no. 2, pp. 425–437, 2022.

[23] F. Ma *et al.*, "Organic Molecular Electrode with Ultrahigh Rate Capability for Supercapacitors," 2020.

[24] T. Cai *et al.*, "Stable cycling of small molecular organic electrode materials enabled by high concentration electrolytes," *Energy Storage Mater.*, vol. 31, no. July, pp. 318–327, 2020.

[25] S. Biswas, N. Shauloff, R. Bisht, and R. Jelinek, "Anthraquinone-Functionalized

Polydiacetylene Supercapacitors," *Adv. Sustain. Syst.*, vol. 7, no. 6, pp. 1–9, 2023.

[26] Y. Zhao *et al.*, "A π-Conjugated Polyimide-Based High-Performance Aqueous Potassium-Ion Asymmetric Supercapacitor," *Macromol. Rapid Commun.*, vol. 43, no. 15, pp. 1–8, 2022.

[27] Y. Hu *et al.*, "Novel Insoluble Organic Cathodes for Advanced Organic K-Ion Batteries," *Adv. Funct. Mater.*, vol. 30, no. 17, pp. 1–10, 2020.

[28] X. Wang *et al.*, "Insoluble small-molecule organic cathodes for highly efficient pure-organic Li-ion batteries," *Green Chem.*, vol. 23, no. 16, pp. 6090–6100, 2021.

[29] Y. Hu *et al.*, "Ultra-Stable, Ultra-Long-Lifespan and Ultra-High-Rate Na-ion Batteries Using Small-Molecule Organic Cathodes," *Energy Storage Mater.*, vol. 41, no. July, pp. 738–747, 2021.

[30] C. Zhang, L. Ren, X. Wang, and T. Liu, "Graphene oxide-assisted dispersion of pristine multiwalled carbon nanotubes in aqueous media," *J. Phys. Chem. C*, vol. 114, no. 26, pp. 11435–11440, 2010.

[31] L. L. Zhang, R. Zhou, and X. S. Zhao, "Graphene-based materials as supercapacitor electrodes," *J. Mater. Chem.*, vol. 20, no. 29, pp. 5983–5992, 2010.

[32] "Graphene Oxide Power." [Online]. Available: https://www.graphenea.com/products/graphene-oxide-powder.

[33] "Carbon Black - Ketjenblack EG-300J." .

[34] L. Jiao *et al.*, "A novel organic molecule electrode based on organic polymer functionalized graphene for supercapacitor with high-performance," *J. Energy Storage*, vol. 52, no. PA, p. 104777, 2022.

[35] M. Ayad and S. Zaghlol, "Nanostructured crosslinked polyaniline with high surface area:

Synthesis, characterization and adsorption for organic dye," *Chem. Eng. J.*, vol. 204–205, pp. 79–86, 2012.

[36] T. Le Gall, K. H. Reiman, M. C. Grossel, and J. R. Owen, "Poly(2,5-dihydroxy-1,4-benzoquinone-3,6-methylene): A new organic polymer as positive electrode material for rechargeable lithium batteries," *J. Power Sources*, vol. 119–121, pp. 316–320, 2003.

[37] N. Elgrishi, K. J. Rountree, B. D. McCarthy, E. S. Rountree, T. T. Eisenhart, and J. L. Dempsey, "A Practical Beginner's Guide to Cyclic Voltammetry," *J. Chem. Educ.*, vol. 95, no. 2, pp. 197–206, 2018.

[38] P. Politzer, J. E. Huheey, J. S. Murray, and M. Grodzicki, "Electronegativity and the concept of charge capacity," *J. Mol. Struct. THEOCHEM*, vol. 259, no. C, pp. 99–120, 1992.

[39] A. S. Lukas, Y. Zhao, S. E. Miller, and M. R. Wasielewski, "Biomimetic electron transfer using low energy excited states: A green perylene-based analogue of chlorophyll a," *J. Phys. Chem. B*, vol. 106, no. 6, pp. 1299–1306, 2002.

[40] S. Vajiravelu, L. Ramunas, G. Juozas Vidas, G. Valentas, J. Vygintas, and S. Valiyaveettil, "Effect of substituents on the electron transport properties of bay substituted perylene diimide derivatives," *J. Mater. Chem.*, vol. 19, no. 24, pp. 4268–4275, 2009.

[41] P. E. Hartnett *et al.*, "Influence of anion delocalization on electron transfer in a covalent porphyrin donor-perylenediimide dimer acceptor system," *J. Am. Chem. Soc.*, vol. 139, no. 2, pp. 749–756, 2017.

[42] F. Marken, A. Neudeck, and A. M. Bond, "Cyclic Voltammetry," in *Electroanalytical Methods*, Springer, Berlin, Heidelberg, 2010, pp. 57–106.

[43] T. Nakayama, N. Okumura, and B. Uno, "Complementary Effect of Intra- And

Intermolecular Hydrogen Bonds on Electron Transfer in β-Hydroxy-Anthraquinone Derivatives," *J. Phys. Chem. B*, vol. 124, no. 5, pp. 848–860, 2020.

[44] S. Yang *et al.*, "Electrode structural changes and their effects on capacitance performance during preparation and charge-discharge processes," *J. Energy Storage*, vol. 24, no. March, p. 100799, 2019.

[45] E. Pameté *et al.*, "The Many Deaths of Supercapacitors: Degradation, Aging, and Performance Fading," *Adv. Energy Mater.*, vol. 13, no. 29, 2023.

[46] A. Eftekhari, "The mechanism of ultrafast supercapacitors," *J. Mater. Chem. A*, vol. 6, no. 7, pp. 2866–2876, 2018.

[47] D. Zhang, X. Zhang, Y. Chen, P. Yu, C. Wang, and Y. Ma, "Enhanced capacitance and rate capability of graphene/polypyrrole composite as electrode material for supercapacitors," *J. Power Sources*, vol. 196, no. 14, pp. 5990–5996, 2011.

[48] M. Z. Iqbal *et al.*, "Capacitive and diffusion-controlled mechanism of strontium oxide based symmetric and asymmetric devices," *J. Energy Storage*, vol. 27, no. October 2019, p. 101056, 2020.

[49] U. Aziz, M. Z. Iqbal, S. Aftab, S. M. Wabaidur, and M. J. Iqbal, "Exploring the Redox Activity of a Transition-Metal-Intercalated 1,3,5-Benzenetricarboxylic Acid Organic-Inorganic Network for Potential Battery-Supercapacitor Applications," *Energy and Fuels*, vol. 37, no. 8, pp. 6248–6256, 2023.

[50] L. Hou, C. Kong, Z. Hu, Y. Han, and B. Wu, "Redox active organic molecule-Emodin modified graphene for high-performance supercapacitors," *J. Electroanal. Chem.*, vol. 895, no. 145, p. 115402, 2021.

[51] L. Xu *et al.*, "Fused Heterocyclic Molecule-Functionalized N-Doped Reduced Graphene

Oxide by Non-Covalent Bonds for High-Performance Supercapacitors," *ACS Appl. Mater. Interfaces*, vol. 12, no. 40, pp. 45202–45213, 2020.

CHAPTER 4

4. PPA

The following paper describes the polymeric material, PPA, as a supercapacitor material. This work on PPA provides insight into the electrochemical energy storage capabilities of PPA by novel application with a low-cost carbon material. Furthermore, the information from this paper on PPA can be compared with that of the trimeric analogue, PDI-DAQ, in Chapter 3. Details of the implications of this work are described in Chapter 1.

A Polymer Electrode Material with Low-Cost Carbon Black for Supercapacitor Applications

Arjun Rego, Navid Noor, Storm Gourley, Amirhossein Foroozan , Shayan Angizi, Drew Higgins*

Department of Chemical Engineering, McMaster University, 1280 Main Street West, Hamilton, Ontario, L8S 4L7, Canada.

4.1 Abstract

The adoption of electric vehicles (EVs) has become a leading solution to mitigate transportation sector greenhouse gas (GHG) emissions, however, challenges remain such as high material costs, limited vehicle range and long-term battery life persist. Supercapacitors are emerging to operate within EV power systems for their faster charge and discharge rates and longevity. Quinone-containing polymeric materials are being investigated as electrode materials for high energy density supercapacitors. In this work, a redox-active polyimide, poly-perylene-3,4,9,10-tetracarboxydiimide-anthraquinone (PPA) was synthesized and prepared as an electrode material incorporated with a low-cost, high surface area conductive carbon black (CB) through a facile preparation process. The PPA electrode exhibited capacitances of up to 377 F g^{-1} at 5 mV s^{-1} and a cycling stability up to 65% after 10,000 cycles at 100 mV s^{-1}. A modified electrode material

synthesis approach incorporated CB during PPA synthesis, which increased the interfacial reactivity between PPA and CB π–π interactions of CB with PPA, improving the cycling stability. The work presented offers the ability for a scalable and low cost PPA electrode material that highlights the advantages of quinone-based polymers for supercapacitor applications.

4.2 Introduction

Globally, a record high of 37.4 Gt of CO_2 equivalents were produced in 2023, largely due to fossil fuel combustion, leading to catastrophic environmental and health damage.[1] The transportation sector alone accounts for about one third of these global CO_2 emissions statistics.[2] To decarbonize this sector, electric vehicles (EVs) have become more popular, making up 14% of global vehicle sales in 2022 [3].[4] [5] A study by the US Department of Energy determined that on a national average, the well-to-wheel emissions produced by EVs is approximately 5-fold lower than that of internal combustion engine vehicles.[6]

The higher power outputs, faster charge and discharge rates, and improved longevity together make supercapacitors viable technologies to work in tandem with LIBs in EVs to improve EV performance.[7][8] Supercapacitors can be used to assist the LIBs to deliver peak power outputs during rapid acceleration as well as to absorb energy more efficiently through regenerative braking.[9] Supercapacitor materials that can reach higher energy densities are critical for integration into EV power systems to extend the energy storage lifetimes.

Materials exhibiting a pseudocapacitive (PC) charge storage mechanism are of interest for their higher possible energy densities than electric double layer capacitance (EDLC) materials.[10], [11] Researching high energy density materials with PC mechanisms is imperative for improving the energy storage capabilities of supercapacitors to widen their scope of applicability. The most common PC materials in research are transition metal oxides (TMOs), however they remain constrained by their high cost and the adverse environmental effects of metals.[12], [13] These constraints make it imperative to explore alternative materials exhibiting low production and material costs with high energy densities. Conductive polymers (CPs) are a more recently emerging field as materials for supercapacitor applications, with just a few explored, such as polyaniline (PANi), polypyrole (PPy), and polythiophene.[14] CPs have easy syntheses, low costs, high possible energy densities, and are more mechanically robust than TMOs.[15] Polyimides are an intriguing class of polymers desirable for nitrogen-containing backbones providing low

HOMO/LUMO band gaps (improving electrical conductivity), accommodation of redox-active carbonyl functionalities with extended π-conjugated systems, and its hydrophilicity for high wettability in aqueous electrolytes. Polyimides have been studied in the field of aqueous rechargeable metal-ion batteries as very promising polymers for their high theoretical capacities, mechanical strength, and high cycling stabilities; however, they have yet to be extensively explored for supercapacitors applications.[16]

Quinones are considered promising candidates for organic electrodes due to their high redox activity, low material cost, ease of structural modifications, and environmental sustainability.[17] However, like many organic materials, they suffer from low electrical conductivity and dissolution in aqueous electrolytes. Polymerizing quinones has become a popular modification alternative to minimize dissolution during cycling while retaining the desirable electrochemical activity of quinones.[16]

The quinone, perylenetetracarboxylic dianhydride (PTCDA), was considered for polymerization for its reversible redox activity and π-conjugated structure for ease of electron transfer. [18], [19] PTCDA, like many organic molecules, suffers from poor cycling stability due to conductivity limitations and dissolution in the electrolyte. Polymerization of PTCDA to make a polyimide can be achieved using a diamine as a linker molecule.[20] Zhao et al researched polymerizing PTCDA with diamine moieties to improve its cycling stability for use in supercapacitors, however the alkyl chain diamines used adds additional weight to the molecule without additional redox activity, and was reported to disrupt the π-conjugation network which decreased the conductivity and charge transfer kinetics.[21] For these reasons, 2,6-diaminoanthraquinone (DAAQ) was therefore chosen as a diamine linker molecule for its π-conjugated structure and two additional redox-active groups. The resulting quinone-based polymer, poly-perylene-3,4,9,10-tetracarboxydiimide-anthraquinone (PPA), has been previously reported by Jiao et al to achieve capacitances up to 604 F g^{-1} at 5 mV s^{-1} (69.9% capacitance retention at 5 A g^{-1}).[22] A paper by Zhou et al reported another quinone-enriched polymer (PDQ) combined with rGO to produce a high performance supercapacitor electrode exhibiting capacitances up to 483.6 F g^{-1} at 5 mV s^{-1} and a capacitance retention of 87.8 % after 10,000 cycles.[23] Here, they demonstrated how polymerizing quinones provides high performance supercapacitor materials, however, this was achieved with reduced graphene oxide (rGO), a highly conductive carbon material that comes at a very high cost and requires additional

time-intensive preparation steps using toxic chemicals (e.g., hydrazine, sodium borohydride, hydroquinone) to prepare into an effective quinone-based composite electrode.[24]

Herein, we report a facile synthesis of PPA prepared as an organic molecule electrode (electrode) with low-cost, electrically conductive Ketjenblack EC-300J carbon black (CB) which itself has a specific surface area of approximately 800 m^2 g^{-1} and is designed for applications to increase the conductivity of polymers.[25] This electrode preparation method is extremely simple and industrially scalable compared to using rGO as a conductive carbon substrate, while demonstrating the impressive electrochemical capabilities of PPA as a supercapacitor material. The PPA electrode reported here exhibited capacitances up to 377 F g^{-1} at 5 mV s^{-1} and a capacitance retention of up to 65 % after 10,000 cycles at a very high scan rate of 100 mV s^{-1}. A pure PPA electrode (without conductive carbon substrate addition) exhibited capacitances up to 254 F g^{-1} at 5 mV s^{-1}, illustrating the impressive electrochemical energy storage capabilities of PPA for supercapacitor applications and providing motivation for the material's further electrochemical exploration.

4.3 Materials and Methods

4.3.1 Materials

All chemicals were reagent grade and used without any additional purification. Ketjenblack EC-300J Carbon Black (CB) was purchased from Fuel Cell Stores. 3,4,9,10-perylenetetracarboxylic dianhydride (PTCDA, 95%) and 2,6-diaminoanthraquinone (DAAQ) was purchased from AK Scientific. Zinc acetate dihydrate and Nafion 117 was purchased from Millipore Sigma. All solutions were prepared using Milli-Q Type 1 Ultra-Pure H_2O. Imidazole (99%) and N,N-dimethylformamide (DMF, 99.8%),was purchased from Fisher Chemicals.

4.3.2 Characterizations

Electrochemical testing was performed using a BioLogic SAS VSP-300 potentiostat. Fourier transform infrared (FT-IR) spectroscopy on PPA was conducted with a Thermo Scientific Nicolet 6700 FTIR. H^1 Nuclear Magnetic Resonance (NMR) spectroscopy was performed on a Bruker 600 Hz. To determine the crystallinity of the samples, x-ray diffraction crystallography was performed with a Cu K_α radiation source (λ=1.5418 Å) operating at 30 kV and 30 mA. The data was collected at diffraction angles between 0 to 50 degrees. Scanning electron microscopy was performed on an

FEI Magellan 400 to determine material morphology, and the uniformity of composition of the PPA/CB composite electrode. Samples were drop casted on Si wafers, with secondary detectors used throughout, as well as an Everhart-Thornley detector for low magnification images at a 4 mm working distance. A through lens detector was used in immersion mode for high magnification images at a 2 mm working distance.

4.3.3 Synthesis

PPA

In a round bottom flask, PTCDA (780 mg, 2.00 mmol), DAAQ (474 mg, 2.00 mmol), zinc acetate anhydride (367 mg, 2.00 mmol), and imidazole (20 g, 294 mmol) was combined and purged under an N_2 atmosphere. The mixture was then heated and stirred at 110°C for 3 hours, melting the imidazole and allowing the reagents to dissolve in it. The temperature was increased to 160°C to allow the reaction to proceed for 48 hours while stirring consistently. After the reaction, the material was cooled to room temperature, and removed from an N_2 atmosphere. 130 mL of Millipore Q water was added, and the resultant mixture was vacuum filtered. The remaining solid was then washed 5x with acetone and 3x with MeOH, to remove the imidazole, zinc acetate, and any unreacted PTCDA and DAAQ impurities. The product was then dried in an oven for at 60°C for 12 hours. Synthesis adapted from Jiao et al. [22]

PPA-CB(50)

In a round bottom flask, PTCDA (390 mg, 1.00 mmol), DAAQ (237 mg, 1.00 mmol), zinc acetate anhydride (183.5 mg, 1.00 mmol), 627 mg CB, and imidazole (10 g, 147 mmol) was combined and purged under an N_2 atmosphere. The mixture was then heated and stirred at 110°C for 3 hours, melting the imidazole and allowing the reagents to dissolve in it. The temperature was increased to 160°C to allow the reaction to proceed for 40 hours while stirring consistently. After the reaction, the material was cooled to room temperature, and removed from an N_2 atmosphere. 100 mL of acetone was added to dissolve the imidazole solvent for 1 hour, and the resultant mixture was washed and centrifuged 3x with acetone and 3x with MeOH, to remove the imidazole, zinc acetate, and any unreacted PTCDA and DAAQ impurities. The product was then dried in an oven for at 60°C for 12 hours. Synthesis adapted from Jiao et al. [22]

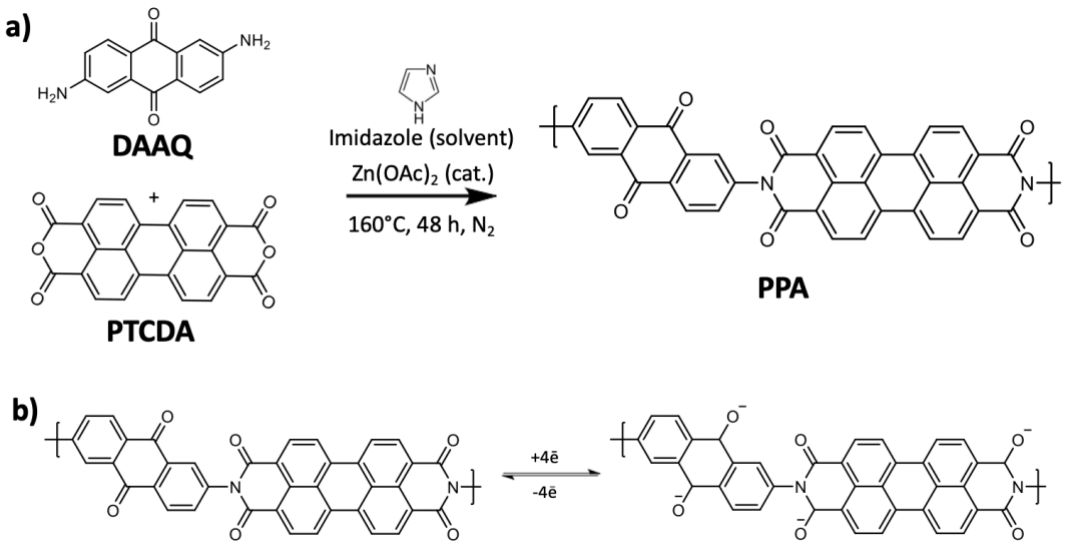

Figure 1: a) Synthesis of PPA from PTCDA and DAAQ in imidazole solvent with $Zn(OAc)_2$ catalyst. b) Proposed 4-electron transfer mechanism of the PPA units.

4.3.4 Electrochemical Measurements

All cyclic voltammetry (CV), galvanostatic charge discharge (GCD), and cycling stability tests were measured by a BioLogic SAS VSP-300 potentiostat through EC-Lab software. All measurements were set-up through a three-electrode system – a Pine glassy carbon working electrode, a graphite counter electrode, and a Pine Ag/AgCl reference electrode. To fabricate the working electrode, the as-synthesized PPA was sonicated with CB for 1 hour with different PPA percentages (30-100% PPA) of the total 5 mg PPA/CB composite in 5 mL DMF and 150 µL Nafion 117. Following sonication, The ink was drop-casted onto the glassy carbon electrode to achieve a mass loading of 34 µg cm^{-2}. The electrode was heated in a VWR forced air oven at 60°C for 15 minutes to evaporate DMF solvent and then allowed to return to room temperature. The electrode (denoted as 30-100% PPA) was placed in a three-electrode cell with 1 M H_2SO_4 electrolyte, which was purged with N_2 during and 20 minutes before all experiments commenced. To make PPA-CB(50), 5 mg was added to 5 mL DMF with 150 µL Nafion 117 and the electrode was prepared in the same method as previously described.

4.3.5 Calculations

Specific capacitance values (C_s, units of F g^{-1}) from CV data were calculated with **Equation 1**:

Equation 1:
$$C_s = \frac{\int I dV}{2 \cdot v \cdot \Delta V \cdot m}$$

Specific capacitance values (C_s, units of F g^{-1}) from GCD data were calculated with **Equation 2:**

Equation 2:
$$C_s = \frac{I}{\left(\frac{dV}{dt}\right)m}$$

In the above equations, I represents the current (A), v is the scan rate (mV s^{-1}), m is the mass of active material (g), t is the time (s) and ΔV is the potential window (V). The integral in the numerator of equation 1 was calculated using OriginPro mathematical software.

4.4 Results and Discussion

4.4.1 Characterization

The FTIR results presented in **Figure 2a** of PPA, PTCDA, and DAAQ provides evidence that the polymerization reaction has occurred. Comparing the spectra of PPA and PTCDA, there is a shift of the C=O peak (1770 cm^{-1}) from the carbonyl group of the anhydride group in PTCDA to 1670 cm^{-1} observed in PPA from the formation of an imide bond. Another observation is the almost complete elimination of the two primary amine (N-H) stretching vibration in DAAQ at 3319 and 3411cm^{-1}, and the N-H bending vibration shouldering at 3197 cm^{-1}. The lack of distinct N-H bands in the 3100-3450 cm^{-1} region of the PPA spectrum suggests there are very few terminal amino groups in PPA, and furthermore that PPA is likely made of polymeric chains rather than many smaller oligomeric units which would result in more terminal amino groups.

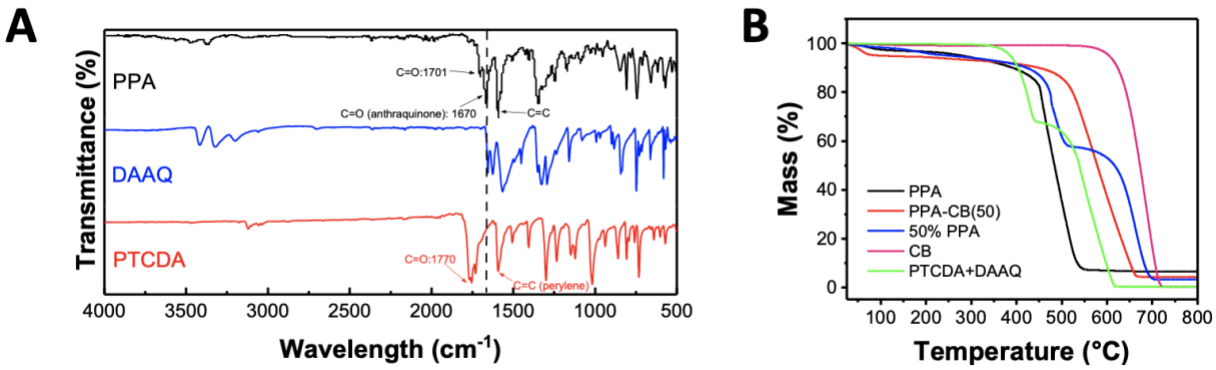

Figure 2: (a) FTIR Spectra For DAAQ, PTCDA, and PPA (b) TGA of PPA, 50% PPA, PPA-CB(50), CB, and PTCDA+DAAQ

TGA from **Figure 2b** shows the degradation of PPA, in which there are two mass loss events; the first is from the loss of water at 70-100°C, and the second is from PPA degradation from 450-525°C. There is residual mass after PPA degradation of 6.6%. This residual mass may be from Na, Zn, and Be impurities identified in the XPS of PPA (**Table S1).** The TGA of the PTCDA+DAAQ

monomers further provides evidence of polymerization, as unlike PPA, they have two distinct mass losses due to degradation, at 350-450°C and 450-620°C for DAAQ and PTCDA, respectively. The TGA of 50% PPA shows two mass loss events, the first being at 450°C from PPA, similarly to the temperature observed for the pure PPA TGA, while the second one is at 520°C from CB. Interestingly, the TGA for PPA-CB(50) (PPA synthesized in the presence of CB), shows only a single mass loss degradation event occurring despite PPA and CB being present in both samples.

The TGA results provides evidence that synthesizing PPA in the presence of CB may result in the PPA chains having increased intermolecular interactions with CB compared to post-synthesis mixing. PPA may transfer heat to the CB particles, such that CB acts as a heat stabilizer.[26] CB is known to increase the heat stability of polymeric compounds.[27] Furthermore, as synthesizing polymers *in situ* with CB has been shown to produce a more uniform composite and prevent reaggregation of CB,[28] it may contribute to the improved stability observed of the prepared electrode during cycling.

Figure 3 shows the XRD spectra of PPA, 50% PPA, and CB. The spectrum of PPA reveals the presence of crystallinity in the sample. There is a very intense peak at 12°, two sharp peaks at 17.5° and 18.5°, and two broad overlapping peaks 23.0° and 26.5°. The spectrum of PPA-CB exhibits the retention of the diffraction peaks of PPA with the exception of the replacement of the two broad peaks observed in PPA (23.0° and 26.5°) with a broad CB peak that appears to have shifted to a higher diffraction angle and overlapped the broad PPA peaks, suggesting the interlayer CB space distance has decreased due to more π–π interactions between PPA and CB.[22]

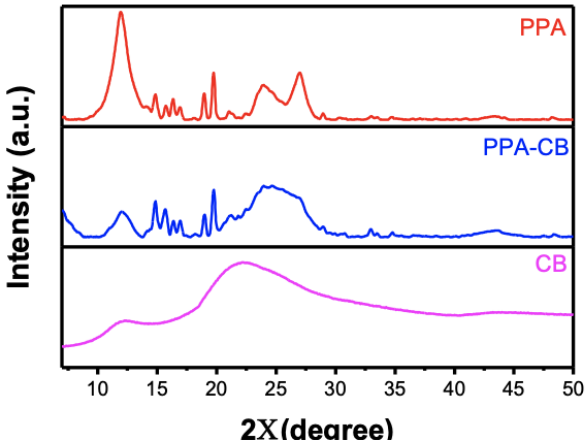

Figure 3: XRD of PPA, 50% PPA, and CB.

Figure 4 shows the SEM images of PPA, 50% PPA, and PPA-CB(50) prepared as an electrode on Si wafers. In **Figure 4a**, PPA is observed to be long and platelet-like in nature with non-uniform particle sizes and a porous framework. **Figures 4b** shows the 50% PPA composite at various magnifications, where there is clear evidence of a composite of PPA with highly porous CB intertwined around the platelets. This conductive CB framework is what increases the conductivity of the electrode, as shown in the EIS results in **Figure 8a** of the charge transfer resistance reduction following CB addition to the PPA electrode. **Figures 4c** show the PPA-CB(50) electrode. **Figure 4b** shows a very large PPA agglomerate with CB compared to well dispersed PPA particles in **Figure 4c**, providing evidence as to why the capacitance of PPA-CB(50) was lower than for the 50% PPA electrode. However, the CB network of PPA-CB(50) appears to be well wrapped around the PPA particle, covering it entirely, resulting in improved intermolecular interactions between PPA and CB compared to synthesizing PPA in the absence of CB. These more intimate interactions may contribute to the improved cycling stability of the PPA-CB(50) electrode and the observation of a single mass loss event in the TGA analysis.

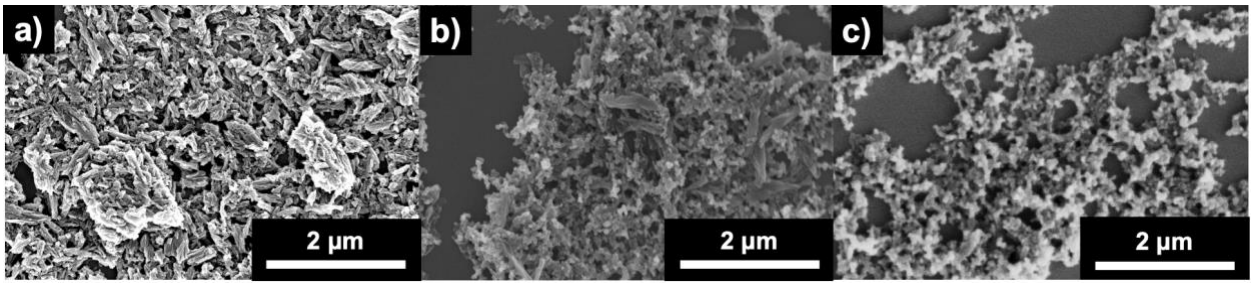

Figure 4: SEM images of (a) 100% PPA, (b) 50% PPA, and (c) PPA-CB(50), all prepared as an electrode on Si wafers.

Using an elemental analyzer, the percentage of PPA present in the PPA-CB(50) material was calculated. From **Table S2**, comparing the ratio of nitrogen between the sulfanilamide standard to both PPA and PPA-CB(50) allowed the relative percentages of nitrogen between PPA and PPA-CB(50) to be calculated. Since the PPA-CB(50) sample had only 4.84 % nitrogen, compared to 10.02 % nitrogen that would be present in the pure PPA sample, it can be estimated that the PPA-CB(50) PPA content is approximately 50%.

The X-ray photoelectron spectroscopy (XPS) analysis provided a detailed examination of the chemical composition and bonding characteristics of the 100% PPA, 50% PPA, and PPA-CB(50) electrode materials. The higher C atomic percentage of 50% PPA (95 at% C) in contrast to PPA-

CB(50) (90% at% C), accompanied by increases in O (6.83 at%) and N (3.44 at%) compared to 50% PPA (2.99 at% O and 1.61 at% N) suggests that PPA synthesis in the presence of CB integrates more foreign atoms into the carbon structure than if CB was added following PPA synthesis (**Table S1**). The high-resolution C 1s spectra reveal several critical observations (**Figure S2**). Firstly, the content of C-C/C-H significantly declines from 100% PPA to both PPA/CB composite samples, indicating that the incorporation of CB diminishes the relative amount of C in C-C and C-H configurations. This reduction is most pronounced in PPA-CB(50). The relative C=O and C-O-C/C-OH content is higher in PPA-CB(50) than 50% PPA as well, likely why there is a reduction in C-C/C-H bonding upon CB addition during PPA synthesis. The presence of a π-π satellite peak in PPA-CB(50) indicates stronger surface interactions between the PPA and CB. A π-π satellite peak is also observed in the PPA C1s spectra at a lower binding energy, attributed to interactions among the aromatic groups within the planar PPA molecules. 50% PPA has no observed π-π satellite peak, indicating CB addition post synthesis disperses PPA particles well, however, does not result in as strong π-π interactions of PPA with CB as when CV is added during synthesis. This can contribute to the improvement in cycling stability observed from the PPA-CB(50) electrode over the 50% PPA electrode. The O1s spectra further show that the ratios of C=O to C-O is 37% higher for PPA-CB(50) than 50% PPA, suggesting that the modified synthesis method may encourage carbon oxidation, potentially decreasing the electrical conductivity of the PPA-CB(50) electrode resulting in lower capacitances than the 50% PPA electrode exhibits. However, XPS analysis and EIS testing on CB following exposure to synthesis conditions without PPA reagents showing a similar C=O/C-O ratio to PPA-CB(50) would provide more evidence of this observation. The N1s spectra reveals the presence of N-C3 and terminal NH_2 peaks, indicating varied nitrogen environments influenced by material preparation methods. However, the mild variations in NH_2 to N-(C3) ratios among the samples suggest that the nitrogen content within PPA maintains having an intact chemical structure across both mixing methods. Overall, these observations demonstrate how PPA synthesis in the presence of CB, appears to create a more reactive interface between PPA and CB, leading to altered chemical structures that could significantly influence the material's properties.

4.4.2 Electrochemical Performance

Following the successful synthesis of PPA, it was dispersed with CB in either ethanol or dimethylformamide (DMF) to identify which of the two solvents best disperse the materials together via sonication to make an electrode, as described in the materials and methods section. The difference in the overall size of their CVs in **Figures S3a** and **S3b** show how DMF provides higher capacitances, as per **Equation 1** where the numerator describes the proportionality of CV area to capacitance. There is a 35% and 53% increase in capacitance for the electrodes prepared with DMF dispersion for 50% and 80% PPA, respectively. PPA is a very polar material found only to dissolve in concentrated H_2SO_4, which was polar enough to solubilize it for NMR spectroscopy due to its very strong protonation ability.[29] DMF has a considerably higher dipole moment than ethanol, at 12.88 C·m, compared to 5.60 C·m for ethanol.[30] This accounts for the improved dispersion of PPA with CB, allowing for less aggregation, more available surface area, and a higher level of PPA contact with CB. As observed in the CVs in **Figures S3a** and **S3b**, the EDLC predominant potential range as per its characteristic rectangular shape (0.4 to 0.8 V vs RHE) increases in area considerably between EtOH and DMF dispersed PPA electrode's, which SEM images in **Figure S4** provide compelling evidence showing there is a much more uniformly dispersed layer in the DMF-dispersed PPA electrode than the local agglomerations found in the EtOH-dispersed sample, allowing for a more complete conductive network around PPA particles for efficient charge transfer. EDX mapping of the PPA electrodes prepared in DMF and EtOH show much more uniformly distributed nitrogen, corresponding to the nitrogen present in PPA (**Figure S5**). Proper dispersion of supercapacitor pseudocapacitive materials in carbon matrices during electrode preparation is well documented to be an important factor contributing to the higher specific capacitances observed for them.[31] These results indicate the vast difference that solvents used during electrode preparation can have on the performance of PPA and provide direction for further in-depth analysis of specific PPA interactions with DMF or other solvents.

Composites of PPA and CB were made with increasing percentages of PPA to CB content, ranging from 30-100%, as described in the *Materials and Methods* section. 80% PPA achieved the highest capacitance of 377 F g^{-1} at 5 mV s^{-1}, as shown in **Figure 5a**. However, at faster scan rates (50 mV s^{-1} and 100 mV s^{-1}), 70% PPA achieved superior capacitances to the other ratios tested at the same rate. Even with the marginal difference in optimal PPA electrode compositions depending on the scan rate, these results illustrate how PPA can achieve very high capacitances with high PPA

loading percentages, even delivering up to 254 F g^{-1} at 5 mV s^{-1} without the addition of any conductive additive such as CB (pure PPA electrode). Comparing this performance to that of pure polyaniline (PANI), the most extensively researched conducting polymer for supercapacitor applications, which only exhibited up to 115 F g^{-1} at 1 mV s^{-1}, there is a clear demonstration of high capacitances achievable with PPA.[32] This demonstrates the marvellous energy storage capabilities and electrochemical activity PPA exhibits, making it an incredibly desirable material to further research. PPA has remarkable electroactivity, achieving peak capacitances with a very low percentage of CB required to improve its capacitance by adding a conductive network. GCD testing was performed on the 50%, 80%, and 100% PPA electrodes as well (**Figure 5d-f**). The GCD curves for each show distinct plateaus occurring during charging and discharging, which are consistent with the potential at which redox peaks are observed in the CV curves. The curve displayed a high degree of symmetry between charging and discharging, reflecting the PPA electrode's high degree of reversibility.

The PPA-CB(50) electrode material has a lower capacitance (319 F g^{-1} at 5 mV s^{-1}) than the *ex situ* mixed 50% PPA electrode (295 F g^{-1} at 5 mV s^{-1}) of an equivalent PPA/CB composition (**Figure S6a)**. However, the capacitance retention of PPA-CB(50) after 10,000 cycles was 64%, a 3% improvement from the 50% PPA capacitance retention of 61%. This stability improvement can be attributed to the increase in π–π interactions of the PPA-CB(50) composite compared to 50% PPA, as observed in XPS (**Figures S2**). The lower capacitance may be attributed to improperly dispersed CB during PPA synthesis, resulting in PPA integrating itself scarcely between large agglomerates of CB, rather than small CB particles, as seen in **Figure 4b and 4c**.

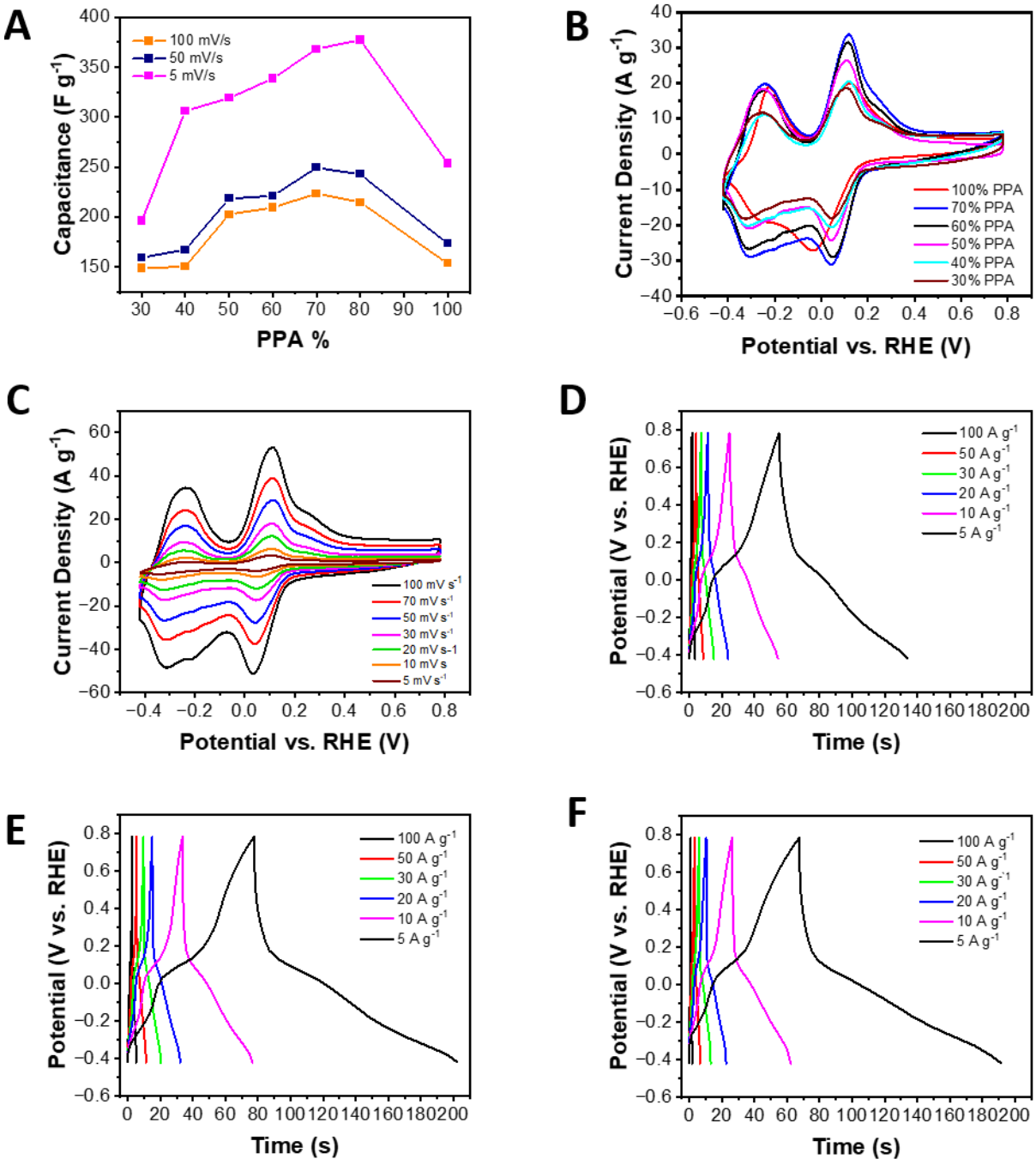

Figure 5: (a) Different compositions the PPA electrode at 50 mV s^{-1} in 1 M H_2SO_4 (b) CVs of different compositions of PPA electrode at 50 mV s^{-1} (c) CVs of 50% PPA electrode at scan rates from 5 to 100 mV s^{-1}. (d) GCDs of 50% PPA at current densities from 5 to 100 A g^{-1}. (e) GCDs of 80% PPA electrode at current densities from 5 to 100 A g^{-1}. (f) GCDs of 100% PPA electrode at current densities from 5 to 100 A g^{-1}.

4.4.3 Rate Capability

The rate capability of 80% PPA and 50% PPA electrode compositions were tested to determine if CB content affected the rate performance of PPA between 5-100 mV s^{-1}, as shown in **Figure 6a**. Results showed that the rate was not particularly sensitive to CB addition. Furthermore, the PPA-CB(50) rate capability was compared to the 50% PPA electrode. The rate capability was reduced by 2.1% with PPA-CB(50).

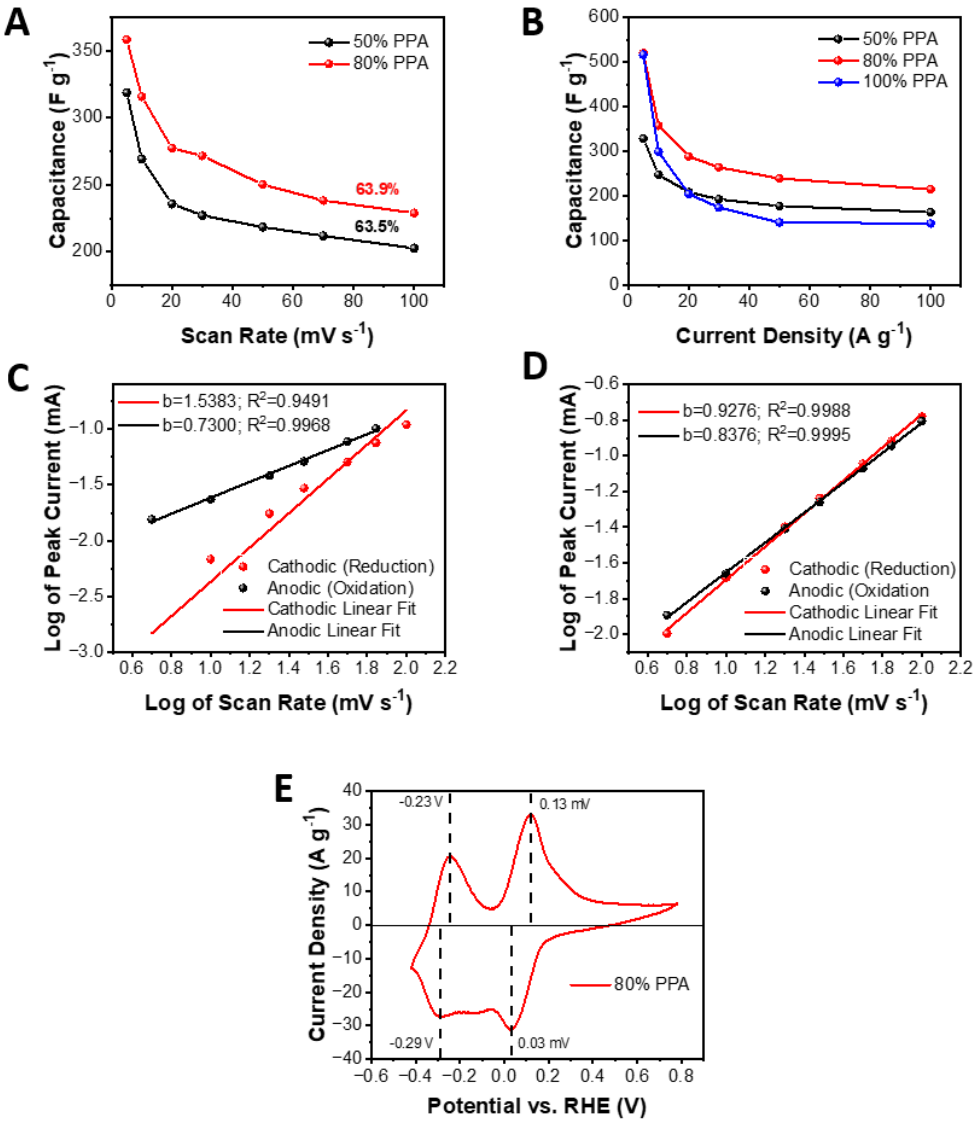

Figure 6: Rate capability of PPA at (a) 50% PPA and 80% PPA electrode composition, and (b) Rate capability of 50% PPA at current densities from 2 to 100 A g^{-1}. (c) The evaluation of the b value for the peak 1 cathodic (reduction) and anodic (oxidation) peak current densities of the 80% PPA electrode from experimental CV tests at different scan rates (5 to 100 mV s^{-1}). (d) The evaluation of the b value for the peak 2 cathodic (reduction) and anodic (oxidation) peak current densities of the 80% PPA electrode from experimental CV tests at different scan rates (5 to 100 mV s^{-1}). (e) 80% PPA reduction and oxidation peak current separation at 50 mV s^{-1}.

To provide insight on the relationship between the scan rate and the peak current observed, the reaction kinetics could be further quantified by the power law formula:

Equation 3: $$i = av^b$$

where i is the cathodic peak current observed at the scan rate, v, related by constants a and b. The constant, b, is of particular importance as it provides meaningful insight as to whether the PPA electrode redox activity is under more surface-controlled (b=1) or diffusion (b=0.5) controlled processes. [33] When the b value is equal to 1, the material is said to exhibit a supercapacitor-type material, while a b value of 0.5 is more representative of a battery-type material.[34] The power law relating the peak cathodic and anodic currents to a range of scan rates (5 to 100 mV s^{-1}) was plotted for the two pairs of peaks of the 80% PPA electrode , as shown in **Figure 6c,d**. A constant was determined by the y-intercept of the linear relationship between current and scan rate, with the b value being the slope. For peak pair 2, the cathodic and anodic b values are close to 1, suggesting the redox reactions observed are predominantly surface-controlled (capacitive process) rather than diffusion controlled. Peak pair 1 has an unusual cathodic b value of 1.5383. A theory for this observation is that the peak pair 1 redox reaction close to the lower potential range limit, close to where the hydrogen evolution reaction (HER) would be observed. The redox peaks may mask minimal evidence of HER occurring. A repeated experiment without active material on the electrode may make possible HER more visible, confirming this hypothesis.

4.4.4 Capacitance Retention

The capacitance retention of PPA was measured by performing 10,000 oxidation and reduction cycles at a fast scan rate of 100 mV s^{-1}, to more closely emulate the rate at which a supercapacitor material would operate at. The capacitance retention of PPA was found to be dependent on its composite ratio with CB. **Figure 7a** shows while the capacitance retention of 100% PPA is only 47% it drastically increases with the addition of CB, with 58%, 61%, and 65% for 80%, 50%, and 30% PPA, respectively. This trend demonstrates how CB addition to the PPA electrode through a simple preparation method (see *Materials and Methods*) creates a more durable supercapacitor electrode over continuous cycling, although there is a trade-off with decreased specific capacitance, as illustrated in **Figure 5a**. From the CVs showing the degradation over the course of the 10,000 cycles (**Figure 5b-d**), its observed that the individual redox peak size are what are significantly lost, rather than the EDLC component that is visible from the 0.4 to 0.8 V vs RHE

range, which appears to retain its size and shape. Specifically, there is a more significant drop in redox activity coming from the redox peak pair corresponding to the anthraquinone monomeric unit from DAAQ, in comparison to the perylene moiety from PTCDA which appears to retain more of its redox peak size throughout repeated cycling. This can be attributed to the increased barrier of electron transfer for the reversible reaction of the carbonyl groups of the anthraquinone moiety, as deduced by its oxidation and reduction peak-to-peak separation (ΔE_p) of approximately 104 mV in the CV at 100 mV s^{-1}, compared to the perylene moiety which exhibits approximately a ΔE_p of only 53 mV (**Figure 6e**). This higher barrier for electron transfer translates to a less favourable reversible reaction, where over 10,000 cycles of oxidation and reduction this can cause reduced species to not be once again oxidized over time [35], [36]

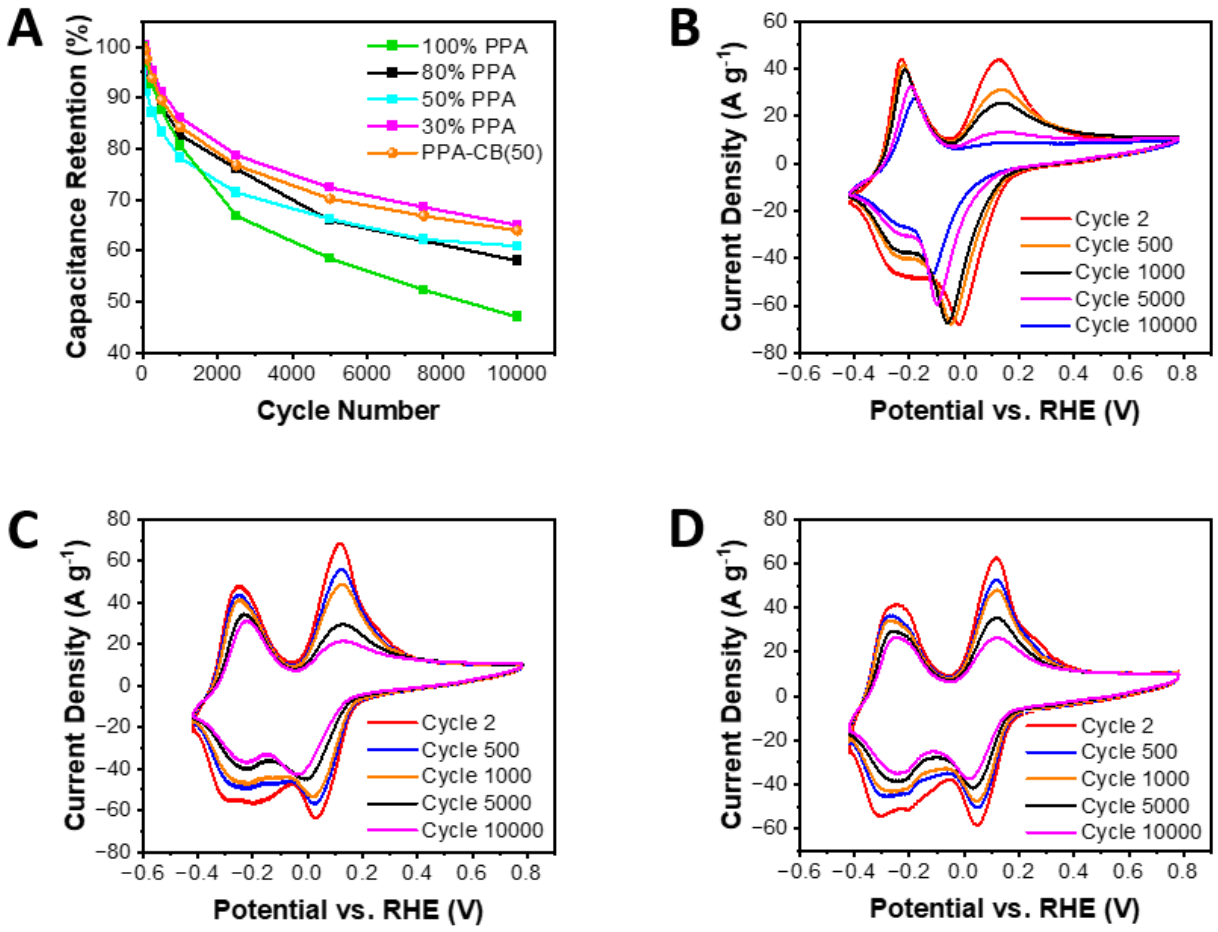

Figure 7: (a) Comparison of Capacitance retention over 10,000 cycles for different PPA electrode compositions and the *in situ* synthesis; (b) 100% PPA (c) 80% PPA (d) 50% PPA.

4.4.5 Electrochemical Impedance Spectroscopy (EIS)

The charge transfer resistivity of the 100% PPA electrode and 80% PPA electrode were 5.2 W and 4.7 W, respectively (**Figure 8a**). The addition of CB to the 80% PPA electrode increased the electrical conductivity, allowing for a lower resistive barrier to charge transfer. The charge transfer resistance was also collected before and after 10,000 oxidation and reduction cycles at 100 mV s^{-1} for the 80% PPA electrode (**Figure 8b**) Results show how the charge transfer resistance increases from 4.7 Ω to 5.2 Ω following cycling, revealing that the electrical conductivity of the PPA electrode decreases and the charge transfer resistance increases from continuous cycling.[37] The increase in charge transfer resistance poses as a barrier for electron transfer to occur over time, resulting in lower capacitance retention.

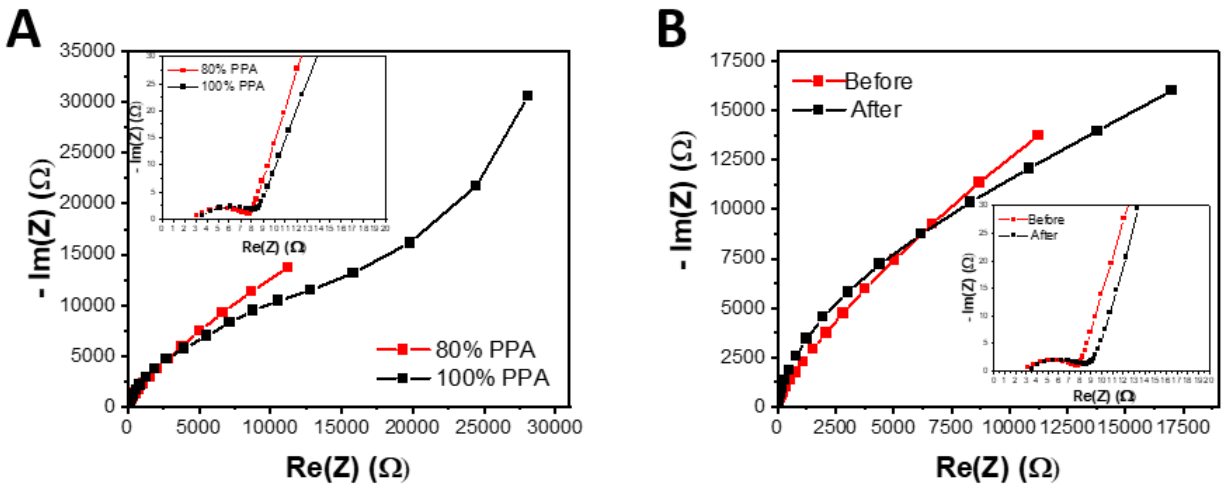

Figure 8: Nyquist plots of (a) 80% PPA and 100% PPA electrodes, and (b) 80% PPA electrode before and after 10,000 cycle stability testing at 100 mV s^{-1}.

4.5 Conclusion

This work presents vast opportunities of organic pseudocapacitive materials for supercapacitor applications. PPA demonstrated a facile synthesis and the electrochemical storage capabilities of it when incorporated with the low cost, high surface area CB, delivering capacitances of up to 377 F g^{-1} at 5 mV s^{-1}. PPA has two pairs of redox reactions occurring at -0.23/-0.29 and 0.13/0.03 V vs RHE that have varying capacitive and diffusive behaviour as well as degradation rates over cycling. Changing the CB composition in the PPA electrode affected the cycling stability, with higher electrode stability found with higher CB content. Modifying the electrode material synthesis by adding CB during PPA synthesis increased the number of π–π interactions between PPA and

CB, contributing the improved cycling stability of it compared to its equivalent PPA electrode prepared with CB addition following PPA synthesis. This data provides valuable directions for further development of PPA electrodes with CB using modified synthesis approaches and facile electrode preparation methods for applications as a scalable supercapacitor material.

4.6 Supplementary Figures

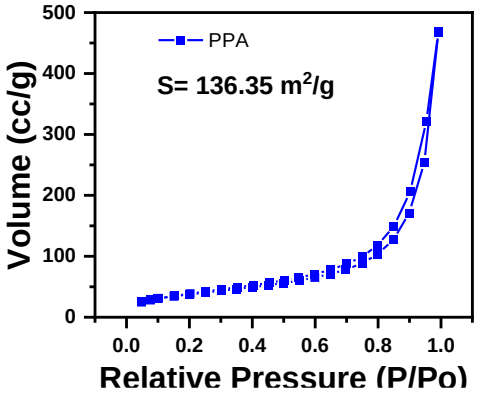

Figure S1: BET N_2 adsorption-desorption isotherm of PPA

Table S1: XPS survey spectra atomic percentages of PPA, 50% PPA, and PPA-CB(50).

	O 1s (At%)	**C 1s (At%)**	**N 1s (At%)**	**Na 1s (At%)**	**Zn 2p (At%)**	**Be 1s (At%)**
PPA	10.26	79.12	8.14	0.06	0.44	1.97
50% PPA	2.99	95.40	1.61	N/A	N/A	N/A
PPA-CB(50)	6.83	89.68	3.44	N/A	0.05	N/A

Table S2: Use of Elemental Analysis of PPA and PPA-CB(50) compared to a sulfanilamide standard to determine the PPA content in the PPA-CB(50) synthesis.

Sample	**Ratio of N Content in Sulfanilamide to Sample**	**Percentage of N (%)**
PPA	1.62	10.02
PPA-CB(50)	3.36	4.84

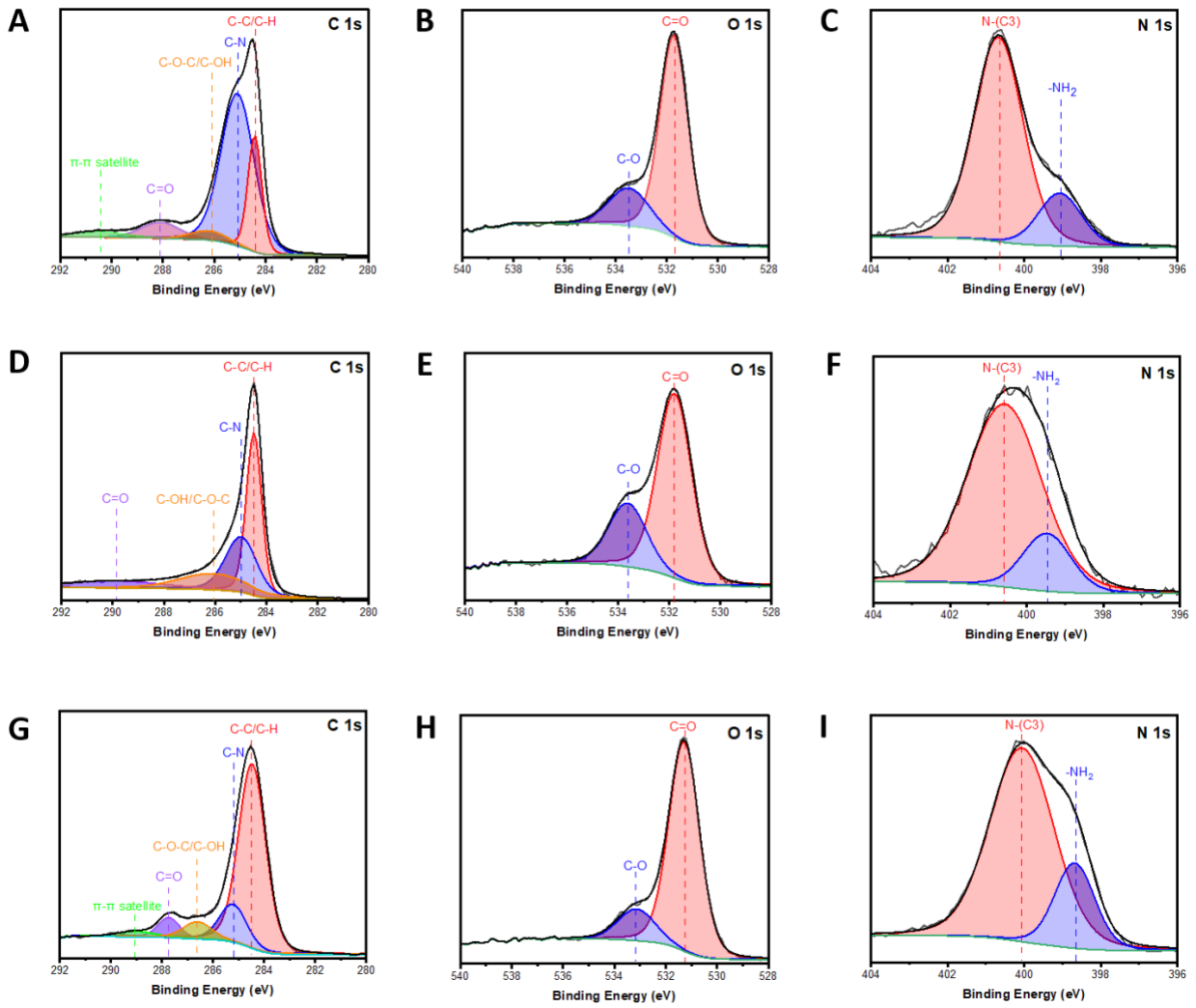

Figure S2: XPS of the C 1s, O 1s, and N 1s of (a-c) PPA-CB(50), (d-f) 50% PPA, and (g-i) 100% PPA electrode materials.

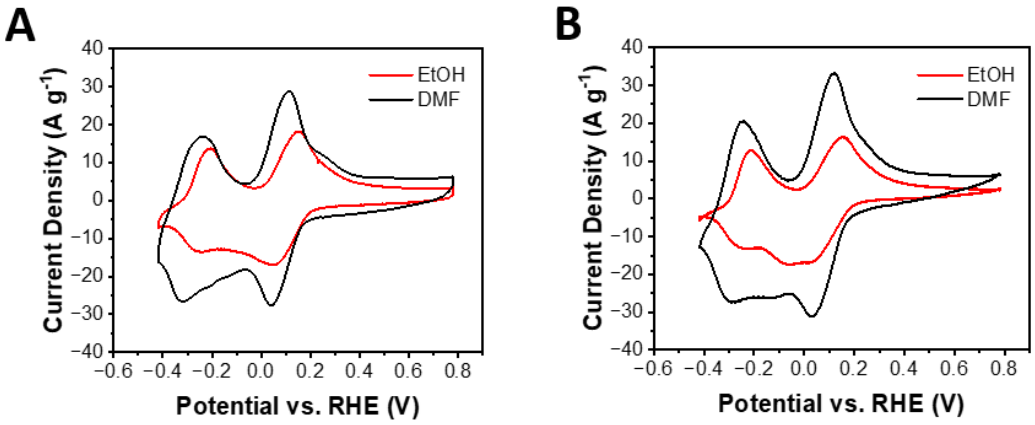

Figure S3: CVs of PPA electrode prepared via dispersion in either EtOH or DMF a) 50% PPA b) 80% PPA.

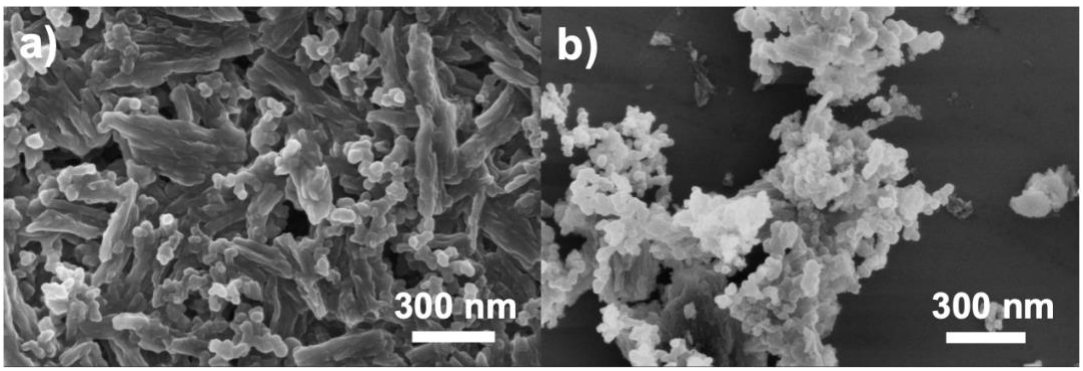

Figure S4: 80% PPA electrode SEM prepared in (a) DMF and (b) EtOH solvents.

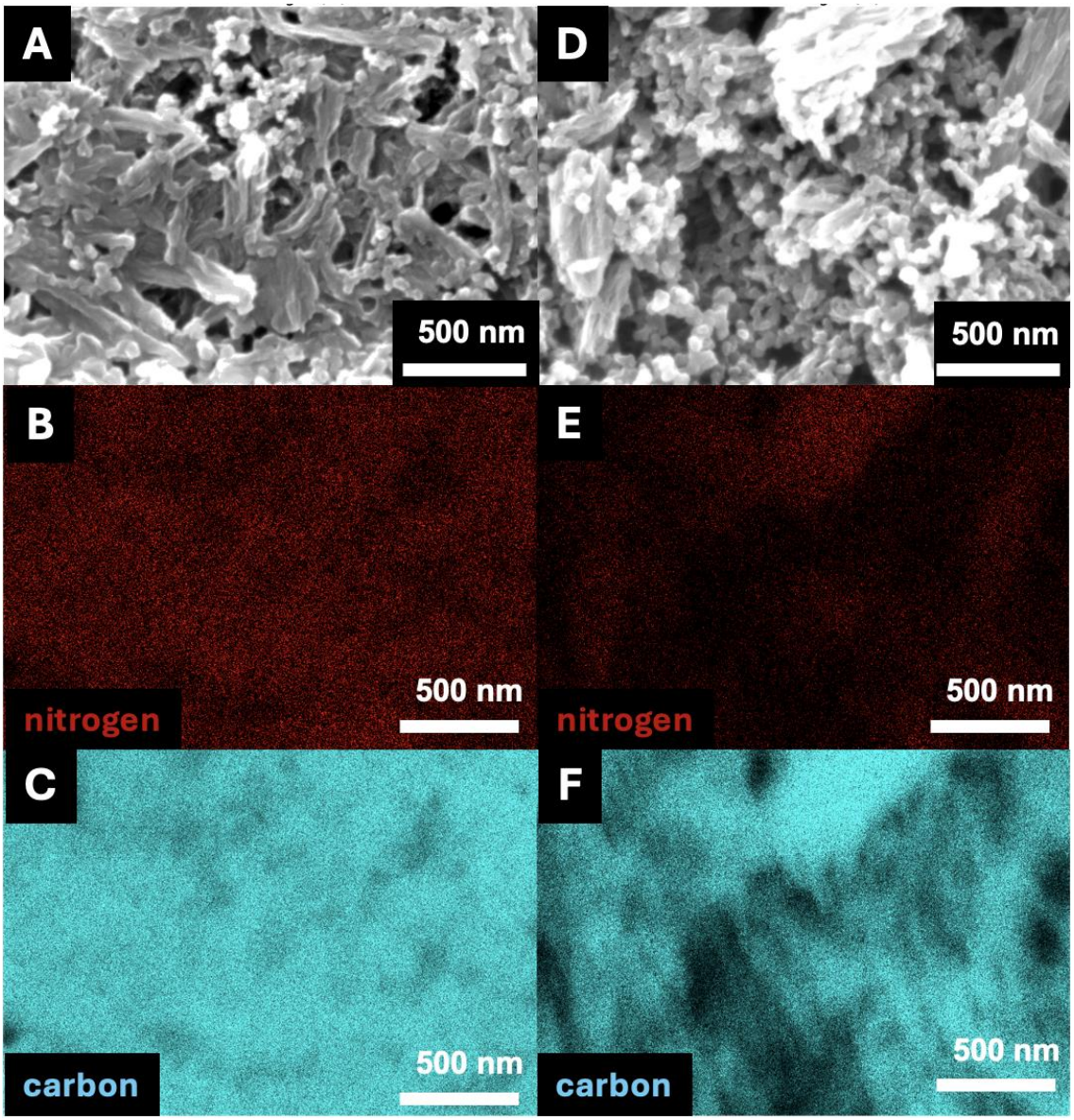

Figure S5: EDX nitrogen and carbon maps of 50% PPA electrode prepared in (a-c) DMF and (d-f) EtOH solvents.

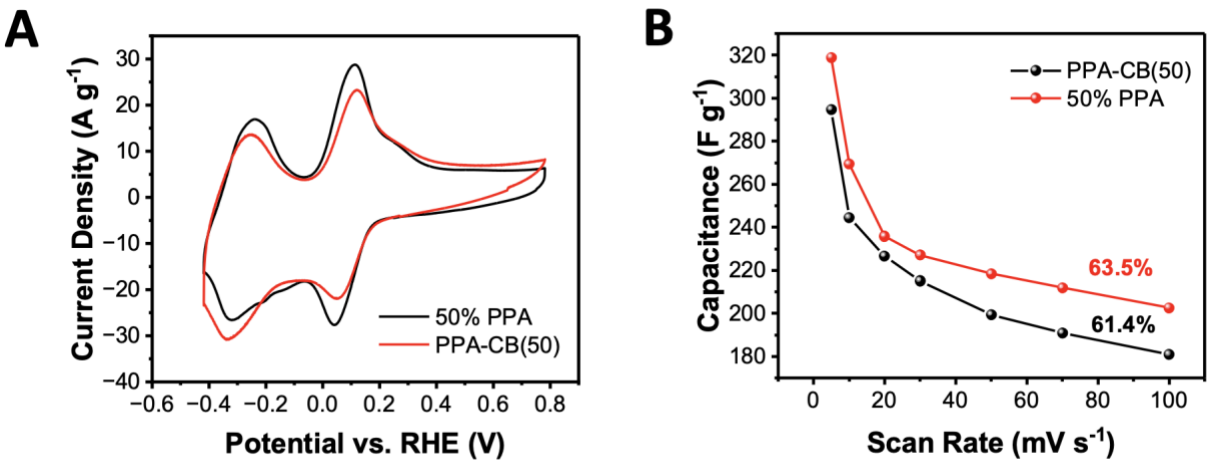

Figure S6: (a) CV of 50% PPA and PPA-CB(50) at 50 mV s^{-1}. (b) Rate capability of PPA of 50% PPA and 80% PPA electrode compositions.

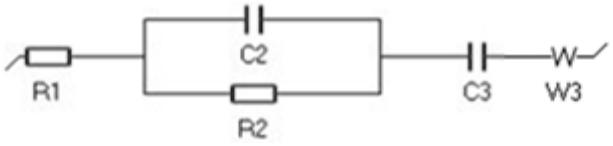

Figure S7: The equivalent circuit for the Nyquist plot.

4.7 References

[1] "CO2 Emissions in 2023," 2023. [Online]. Available: https://www.iea.org/reports/co2-emissions-in-2023.

[2] "Greenhouse Gas Emissions," *Canada, Natural Resources*, 2022. [Online]. Available: https://www.canada.ca/en/environment-climate-change/services/environmental-indicators/greenhouse-gas-emissions.html.

[3] V. Singh, V. Singh, and S. Vaibhav, "A review and simple meta-analysis of factors influencing adoption of electric vehicles," *Transp. Res. Part D Transp. Environ.*, vol. 86, no. August, p. 102436, 2020.

[4] "CO2 Emissions in 2022," *International Energy Agency*, 2022. [Online]. Available: https://www.iea.org/reports/co2-emissions-in-2022.

[5] "Zero emissions vehicle infrastructure program," *Natural Resources Canada*, 2022. [Online]. Available: https://natural-resources.canada.ca/energy-efficiency/transportation-alternative-fuels/zero-emission-vehicle-infrastructure-program/21876.

[6] "Emissions from electric vehicles," *U.S Department of Energy*, 2021. [Online]. Available: https://www.google.ca/url?sa=t&source=web&rct=j&opi=89978449&url=https://afdc.energy.gov/vehicles/electric_emissions.html&ved=2ahUKEwiMuLm4w6aFAxWUMjQIHU28APIQFnoECA4QAQ&usg=AOvVaw0N9neVabd7m4fjJumOJnSA.

[7] S. Manoharan, K. Krishnamoorthy, A. Sathyaseelan, and S. J. Kim, "High-power graphene supercapacitors for the effective storage of regenerative energy during the braking and deceleration process in electric vehicles," *Mater. Chem. Front.*, vol. 5, no. 16, pp. 6200–6211, 2021.

[8] N. Devillers, S. Jemei, M. Péra, D. Bienaimé, and F. Gustin, "Review of characterization methods for supercapacitor modelling," *J. Power Sources*, vol. 246, pp. 596–608, 2014.

[9] H. Xu and M. Shen, "The control of lithium-ion batteries and supercapacitors in hybrid energy storage systems for electric vehicles: A review," *Int. J. Energy Res.*, vol. 45, no. 15, pp. 20524–20544, 2021.

[10] R. H. Deblock, “Achieving high energy density and high power density with pseudocapacitive materials,” *Nat. Rev. Mater.*

[11] S. Fleischmann *et al.*, “Pseudocapacitance: From Fundamental Understanding to High Power Energy Storage Materials,” *Chem. Rev.*, vol. 120, no. 14, pp. 6738–6782, 2020.

[12] M. Cui and X. Meng, “Nanoscale Advances Overview of transition metal-based composite materials for supercapacitor electrodes,” pp. 5516–5528, 2020.

[13] W. Raza *et al.*, “Recent advancements in supercapacitor technology,” *Nano Energy*, vol. 52, no. July, pp. 441–473, 2018.

[14] Q. Li, M. Horn, Y. Wang, J. Macleod, N. Motta, and J. Liu, “A Review of Supercapacitors Based on Graphene and Redox-Active Organic Materials,” 2019.

[15] M. Amirul, A. Mohd, N. Hawa, N. Azman, S. Kulandaivalu, and Y. Sulaiman, “Review of the use of transition-metal-oxide and conducting polymer-based fi bres for high-performance supercapacitors,” vol. 186, 2020.

[16] A. Mauger, C. Julien, A. Paolella, M. Armand, and K. Zaghib, “Recent progress on organic electrodes materials for rechargeable batteries and supercapacitors,” *Materials (Basel).*, vol. 12, no. 11, pp. 1–57, 2019.

[17] S. P. Ega and P. Srinivasan, “Quinone materials for supercapacitor: Current status, approaches, and future directions,” *J. Energy Storage*, vol. 47, no. September 2021, p. 103700, 2022.

[18] F. Ma *et al.*, “Organic Molecular Electrode with Ultrahigh Rate Capability for Supercapacitors,” 2020.

[19] L. Wang *et al.*, “Conjugated molecule functionalized graphene films for energy storage devices with high energy density,” *Electrochim. Acta*, vol. 340, p. 135804, 2020.

[20] R. V Ghorpade, J. E. Soc, and M. Jung, “Polyimide Containing Tricarbonyl Moiety as an Active Cathode for Rechargeable Li-Ion Batteries Polyimide Containing Tricarbonyl Moiety as an Active Cathode for Rechargeable Li-Ion Batteries,” 2018.

[21] Y. Zhao *et al.*, “A ? -Conjugated Polyimide-Based High-Performance Aqueous

Potassium-Ion Asymmetric Supercapacitor," vol. 2200040, pp. 1–8, 2022.

[22] L. Jiao *et al.*, "A novel organic molecule electrode based on organic polymer functionalized graphene for supercapacitor with high-performance," *J. Energy Storage*, vol. 52, no. PA, p. 104777, 2022.

[23] Y. Zhou *et al.*, "Synthesis and capability evaluation of quinone-enriched polymer with extended π-conjugated and contorted structures for efficient energy storage," *Electrochim. Acta*, vol. 476, no. November 2023, p. 143693, 2024.

[24] L. Stobinski *et al.*, "Graphene oxide and reduced graphene oxide studied by the XRD, TEM and electron spectroscopy methods," *J. Electron Spectros. Relat. Phenomena*, vol. 195, pp. 145–154, 2014.

[25] C. A. S. No, E. No, A. Pore, M. Volatiles, and A. Fines, "Ketjenblack EC-300J," 2011.

[26] C. H. Chen, H. C. Li, C. C. Teng, and C. H. Yang, "Fusion, electrical conductivity, thermal, and mechanical properties of rigid poly(vinyl chloride) PVO/carbon black (CB) composites," *J. Appl. Polym. Sci.*, vol. 99, no. 5, pp. 2167–2173, 2006.

[27] A. Shenavar and F. Abbasi, "Morphology, thermal, and mechanical properties of acrylonitrile–butadiene–styrene/carbon black composites," *J. Appl. Polym. Sci.*, vol. 105, no. 4, pp. 2236–2244, 2007.

[28] Y. Liu and X. Li, "Effect of Dispersion of Carbon Black on Electrical and Thermal Properties of Poly (Ethylene Terephthalate)/ Carbon Black Composites," no. September 2008, pp. 146–156, 2009.

[29] Y. Hu *et al.*, "Novel Insoluble Organic Cathodes for Advanced Organic K-Ion Batteries," *Adv. Funct. Mater.*, vol. 30, no. 17, pp. 1–10, 2020.

[30] C. Zhang, J. Wang, and Y. Wang, "Solubility of ceftriaxone disodium in acetone, methanol, ethanol, N,N,-dimethylformamide, and formamide between 278 and 318 K," *J. Chem. Eng. Data*, vol. 50, no. 5, pp. 1757–1760, 2005.

[31] A. Borenstein, O. Hanna, R. Attias, S. Luski, T. Brousse, and D. Aurbach, "Carbon-based composite materials for supercapacitor electrodes: A review," *J. Mater. Chem. A*, vol. 5,

no. 25, pp. 12653–12672, 2017.

[32] J. Yan *et al.*, "Preparation of graphene nanosheet/carbon nanotube/polyaniline composite as electrode material for supercapacitors," *J. Power Sources*, vol. 195, no. 9, pp. 3041–3045, 2010.

[33] L. Hou, C. Kong, Z. Hu, Y. Han, and B. Wu, "Redox active organic molecule-Emodin modified graphene for high-performance supercapacitors," *J. Electroanal. Chem.*, vol. 895, no. 145, p. 115402, 2021.

[34] U. Aziz, M. Z. Iqbal, S. Aftab, S. M. Wabaidur, and M. J. Iqbal, "Exploring the Redox Activity of a Transition-Metal-Intercalated 1,3,5-Benzenetricarboxylic Acid Organic-Inorganic Network for Potential Battery-Supercapacitor Applications," *Energy and Fuels*, vol. 37, no. 8, pp. 6248–6256, 2023.

[35] N. Elgrishi, K. J. Rountree, B. D. McCarthy, E. S. Rountree, T. T. Eisenhart, and J. L. Dempsey, "A Practical Beginner's Guide to Cyclic Voltammetry," *J. Chem. Educ.*, vol. 95, no. 2, pp. 197–206, 2018.

[36] F. Marken, A. Neudeck, and A. M. Bond, "Cyclic Voltammetry," in *Electroanalytical Methods*, Springer, Berlin, Heidelberg, 2010, pp. 57–106.

[37] P. Zhang *et al.*, "Capacitance fading mechanism and structural evolution of conductive polyaniline in electrochemical supercapacitor," *J. Mater. Sci. Mater. Electron.*, vol. 31, no. 17, pp. 14625–14634, 2020.

CHAPTER 5

5. Conclusion and Suggested Future Work

In conclusion, the work of this thesis focused on the evaluation of organic supercapacitor materials that have been explored minimally in the energy storage field. The work aimed to demonstrate the opportunities organic materials have as a more sustainable and cost-effective alternative to the extensive metal-based materials researched. More specifically, comprehensive analysis of two molecules was performed and presented across two papers: one on the polymer, PPA, and the other on the trimeric analogue of PPA, PDI-DAQ, to pave a path for future research. This analysis has provided valuable insights and demonstrated the promising electrochemical capabilities of both PPA and PDI-DAQ as supercapacitor electrode materials. To fabricate the supercapacitor electrode, both materials were both incorporated with a low-cost, conductive, high surface area CB via a simple preparation method. Using CB as a carbon material offered a realistic approach of testing PPA and PDI-DAQ by showcasing opportunities for potential scalability of the electrode preparation via avoiding high material costs and complicated preparation processes.

Testing PPA and PDI-DAQ aimed to discern the impact molecule size had on the electrochemical energy storage capabilities of the structures in supercapacitors. PPA exhibited slightly higher capacitances than PDI-DAQ (377 F g^{-1} verses 318 F g^{-1}, respectively), however the cycling stability and rate capability appeared to be very comparable between both materials (**Table 1)**. Furthermore, PPA research showcased a modified synthesis method in which PPA was synthesized in the presence of CB, which upon further analysis provided evidence of creating stronger intermolecular π-π interactions between the two materials, improving the cycling stability of the PPA/CB composite electrode.

Table 1: Summary of the experimentally determined critical performance metrics for PPA and PDI-DAQ

	PPA	PDI-DAQ
Optimal Electrode Composition (PPA:CB)	80:20	50:50
Capacitance (F g^{-1})	377	319
Capacitance Retention (10,000 Cycles; 50:50)	61%	61%
Rate Capability	64%	61%
Charge Transfer Resistance (Ω)	5.2	21.6
BET Surface Area (m^2 g)	136	154

An important aspect of these research results is highlighting the areas for improvement for both PPA and PDI-DAQ. The cycling stability and rate capability of both materials especially are not comparative to leading supercapacitor material research which necessitates continued research endeavours to identify the underlying mechanisms governing the limitations of PPA and PDI-DAQ to devise strategies for improvement.

Further investigation of the mechanism of capacitance degradation of both PPA and PDI-DAQ by spectroscopic analysis of the respective composite electrodes during, and after continuous cycling is required to identify morphological changes occurring, such as evidence of swelling/shrinking, pore size changes, or structural degradation. The redox groups of PPA were found to degrade at individual rates, which can be a starting point to find out the individual mechanisms of redox-activity loss for the perylene and anthraquinone moieties. Using spectroscopic techniques such as FTIR to identify if individual functional group degradation occurs during cycling would lead to

determination of the chemical changes the functional groups undergo, if any. This methodology can be employed for either PPA or PDI-DAQ. To ensure dissolution of the organic molecules is not occurring and contributing to capacitance loss over cycling, highly sensitive quantification methods such as ultraviolet-visible spectroscopy can be performed on the electrolyte following prolonged cycling to search for evidence of PPA or PDI-DAQ that has detached itself from the electrode.

As the modified PPA synthesis in the presence of CB provided evidence of improved cycling stability as a result of stronger π-π interactions, further improvement the degree of intermolecular non-covalent or covalent interactions between PPA or PDI-DAQ and carbon substrates through synthesis modification can be performed. One such modification is preparing CB prior to synthesis with PPA or PDI-DAQ by dispersing CB into smaller agglomerates to increase the surface area available for π-π interactions to form during synthesis. Another avenue to pursue is examining synthesis solvent options to determine if there are alternatives that allow for PPA or PDI-DAQ synthesis while also dispersing CB more effectively than imidazole does. Grafting either molecule to CB following synthesis is another method to test for improved cycling stability, as immobilizing organic molecules to carbon substrates has shown evidence of increasing durability during cycling. Comparing the performance of the covalently bonded molecules to carbon substrates, such as CB, to non-covalent π-π interactions with CB can provide insight into the advantages of different methods of immobilization of the molecules to carbon substrates has on the long-term cycling stability. Comparison can include the differences in capacitance and stability improvement observed, and the trade-offs involved regarding the degree complexity between the material synthesis methods. The suggested future work involved can directly improve the electrochemical energy storage capabilities of PPA and PDI-DAQ as supercapacitor electrode materials, as well as

provide valuable direction to further understand the underlying mechanisms of the redox activity and degradation of the materials. Furthermore, more research on these materials can answer whether organic supercapacitor research should focus on smaller molecules such as PDI-DAQ, or polymers such as PPA.

On a grander scale, the contributions to the sustainable energy storage research field that have been outlined is important for finding alternative technologies to implement into the transportation sector to decrease CO_2 emissions. This research addresses the motivation behind supercapacitor research to contribute to improving EV technologies and acts as a beacon to future sustainability-focused researchers to pursue organic supercapacitor research for the opportunities presented to ensure a sustainable energy future.

6. References

[1] R. Lindsey and L. Dahlman, "Climate Change: Global Temperature," *Climate..gov*, 2024. [Online]. Available: https://www.climate.gov/news-features/understanding-climate/climate-change-global-temperature.

[2] K. O. Yoro and M. O. Daramola, *CO2 emission sources, greenhouse gases, and the global warming effect*. Elsevier Inc., 2020.

[3] C. Le Quéré *et al.*, "Temporary reduction in daily global CO2 emissions during the COVID-19 forced confinement," *Nat. Clim. Chang.*, vol. 10, no. 7, pp. 647–653, 2020.

[4] "CO2 Emissions in 2022," *International Energy Agency*, 2022. [Online]. Available: https://www.iea.org/reports/co2-emissions-in-2022.

[5] D. Lemian and F. Bode, "Battery-Supercapacitor Energy Storage Systems for Electrical Vehicles: A Review," *Energies*, vol. 15, no. 15, 2022.

[6] V. Singh, V. Singh, and S. Vaibhav, “A review and simple meta-analysis of factors influencing adoption of electric vehicles,” *Transp. Res. Part D Transp. Environ.*, vol. 86, no. August, p. 102436, 2020.

[7] “Zero emissions vehicle infrastructure program,” *Natural Resources Canada*, 2022. [Online]. Available: https://natural-resources.canada.ca/energy-efficiency/transportation-alternative-fuels/zero-emission-vehicle-infrastructure-program/21876.

[8] “Emissions from electric vehicles,” *U.S Department of Energy*, 2021. [Online]. Available: https://www.google.ca/url?sa=t&source=web&rct=j&opi=89978449&url=https://afdc.energy.gov/vehicles/electric_emissions.html&ved=2ahUKEwiMuLm4w6aFAxWUMjQIHU28APIQFnoECA4QAQ&usg=AOvVaw0N9neVabd7m4fjJumOJnSA.

[9] H. Xu and M. Shen, “The control of lithium-ion batteries and supercapacitors in hybrid energy storage systems for electric vehicles: A review,” *Int. J. Energy Res.*, vol. 45, no. 15, pp. 20524–20544, 2021.

[10] M. J. Lain and E. Kendrick, “Understanding the limitations of lithium ion batteries at high rates,” *J. Power Sources*, vol. 493, p. 229690, 2021.

[11] S. Rajagopal, R. Pulapparambil Vallikkattil, M. Mohamed Ibrahim, and D. G. Velev, “Electrode Materials for Supercapacitors in Hybrid Electric Vehicles: Challenges and Current Progress,” *Condens. Matter*, vol. 7, no. 1, 2022.

[12] F. Naseri, E. Farjah, and T. Ghanbari, “An Efficient Regenerative Braking System Based on Battery/Supercapacitor for Electric, Hybrid, and Plug-In Hybrid Electric Vehicles With BLDC Motor,” *IEEE Trans. Veh. Technol.*, vol. 66, no. 5, pp. 3724–3738, 2017.

[13] C. Choi *et al.*, “Achieving high energy density and high power density with pseudocapacitive materials,” *Nat. Rev. Mater.*, vol. 5, no. 1, pp. 5–19, 2020.

[14] S. Najib and E. Erdem, “Current progress achieved in novel materials for supercapacitor electrodes: Mini review,” *Nanoscale Adv.*, vol. 1, no. 8, pp. 2817–2827, 2019.

[15] S. Khodabakhshi, P. F. Fulvio, and E. Andreoli, “Carbon black reborn: Structure and chemistry for renewable energy harnessing,” *Carbon N. Y.*, vol. 162, pp. 604–649, 2020.

[16] Y. Yoo, J. Park, M. S. Kim, and W. Kim, “Development of 2.8 V Ketjen black supercapacitors with high rate capabilities for AC line filtering,” *J. Power Sources*, vol. 360, pp. 383–390, 2017.

[17] E. Dhandapani, S. Thangarasu, S. Ramesh, K. Ramesh, R. Vasudevan, and N. Duraisamy, “Recent development and prospective of carbonaceous material, conducting polymer and their composite electrode materials for supercapacitor — A review,” *J. Energy Storage*, vol. 52, no. PC, p. 104937, 2022.

[18] A. Eftekhari, L. Li, and Y. Yang, “Polyaniline supercapacitors,” *J. Power Sources*, vol. 347, pp. 86–107, 2017.

[19] S. A. A. Shah, R. Idrees, and S. Saeed, “A critical review on polyimide derived carbon materials for high-performance supercapacitor electrodes,” *J. Energy Storage*, vol. 55, no. PC, p. 105667, 2022.

[20] Y. Zhao *et al.*, “A π-Conjugated Polyimide-Based High-Performance Aqueous Potassium-Ion Asymmetric Supercapacitor,” *Macromol. Rapid Commun.*, vol. 43, no. 15, pp. 1–8, 2022.

[21] L. Jiao *et al.*, “A novel organic molecule electrode based on organic polymer functionalized graphene for supercapacitor with high-performance,” *J. Energy Storage*, vol. 52, no. PA, p. 104777, 2022.

[22] M. -F Grenier-Loustalot, F. Joubert, and P. Grenier, “Mechanism and kinetics of the

polymerization of thermoplastic polyimides. I. Study of the pyromellitic anhydride/aromatic amine system," *J. Polym. Sci. Part A Polym. Chem.*, vol. 29, no. 11, pp. 1649–1660, 1991.

[23] F. Ma *et al.*, "Organic Molecular Electrode with Ultrahigh Rate Capability for Supercapacitors," *Energy and Fuels*, vol. 34, no. 10, pp. 13079–13088, 2020.

[24] B. Jiang *et al.*, "Solution-processed perylene diimide-ethylene diamine cathodes for aqueous zinc ion batteries," *J. Colloid Interface Sci.*, vol. 598, pp. 36–44, 2021.

[25] M. R. Biradar, A. M. Kale, B. C. Kim, S. V. Bhosale, and S. V. Bhosale, "Perylenediimide/Graphite Foil-Based Electrode Materials with Outstanding Cycling Stability for Symmetric Supercapacitor Device Architectures," *Energy Technol.*, vol. 10, no. 6, pp. 1–10, 2022.

[26] X. Wang *et al.*, "Insoluble small-molecule organic cathodes for highly efficient pure-organic Li-ion batteries," *Green Chem.*, vol. 23, no. 16, pp. 6090–6100, 2021.

[27] Y. Hu *et al.*, "Ultra-Stable, Ultra-Long-Lifespan and Ultra-High-Rate Na-ion Batteries Using Small-Molecule Organic Cathodes," *Energy Storage Mater.*, vol. 41, no. July, pp. 738–747, 2021.

[28] Y. Hu *et al.*, "Novel Insoluble Organic Cathodes for Advanced Organic K-Ion Batteries," *Adv. Funct. Mater.*, vol. 30, no. 17, pp. 1–10, 2020.

[29] Y. He, Q. Wei, N. An, C. Meng, and Z. Hu, "Organic Small-Molecule Electrodes: Emerging Organic Composite Materials in Supercapacitors for Efficient Energy Storage," *Molecules*, vol. 27, no. 22, 2022.

[30] Y. Shao *et al.*, "Design and Mechanisms of Asymmetric Supercapacitors," *Chem. Rev.*, vol. 118, no. 18, pp. 9233–9280, 2018.

[31] N. Elgrishi, K. J. Rountree, B. D. McCarthy, E. S. Rountree, T. T. Eisenhart, and J. L. Dempsey, "A Practical Beginner's Guide to Cyclic Voltammetry," *J. Chem. Educ.*, vol. 95, no. 2, pp. 197–206, 2018.

[32] "Double Junction Solver Chloride Reference Electrode," *Pine Research*. [Online]. Available: https://pineresearch.com/shop/products/electrodes/reference-electrodes/standard/double-junction-silver-chloride/#description.

[33] L. Zeng, T. Wu, T. Ye, T. Mo, R. Qiao, and G. Feng, "Modeling galvanostatic charge–discharge of nanoporous supercapacitors," *Nat. Comput. Sci.*, vol. 1, no. 11, pp. 725–731, 2021.

[34] X. Yang and A. L. Rogach, "Electrochemical Techniques in Battery Research: A Tutorial for Nonelectrochemists," *Adv. Energy Mater.*, vol. 9, no. 25, pp. 1–10, 2019.

[35] A. C. Lazana and M. I. Prodromidis, "Electrochemical Impedance Spectroscopy-A Tutorial," *ACS Meas. Sci.*, vol. 3, no. 3, pp. 162–193, 2023.

[36] Gamry Instruments, "Testing Super-Capacitors," *White Pap.*, p. 58, 2018.

[37] "Basics of Electrochemical Impedance Spectroscopy," *Gamry Instruments*. [Online]. Available: https://www.gamry.com/application-notes/EIS/basics-of-electrochemical-impedance-spectroscopy/.

[38] T. Zavalis, "Studying Impedance to Analyze the Li-Ion Battery with an App," *Comsol*, 2015. [Online]. Available: https://www.comsol.com/blogs/studying-impedance-to-analyze-the-li-ion-battery-with-an-app/. [Accessed: 02-Apr-2024].

[39] J. I. Goldstein, D. E. Newbury, J. R. Michasel, N. W. . Ritchie, J. H. J. Scott, and D. C. Joy, *Scanning Electron Microscopy and X-Ray Microanalysis*. 2018.

[40] D. Harvey, "21.3: Scanning Electron Microscopy," *LibreTexts Chemistry*. [Online].

Available: https://chem.libretexts.org/Bookshelves/Analytical_Chemistry/Instrumental_Analysis_%28LibreTexts%29/21%3A_Surface_Characterization_by_Spectroscopy_and_Microscopy/21.03%3A_Scanning_Electron_Microscopy. [Accessed: 02-Apr-2024].

[41] "Which Electron Detector is Right for Your Application?," *Nanoscience Instruments*, 2024. .

[42] H. Toraya, "Introduction to X-ray analysis using the diffraction method," *Rigaku J.*, vol. 32, no. 2, pp. 35–43, 2016.

[43] T. Sochi, "High Throughput Software for Powder Diffraction and its Application to Heterogeneous Catalysis," 2010.

[44] F. A. Stevie and C. L. Donley, "Introduction to x-ray photoelectron spectroscopy," *J. Vac. Sci. Technol. A Vacuum, Surfaces, Film.*, vol. 38, no. 6, 2020.

[45] J. B. Lambert, E. P. Mazzola, and C. D. Ridge, *Nuclear Magnetic Resonance Spectroscopy: An Introduction to Principles, Applications, and Experimental Methods*, 2nd ed. John Wiley & Sons, Ltd, 2019.

[46] "How NMR Works; NMR 101," *Bruker*. [Online]. Available: https://www.bruker.com/en/resources/library/application-notes-mr/nmr-101.html#:~:text=An information-rich and non,in solid or liquid samples. [Accessed: 25-Feb-2024].

[47] A. A. Ismail, F. R. van de Voort, and J. Sedman, "Chapter 4 Fourier transform infrared spectroscopy: Principles and applications," *Tech. Instrum. Anal. Chem.*, vol. 18, pp. 93–139, 1997.

[48] N. Saadatkhah *et al.*, "Experimental methods in chemical engineering: Thermogravimetric

analysis—TGA," *Can. J. Chem. Eng.*, vol. 98, no. 1, pp. 34–43, 2020.